Contact Line Dynamics on Heterogeneous Substrates

Dissertation
zur Erlangung des mathematisch-naturwissenschaftlichen Doktorgrades
"Doctor rerum naturalium"
der Georg-August-Universität Göttingen
–
im Promotionsprogramm ProPhys
der Georg-August University School of Science (GAUSS)

vorgelegt von
Daniel Herde
aus Luxembourg, Luxemburg

Göttingen, 2013

Betreuungsausschuss:

Prof. Stephan Herminghaus, Max-Planck-Institut für Dynamik und Selbst-Organisation
Prof. Marcus Müller, Georg-August Universität Göttingen
Dr. Martin Brinkmann, Universität des Saarlandes

Mitglieder der Prüfungskommission:

Referent: Prof. Marcus Müller, Georg-August Universität Göttingen
Korreferent: Prof. Stephan Herminghaus, MPI DS

Weitere Mitglieder der Prüfungskommission:

Prof. Uwe Thiele, Loughborough University
Prof. Reiner Kree, Georg-August Universität Göttingen
Dr. Jean-Christophe Baret, MPI DS
Dr. Martin Brinkmann, Universität des Saarlandes

Tag der mündlichen Prüfung:

Abstract

Fluid interfaces in contact with solid substrates play an important role in fields ranging from microfluidics, over oil recovery and inkjet printing to coating processes. Effective models for the static wetting of structured substrates exist, as models for the dynamics of a fluid interface moving over a molecularly uniform and flat substrate.

In the present work, the effect of a periodically varying wetting energy on the dynamics of contact lines is studied. To study the static configurations, a minimisation approach for the free energy and continuation methods are employed. The dynamics of the free interface flow are modeled in the Stokes limit using boundary element methods. This is complemented by simulations of a simplified system in the form of the thin film model.

First, the effect of surface heterogeneities on a contact line driven with a constant velocity is addressed. A connection between the motion of the contact line over the substrate and the macroscopic contact angle is observed. To get a better understanding of the response of the fluid interface to the variation of the contact angle, a time periodic variation of the contact angle is introduced. This allows to characterise the displacement of the contact line depending on the driving frequency and slip in the system.

Based on the observed response of the fluid interface, a mode expansion model is proposed to give a simplified description for the motion of the contact line. The basic assumption is that there is no distinction between the response of the interface to a non-sinusoidal variation of the contact angle with time and the response to the contact angle determined by the current position of the contact line.

This is followed by a study on the motion of a droplet driven over a heterogeneous substrate with a constant body force. There, the effect of the amplitude and characteristic length scale of the heterogeneity on the possible droplet configurations is studied. It continues with a study of the depinning process and dynamics of the depinned droplets. In the limit of high slip lengths, a coexistence of pinned and depinned droplets was observed.

To understand the mechanism underlying this transition, a simplified model based on the translation and deformation mode of the droplet is considered. The model shows how the varying mobility ratio of these two modes allows for a change in the observed bifurcation scenario.

Contents

1 Introduction

The problem of fluid droplets resting and moving on a solid substrate is encountered in a range of fields from rain droplets sitting on a leaf to oil recovery[88], where water is used to displace oil in a porous medium. Wetting of non-uniform surfaces plays an important role in many biological systems. The Namib desert beetle for example uses a water-repelling (hydrophobic) structure on its wings to harvest condensing water for consumption[96]. Plants, as the Lotus or Indian Cress, use hydrophobic structures to make droplets slide off easily[50]. The self-cleaning functionality of such surfaces, where the sliding droplets remove any residual particles on it, is often referred to as Lotus effect.

These hydrophobic structures, as inspired by nature, and more advanced amphiphobic structures, that repel both oil and water, also have a number of industrial applications: Possible use cases range from surface coatings for simplified removal of graffiti[83] to reducing hydrodynamic drag, for example for swimsuits[74]. This drag reduction is achieved by trapping air at the surface of the material, thus reducing the friction at the interface.

In industrial applications, control of the wetting properties is important: For the printing industry, stronger localization of the droplets is of interest to achieve higher resolutions[21]. On the other hand, insecticide dispersal requires the plants to be covered as uniform as possible by the liquid[93], as in the case of surface coating technologies[94]. The pinning and mobilization of fluid interfaces is important in the oil industry as the goal is to make oil accessible for secondary recovery by displacing it with water[88]. One surprising application where contact line dynamics plays an important role is lithography on silicone wafers, where immersion lithography is used to obtain smaller structure sizes[49]. There, a droplet is deposited on the silicon wafer below the lithography optics to modify the index of refraction. As different parts are exposed, the droplet must be moved without film formation or deposition of droplets, making contact line dynamics a speed-limiting step in this process. In all of these cases, a fluid-liquid or a liquid-liquid interface is moving over a solid substrate.

Since wetting phenomena play a fundamental role in many biological systems and applications, research on the theoretic foundations of wetting dates back to the 18th century[95]. Young explained how the interfacial energies of the interfaces determine the equilibrium contact angle, i.e. the slope with which the fluid-liquid interface approaches the substrate. When a fluid does not cover the solid completely, but forms a drop with an interface that approaches the substrate with a finite angle, it is referred to as partially wetting. This angle is unique for homogeneous substrates, but not for substrates with a topographically structured surface or chemical impurities on the surface. In these cases, the microscopic contact angle varies with the position on the substrate.

The interfacial energy argument is a continuum approach for describing static wetting. It does not necessarily hold on length scales where thermal and molecular fluctuations play a role, i.e. close to the contact line. Fundamental questions concerning this transition from a molecular microscopic description to the continuum description are still unsolved[13]. The best continuum description to date accounts for the molecular interaction of the fluids with the substrate with an extra pressure term that depends on the distance from the surface. While

it gives a very good agreement in the limit of small contact angles, this approach leads to problems when attempting to model hydrophobic substrates.

Going beyond the static wetting of homogeneous substrates, there are two main directions in wetting research: One side is focussed on preparing flat and chemically pure substrates to study the motion of a fluid interface moving over it. The other side studies the possible configurations that a static, non-moving fluid can take on a structured surface.

When studying static wetting of heterogeneous substrates, the goal is to determine the shape that a fluid interface can take on a substrate, which has a position dependent contact angle, a topographic structure of the surface or a combination of both. Two fundamental publications in this field are the work of Cassie[17] and Wenzel[92], making predictions on the apparent contact angle that is observed for a fluid wetting a non-uniform substrate. These predicted only an average contact angle, though, based on a term for the effective surface free energy that takes the topography into account. On most heterogeneous substrates, multiple stable and and metastable configurations of the fluid interface, and therefore a range of contact angles can be observed for which the contact line does not move. This range is characterized by the static advancing and static receding contact angle. This problem of static droplet configurations on heterogeneous substrates has received significant attention from the theoretical side[17, 16, 37, 40, 80, 34]. Over time, more advanced methods to predict these angles on patterned surfaces were developed, for example by direct numerical minimization of an energy functional to obtain static interface shapes[69].

There were attempts to generalize this approach to moving fluid interfaces, as presented by Santos *et al.*[63]. Their work studied the droplet motion on a heterogeneous substrate in the quasi-static limit. The assumption is that the droplet shape is close to the equilibrium, but the motion is determined by a friction law that relates the macroscopic contact angle obtained by minimizing the free energy of the interface to a contact line velocity. This approach does not take into account the fluid flow and resulting viscous stresses acting on the fluid interface.

For the dynamic case, where the contact line is moving over the substrate, giving universal descriptions of the underlying mechanisms is more challenging. These interfaces are driven by an external forcing or thermally activated processes taking place at the substrate. Disparate approaches to describe these processes can be found in the literature. The models based on a continuum description consider spatial averages of the molecule velocities. They hold on length scales above the molecular length scale. Major theoretical work in this direction was undertaken by Cox and Voinov[90] and recently by Eggers[24]. A microscopic approach to the question is to assume that the dynamics is determined by molecular hopping processes taking place at the contact line. One example for such a molecular model is the molecular kinetic theory (MKT) by Blake[11]. The MKT assumes that the motion at the contact line can be approximated by the thermally activated escape of a particle from a potential well. These fundamental works assume an atomically flat and homogeneous substrate. They do not attempt to describe the effect of topographic or chemical structures on the substrate that break the translation invariance of the problem.

A natural extension of the study of contact lines dynamics is the study of moving fluids droplets, where moving contact lines are coupled with a bulk fluid flow. The problem of a droplet moving on a homogeneous plane with a small inclination angle has been studied extensively. The work of Hodges *et al.*[36] provides a range of references on this topic. Results on the tail formed by droplets moving on an inclined substrate due to viscous stresses were obtained by Snoeijer *et al.*[73]. Their work described both numerically and experimentally how the opening angle of the corner at the back end decreases with increasing droplet velocity,

which eventually results in a pinch-off of smaller droplets.

Going beyond the dynamic wetting on homogeneous substrates and the static wetting on static substrates, the wetting dynamics on non-ideal substrates recently moved into the focus of research[65]. The goal of the present work is to provide a better understanding for the response of a fluid interface driven over a substrate with a periodically varying wetting energy and to present possible approaches to reduce the complexity.

To achieve this goal, the motion of a droplet over a substrate, where the microscopic contact angle varies periodically with the position on the substrate, is simulated in the continuum limit. Understanding the motion over a periodically patterned substrate is a first step towards a better understanding for the dynamic contact angles observed experimentally on real, i.e. non-ideal, surfaces. This system is studied in the limit of continuum mechanics in a translationally invariant, i.e. effectively two-dimensional, system. For a heterogeneity of the form of a sinusoidal variation of the wetting energy, the length scale and amplitude of the wetting energy contrast can be varied systematically. The response was studied in two different configurations: In the first part, the response of the interfaces of a droplet driven with constant velocity was considered. In the second part, the depinning and subsequent motion of a droplet driven with constant force is presented.

The dynamics of the free interface flow was studied in the Stokes limit. The solutions to the Stokes equation that determine the time evolution of the free interface were computed using Boundary Element Methods(BEM), as described by Pozrikidis[55]. This approach makes it possible to study systems with high contact angles, going beyond the lubrication approximation for fluid interfaces with small and slowly varying slopes. An application of BEM to model moving droplets in the Stokes limit are the works of Schleizer[67] and Spelt[76, 22]. These works studied the motion of droplets on substrates in a shear flow geometry. While the first study did not incorporate substrate heterogeneities, they were incorporated in the second study on a microscopic scale, by using a static advancing and receding contact angle. As the contact angles do not vary spatially, the droplet still approaches a stationary shape. The present work goes beyond this limit by introducing a microscopic contact angle that varies with the position of the contact line on the substrate.

These publications discuss difficulties associated with the implementation of contact line dynamics in the boundary element formalism. When the work of Schleizer[67] was published, implementing the Navier slip condition at the substrate required a prohibitive computational effort, therefore an effective slip model was introduced. The present work goes beyond the approximation of spatially homogeneous advancing and receding contact angles by studying a spatially varying wetting energy. The goal is to understand if and in which limit such a heterogeneous substrate can be reasonably well approximated with a spatially uniform heterogeneity.

The second part of the thesis was motivated by work on the depinning of droplets from single defects done by Beltrame, Thiele and Knobloch[7, 85, 8]. It showed the effect of pinning strength on depinning energy and mobility for cases of two-dimensional and three-dimensional droplets. They modeled the problem in the lubrication approximation with a disjoining pressure, which allows for fluid to flow through the prewetting film, especially for low heterogeneities. Due to this non-vanishing flux, determining a depinning threshold for low heterogeneities / thick precursor films is difficult. In the present work, this problem is extended to the case of arbitrary substrate contact angles and multiple defects, in an attempt to approach the case of a general heterogeneous substrate. The results can be found in chapter 5.

Recently, significant progress on the wetting dynamics on structured and randomly heterogeneous substrates using an asymptotic matching approach was achieved by Savva and Kalliadasis[64, 65, 66]. While still operating in the thin film limit, their novel matching approach allowed them to study the spreading of two-dimensional droplets on randomly structured topographic and chemical heterogeneities. Their approach reduced the dynamics of a spreading droplet to a set of ODEs for the dynamics of the contact line.

The dynamics of free interface can also be modeled without solving the fluid dynamic equations explicitly on a mesh by using particle based methods. Molecular Dynamics (MD) simulations and Lattice-Boltzmann models are used for fluid dynamics problems. Other methods are also available, like dissipative particle dynamics and stochastic rotation dynamics, bridging the gap and offering different levels of abstraction and coarse-graining. MD simulations represent individual molecules as particles with atomistically justified two-particle interaction forces. These models were successfully employed to study wetting dynamics[9], also when being coupled with continuum models by parameter passing[87].

Lattice-Boltzmann simulations operate on particles in a discretised space and velocity domain, with the atomistic interactions represented by a collision operator acting on the density distribution of the particle velocities at the same grid point. A range of wetting-related phenomena, including contact angle hysteresis on chemically patterned substrates[40, 53, 62] were modeled with this approach. This is the oldest and most well-established tool of the particle based methods mentioned here. Another two recent methods are relevant to simulating fluid flows on a coarse-grained scale. In both models one particle does not represent a single atom or molecule, but rather a volume of fluid: Stochastic rotation dynamics[61], similar to Lattice-Boltzmann simulations, uses a rotation operator in a collision box to replace the two-particle interactions, but with continuous particle velocities and positions. Dissipative particle dynamics[31] uses pairwise interactions between particles within a certain cutoff region. These models cannot obtain an increased resolution in regions of interest without coupling models for the different length scales. Therefore studying contact line phenomena in a system spanning multiple length scales becomes computationally expensive using these particle based methods and a continuum approach was employed in the present work.

The thesis has the following structure: In chapter 2, the foundations of free interface flows and both statics and dynamics of contact line dynamics are introduced. After an introduction to the fundamental equations governing fluid flows, the boundary conditions due to solid and free interfaces are discussed. This is followed by a presentation of the different models for static and moving contact lines.

In chapter 3, the numerical methods used to study contact line problems in the present work are introduced. Two different approaches to obtain static fluid interface configurations are presented: One based on a free energy minimization, the other based on determining solutions to the differential equation that determines interface shapes directly. This is followed by an introduction to the boundary element methods code employed in the present work to study the dynamics of free interface flows. The method used to solve the thin film equation with sharp contact lines is also discussed.

Chapter 4 presents the results obtained for a contact line driven with a constant velocity over a substrate with a periodic variation of the contact angle. The goal is to get a better understanding for the effect of the spatially varying substrate contact angle on the motion of the interface and the macroscopic contact angle that can be observed. By combining these observations with the results obtained from varying the contact angle with time, a simplified model for predicting the contact line motion could be introduced.

The second part of the results, chapter 5 presents the observations on droplets driven with a volume force over a substrate with periodically varying contact angle. As the two-dimensional system is studied, it can be thought of as two contact lines coupled through the fluid bulk. Influence of the length scale of the heterogeneity on the droplet dynamics are studied. This is followed by discussion of a simplified model for the droplet dynamics in the form of a modified gradient dynamics on a static energy landscape.

It ends with the conclusions and an outlook on possible future research directions that build up on the present work. A list of figures, a list of symbols and an index can be found at the end of the thesis.

2 Foundation

This review chapter presents the foundations of fluid dynamics of immiscible fluids, confined both by solid and free interfaces. Based on the fundamental equations used to model fluid flows, the chapter presents the processes taking place at a moving contact lines. The contact line is the point where two fluid and the solid phase meet.

First, the continuum transport equations for momentum and mass are introduced to describe the time evolution of velocity, pressure, and density of an incompressible fluid. As the fluid is confined both by solid interfaces and free surfaces that can deform, the corresponding boundary conditions are presented. Second, an overview of different approaches to incorporate the contact line as transition point between different types of interfaces is given. Finally, a short overview over the relevant literature is given to clarify the scope and context of the present work.

2.1 Governing equations of continuum fluid dynamics

From astronomic length scales down to length scales in the range of nanometers, fluid dynamics describes the motion of molecules interacting through repulsive and attractive forces. All the trajectories of the individual particles follow the fundamental equations of conservation of energy and momentum. When studying the system on length scales where the individual fluctuation can not be observed, macroscopic variables that represent these averaged value of these quantities can now be introduced as continuous fields in space. In the continuum limit, the conservation of of mass and linear momentum still has to hold. These conservation laws can now be expressed in the form of continuity equations that relate changes of an averaged density to the divergence of a flux.

Phenomena like phase separation are also based on microscopic interactions on the molecular length scale. The difference in the interaction force between molecules of different fluids leads to aggregation and separation of the different phases, as in the case of immiscible liquids. Immiscible liquids still have a transition region between the different phases with a width in the range of nanometers. If the smallest length scale that is resolved in the model is larger than the width of the transition region, it can be replaced by a “sharp” interface at which the system properties change discontinously. This discontinously changing property can be for example the density, the velocity tangential to the interface or the stress normal to the interface.

2.1.1 Navier Stokes equation

The conservation laws of mass and linear momentum can be expressed in form of a continuity equation that relates the change of mass density to the divergence of a mass current, and another equation that relates the volume force density to the divergence of a local stress and a momentum flux coupled to mass transport. The conservation of linear momentum takes the form:

$$\frac{\partial}{\partial t}(\rho u) + \nabla(\rho u \otimes u) - \nabla\sigma - g(x) = 0$$

with u being the velocity field, ρ the local density, σ representing the local stress in the fluid and $g(x)$ a volume force that might depend on the position x in the system and is introduced by an external field acting on the system. The symbol $\otimes$ represents the outer product of two vectors. When integrating over a volume element, the first part represents the change in momentum in the volume element, the gradient terms represent the flow of momentum due to convection, viscous stresses and pressure gradients in the fluid through the domain boundaries and the last term describes the coupling of the momentum to the external force field $g(x)$. One example for such an external field would be gravity.

The second continuity equation, the conservation of mass, can be written similarly as

$$\frac{\partial}{\partial t}\rho + \nabla(\rho u) = 0$$

assuming that no mass sources or sinks exist in the system. Integrated over a volume element, it states that the change in mass in the volume has to correspond to the flux into or out of the volume.

In order to obtain a closed system of partial differential equations the continuity equations of mass and linear momentum have to be complemented by a constitutive relation between stresses and strain rate and an equation of state of the fluid. Based on Newton's observation that the viscous stress σ in ideal viscous fluids is proportional to the rate of strain tensor, together with the assumption of an isotropic liquid and the fact that $\nabla\sigma$ should vanish when the fluid is at rest, the stress tensor can be assumed to have the form

$$\sigma = \eta\dot{\varepsilon} - \mathbb{I}p$$

with η representing the dynamic viscosity of the fluid, p the isotropic fluid pressure and the rate of strain tensor defined as

$$\dot{\varepsilon} = (\nabla \otimes u) + (\nabla \otimes u)^T$$

The unit tensor is represented by $\mathbb{I}$. The second common assumption is the incompressibility of fluids, i.e. that the density ρ is a local property of the fluid that gets advected with the fluid flow. For an incompressible fluid, the divergence of the velocity field vanishes. With those two assumptions, i.e. for an incompressible Newtonian fluid, the Navier-Stokes equation takes the following form[41]:

$$\rho\left(\frac{\partial u}{\partial t} + (u\nabla)u\right) = -\nabla p + \eta\nabla^2 u + g(x)$$

$$\nabla u = 0$$

Details of the derivation as outlined above can be found in in the textbook by Batchelor[5]. While this equation already has been simplified, it remains very difficult to solve due to the PDE being nonlinear with respect to the velocity field.

2.1.2 Steady Stokes equation

The nonlinear terms in the equations of motion prevent the application of standard methods to solve linear partial differential equations, for example methods based on the superposition of solutions. The nonlinearities arise from terms related to inertial effects. The variables can be rescaled with the characteristic length scale L determined by the domain boundaries, the characteristic velocity U occurring in the system and the resulting timescale $T = L/U$. With this, the Navier-Stokes equation can be written in the form[55]

$$Re(\frac{\partial u}{\partial t} + u\nabla u) = -\frac{\nabla p}{\eta} + \nabla^2 u + \frac{g(x)}{\eta}$$

$$\nabla u = 0$$

where $Re = UL\rho/\eta$ is named Reynolds number and gives the ratio between the inertial and the viscous force scale in the system. The nonlinearities are suppressed in the case where the Reynolds number is small, i.e. where inertia plays a minor role. In this limit, the terms on the left hand side can be neglected, leading to the Steady Stokes equation

$$0 = -\nabla p + \eta\nabla^2 u + g(x)$$

$$\nabla u = 0$$

The system of equations is linear in u and g. Therefore, a linear superposition of two solutions is still a solution of the differential equations. As a consequence the Greens formalism, as discussed by Pozrikidis[55], can be employed to express it as a boundary value problem. By representing a particular solution as superposition of fundamental solutions, it can be expressed in terms of stresses and velocities on the domain boundary. This approach will be discussed in the methods section, where the boundary element method (BEM) is introduced.

That means the state of the system is completely described by the current shape of the domain boundary and the velocity and stress on the boundary. For simple fluids in a free interface flow, the boundary values can be computed from the boundary conditions and the current shape of the domain boundary, as discussed later on. Therefore, the time evolution of a moving droplet is completely described by the shape of the domain boundary over time. The time evolution is determined by the deformation of the free interface in the induced flow field.

2.2 Boundary conditions for walls and free interfaces

With this understanding of the dynamics of the flow occurring in the bulk of a fluid, it is important to understand how the fluid interfaces can be represented in the continuum limit. The fluid interfaces can represent a transition region between two different liquids or a liquid and a solid and therefore have to be treated differently.

When studying a two-phase fluid on a microscopic length scale by using molecular dynamics simulations, a depletion layer or a mixing layer of molecular length scale can be observed in the transition region, depending on the system properties. On a length scale where the continuum description becomes appropriate, the width of this layer becomes negligible. The transition region can be approximated by a subspace on which system parameters, such as the density, viscosity and stress, exhibit a discontinuous variation. This is the sharp interface

approximation. In this approach, fluid-liquid and fluid-solid interfaces are characterized by different boundary conditions due to the microscopic interactions, as discussed below.

There are other approaches to introduce fluid interfaces in continuum models: One possibility is to introduce an additional field[3, 14] with an evolution equation that locally determines the phase. This field is coupled to the fluid dynamic equations by introducing phase-dependent viscosity and stress terms. Introducing an extra differential equation that describes the time evolution of the phase field increases the computational difficulty significantly. Increased computational complexity is detrimental to the goal of resolving the region of the three-phase contact line in detail. Therefore, the sharp interface approach is utilized in the present work.

2.2.1 Fluid-liquid interface

The sharp interface model assumes that the transition region between the fluid and the liquid is thin compared to the smallest length scale on which the system is observer. In this limit, the transition region can be replaced by a surface on which the macroscopic properties, as the density and viscosity, change discontinuously. It is observed that droplets and bubbles take a spherical shape, indicating that the system attempts to minimize the area of this interface between the fluid and the liquid.

The origin of of this excess energy can be understood when considering the liquid-vapor-coexistence of a fluid in a container. The free energy of the gas over the fluid density exhibits two local minima when phase separation occurs, corresponding to the liquid and the vapor phase. In the transition region of finite width between the two phases, the fluid density changes continuously. This gives rise to an excess free energy, as the free energy of fluid in this region is increased compared to the fluid in the bulk. The excess energy is proportional to the surface area of the liquid-vapor interface. In the sharp interface model, this transition region is replaced with a surface where the density changes discontinuously and the excess energy associated with the transition region is represented by the interfacial energy γ. A more comprehensive derivation of this phenomenon can be found in Ref. [5, 41].

The change in surface area by an infinitesimal normal displacement is determined by the mean curvature of the interface at that point, giving rise to a normal force acting on the interface proportional to the curvature. In an equilibrium state of a fluid-liquid interface, this stress has to be constant on the surface to prevent deformation of the interface. This stress due to surface forces is balanced by the pressure difference between the two phases. This is expressed by Laplace's formula

$$p_l - p_f = 2\gamma\kappa$$

with the mean curvature of the free interface κ, defined as

$$\kappa = \frac{1}{2}\left(\frac{1}{R_1} + \frac{1}{R_2}\right)$$

with $R_{1,2}$ as the two principal curvatures of the interface. The sign of the mean curvature κ is chosen such that it is positive for a spherical liquid droplet. For a static interface, only the surface forces have to balance. For a moving free interface, the surfaces forces and the viscous forces at the surface have to be in equilibrium[41]. This balance can be expressed in a more general form as a jump in the normal stress component proportional to the curvature of the interface, taking the form

$$n(\sigma_f - \sigma_l) = 2\, n\, \gamma\kappa \tag{2.1}$$

with n as the normal vector to the surface, $\sigma_{f,l}$ as the stress tensor in fluid and the liquid at the fluid interface, respectively, and γ as the interfacial tension. This characterizes the restoring force leading to free interfaces assuming configurations of constant mean curvature in a static mechanical equilibrium, unless additional external forces act upon the interface. The normal component of the velocity has to be continuous. Also, as no tangential forces act on the interface when the surface tension is constant, the tangential stress component has to be continuous at the fluid interface. This model aligns well with the classical treatment of fluid dynamical problems as solutions to PDEs with certain boundary conditions.

2.2.2 Fluid-solid interface

Stokes presented in 1845[77] that the relative velocity of a fluid has to continuously approach zero at a solid wall for slow fluid flows. He argued the stresses induced by any discontinuity in the velocity between the fluid and the solid would slow down the flow close at the wall until there is no relative motion of the fluid to the wall. This is called the no-slip boundary condition, stating that both the tangential velocity and the normal velocity have to be continuous at a fluid-solid interface. The idea behind this model is that the first layer of fluid particles adheres to the wall.

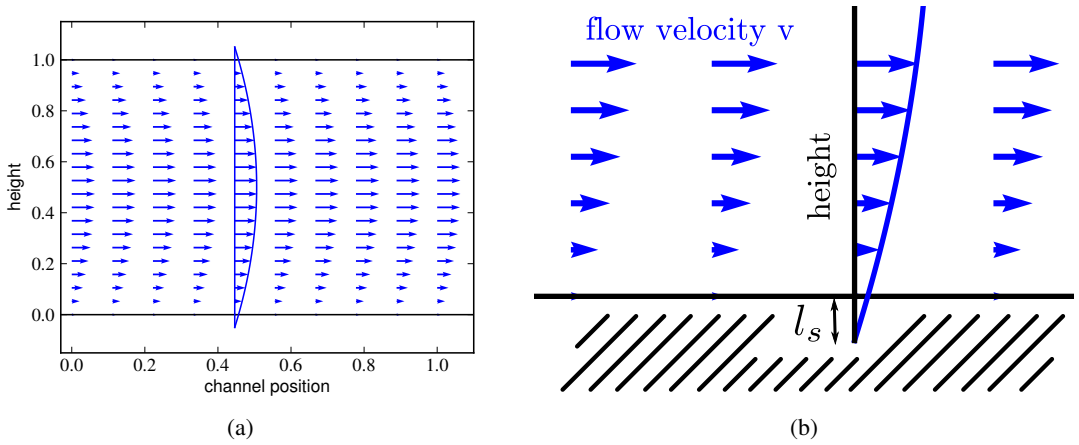

Fig. 2.1: a) Illustration of the velocity field (blue arrows) of a pressure driven channel flow with finite slip length. The blue parabola shows the extrapolated flow field reaching zero outside of the channel. b) Zoom of the region close to the channel wall, showing the parabolic flow profile and the extrapolation length determined by the slip length l_s more in detail.

This point of view has been challenged over the course of the last century, as observed flow fields showed a finite velocity close to the wall[42]. One example is the flow field observed in a pipe with circular cross-section that is driven by a constant pressure gradient. When fitting the measured radial velocity distribution with the closed-form solution for the flow field, a parabola, the observed profile reaches zero not at the wall, but at an extrapolated point outside of the fluid. That means the fluid still has a finite velocity at the wall, increasing with the driving velocity. To remedy this discrepancy between experimental observation and theoretical model, the Navier slip model was introduced. With u as the velocity relative to the

wall, it maintains the assumption that the wall is impermeable, i.e. that the fluid can not enter the wall

$$u_\perp = 0$$

but it states that the velocity tangential to the wall is proportional to the stress

$$u_\parallel = l_s \frac{\partial u_\parallel}{\partial n} = \frac{l_s}{\eta} f_\parallel$$

with $u_\perp$ and $u_\parallel$ as the normal and tangential components of the velocity at the wall and $f_\perp$ and $f_\parallel$ as the normal and tangential component of the projection of the stress tensor $f = \sigma n$ on the surface normal n. The length scale l_s is referred to as slip length, as it can be obtained from the depth in the substrate where the extrapolated observed velocity profile would reach zero. The slip length is commonly in the range of some nanometers, for example for water on a hydrophilic surface[12], but can be in the range of tens to hundreds of nanometers, as shown for polymer melts on specific surface coatings both experimentally[46] and numerically[70].

More than 150 years later, this problem is still subject of discussion. For example when comparing molecular dynamics simulations of polymer flows in a shear or a pipe flow it is necessary to enforce the Navier slip condition at a height above the fluid-solid interface to obtain consistent results[86].

2.3 Contact lines

The triple line where two fluids and a solid or a fluid, a liquid and a solid are in contact is referred to as contact line. At the contact line, interfaces with different boundary conditions, as introduced in the previous section, come into contact and have to be matched. In the static limit, the goal is to balance the interfacial energies in that point and study the set of energetically minimal configurations on non-ideal substrates. On the smallest scale, the challenge posed by contact lines is to obtain a description for the thermodynamics of interacting particles that can be incorporated into a continuum model capable of describing both a static and a moving interface. Even if the underlying processes close to the contact line are understood from the microscopic perspective, the observation length scale is in most cases orders of magnitude larger than the molecular length scale. This requires a model that accounts for the interface deformation due to viscous stresses on the intermediate length scales to enable predictions for the macroscopic dynamics that can be observed in the system.

The following reviews provide an extensive overview over contact line dynamics related questions, as this section only briefly covers the main results presented there that are directly related to the thesis: A review of the historic foundations of wetting dynamics on homogeneous substrates is given by “Wetting: statics and dynamics” by de Gennes from 1985[30]. A more recent overview, that also includes wetting of heterogeneous substrates, is given by the review paper written by Bonn *et al.*[13]. A second review on the problems of moving contact lines, also discussing the coupling of molecular to macroscopic scales, was written recently by Andreotti and Snoeijer[4].

In the beginning of this section, the theory of equilibrium contact angles on homogeneous substrates will be introduced, on which any discussion of moving contact lines must be based. This is followed by a section on a model for the molecular processes occurring close to the contact line, giving a description of the contact line motion as molecular hopping processes. One approach to regularize the stress singularity occuring at a moving contact line in the

continuum limit is to assume that the whole substrate is covered by a thin fluid film. This is introduced in the third subsection. For a moving fluid interface, the contribution of dynamic viscous stresses to the stress balance at the fluid interface has to be considered. Different approximations can be made for the flow field in the contact line region and the contribution of the resulting viscous stresses to stress balance that determines the steady shape of the fluid interface. These approximations are discussed in the last subsection of the chapter.

2.3.1 Equilibrium contact angles

In many cases the free interface of a liquid at rest approaches the substrate with a finite slope, as observed for a water droplet resting on a plastic plate. The angle formed between the fluid-liquid interface and the substrate is referred to as contact angle, as illustrated in Fig. 2.2. The wetting properties of the system, i.e. under which angle the fluid interface approaches the substrate or if it covers the substrate completely, depend both on the chemical properties of the substrate and the fluids, and the topographic structure of the substrate, which might enhance or limit the spreading of the fluid.

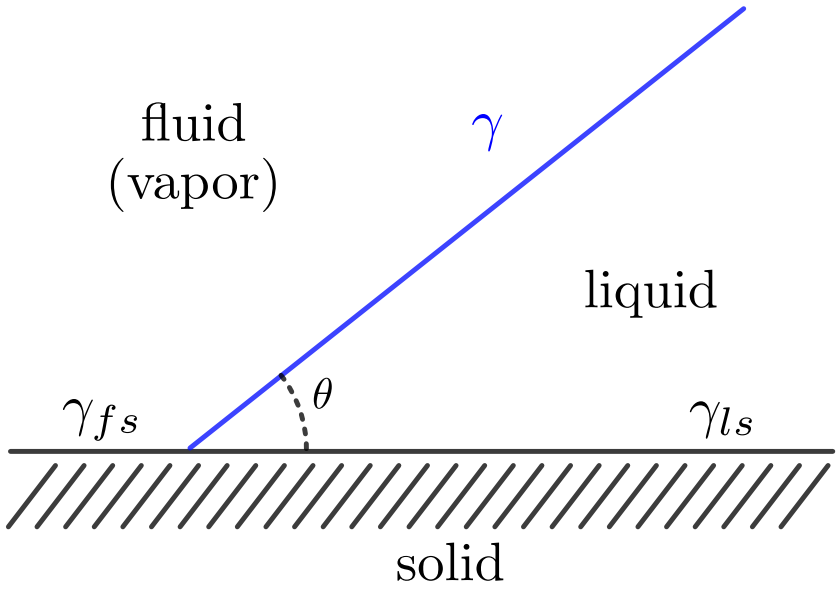

Fig. 2.2: Three-phase contact line with the interfacial free energies of the fluid-liquid interface γ, fluid-solid interface γ_{fs} and liquid-solid interface γ_{ls}, giving rise to the contact angle θ from the stress balance

For an ideal substrate, topographically flat and chemically homogeneous, the contact angle is controlled by the balance of the surface free energies, of the fluid-liquid γ, the fluid-substrate γ_{fs} and the liquid-substrate γ_{ls} interface. The surface free energy of the fluid-liquid interface is also commonly referred to as surface tension. If the energy difference $\gamma+\gamma_{ls}-\gamma_{fs}$ is smaller than zero, a flat substrate will be covered completely by the fluid. This is the fully wetting case. If $|\gamma_{fs}-\gamma_{ls}|<|\gamma|$, the system is partially wetting, i.e. the system shows a finite contact angle between the fluid-solid and fluid-gas interface, given by the relation:

$$\gamma_{ls}-\gamma_{fs}+\gamma\cos\theta=0$$

This relation was discussed already more than 200 years ago by Young[95]. If the contact angle deviates from the equilibrium angle, it implies that there is a residual stress at the contact line. This means that the contact line is still moving towards the equilibrium configuration. To describe the wetting properties of the substrate, a nondimensionalised wetting energy w can be introduced:

$$w = \frac{\gamma_{ls} - \gamma_{fs}}{\gamma}.$$

For $w \leq -1$, the fluid is completely wetting, while for $-1 < w < 1$, the fluid-interface approaches the substrate with a finite contact angle. This notation will be employed to describe the wetting properties of the substrate in the present work.

2.3.2 Microscopic approach: Molecular-kinetic theory

To describe the dynamics of a contact line in the limit where the motion is dominated by processes close to the contact line, Blake proposed a model known as molecular kinetic theory[11]. On a microscopic length scale, the contact line is not a discontinuity, but a region of space filled with particles moving due to the thermal energy in the system which display a gradient in the concentration of particles of the two fluids. In this model, the motion of the interface is controlled by thermal hopping of fluid molecules close to the substrate in a series of local energy minima. The idea is that the molecular structure of the substrate allows for a dynamic adsorption/desorption equilibrium of the migrating fluid molecules, leading to a motion of the contact line. The contribution of bulk fluid dynamics is neglected in this model, as the dynamic contact angle only influences the stress imbalance modifying the hopping rate.

The contact line velocity is therefore given by the flow in a forced thermally activated hopping process, following Kramer's problem of the escape rate of a thermally activated particle from a potential well[39, 32].

$$v = K_0 \lambda e^{\lambda^2 \gamma |\cos\theta_0 - \cos\theta| / (2 k_B T)}$$

Here, K_0 gives an hopping attempt frequency, λ a distance between two local minima. The term $\gamma|\cos\theta_0 - \cos\theta|$ gives the stress imbalance due to the apparent contact angle θ that deviates from the equilibrium contact angle θ_0.

This model has been fitted to datasets from various experimental setups [26, 45, 19]. The reported energy barriers and hopping distances in the range of several tens of nanometers or more do not agree well with the interpretation as hopping process on a molecular length scale[26], as the spacing of the local minima in the energy landscape of a homogeneous substrate is in the sub-nanometer range.

In Molecular Dynamics simulations, though, a quantitative agreement with this model has been achieved[20]. This is an indication that the deviation in real systems might be due to the inhomogeneous nature of the substrates in experimental setups. Most samples will feature both chemical and topographical heterogeneities on length scales ranging from nanometers to micrometers, depending on the preparation process. On the other hand, these structures correspond to energy barriers much higher than $k_B T$. It is unclear if the dynamics on such a length scale is best described by thermally activated motion.

2.3.3 Disjoining pressure and precursor films

Molecular forces between unpolar molecules feature both long distance attractive contributions, as van der Waals forces, and short distance repulsive forces, due to overlapping electron orbitals. The difference between the interaction of the two phases with the substrate can be incorporated in the continuum models as an additional pressure term on the free interface that depends on the distance from the substrate.

As mentioned previously, introducing a contact line in continuum models requires additional assumptions, as a slip condition at the substrate and a constitutive law for the dependence of the contact angle at the substrate on the velocity. Introducing such a pressure term that depends on the distance of the fluid interface to the substrate allows for the coexistence of macroscopic droplets and a thin film wetting the whole substrate. In the presence of such a precursor film there is no three-phase contact line, but only a transition region between the macroscopic droplet and the precursor film. The logarithmic stress singularity associated with contact line problems is now regularized with the cut-off length, determined by the thickness of the precursor. The no-slip condition at the substrate still holds for the wetting liquid in both regions.

To allow for a precursor film to form, the disjoining pressure is derived from a molecular interaction potential that has a local minimum at a distance h_0 over the substrate and decays to zero as $h \to \infty$. As presented for example in Ref. [84], the interface potential can take the form of

$$W(h) = -a(\frac{b}{h^3} - e^{-h/l_r}) \tag{2.2}$$

with l_r setting the length scale of the short-range attactive potential, $\sqrt[3]{b}$ the length scale of the long-range repulsive potential and a, with the dimension of an interfacial energy. The height-dependent disjoining pressure can now be introduced as the first derivative with the distance:

$$\Pi(h) = -\frac{\partial W(h)}{\partial h}$$

Figure 2.3 illustrates the shape of the potential for $b = 10^{-4}$ after non-dimensionalisation with a and l_r set to unity. The minimum of the potential allows for the formation of a precursor film, covering the whole substrate, from which the macroscopic droplet emerges. The effective slip that is observed for the macroscopic droplet increases with the thickness of the precursor film and thus is determined by the distance of the minimum of the potential from the substrate.

A fluid interface of unit length placed at $h_{\min}$, the thickness corresponding to the minimum of the potential, is energetically favorable by $\Delta W = W(\infty) - W(h_{\min})$, the depth of the minimum. Following Young's law, the contact angle can thus be determined by

$$\gamma \cos\theta = \gamma - \Delta W$$

with the energy contribution of the free interface balanced by the reduced contribution $\gamma - \Delta W$ of the free interface close to the substrate forming the precursor film[60]. This approach, especially the formation of a precursor film, leads to issues in the case of high contact angles. For thin films of a highly wetting fluid it is an elegant method to circumvent treatment of the three-phase contact line that intrinsically introduces a slip of the interface. Recently, Sibley *et al.*[71] argued that both contact line and precursor film models can be mapped onto each

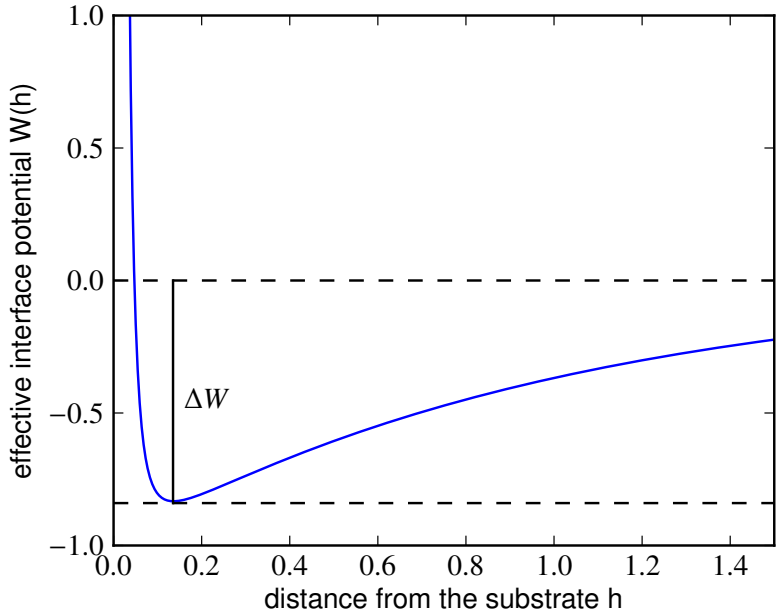

Fig. 2.3: Interface potential $W(h)$, as defined in eqn. 2.2, for $b = 10^{-4}$ after non-dimensionalisation with a and l_r. At h_0, the minimum interface potential ΔW is plotted.

other and therefore used interchangeably for small driving forces with appropriately chosen parameters. Their study was done for a moving contact line on a homogeneous substrate, though. In view of Ref. [85], where it was shown that the precursor film plays an important role in the depinning process, the present work will explore the depinning process of droplets with contact lines on substrates with Navier slip condition.

2.3.4 Dynamic contact angles in continuum models

For a static fluid interface, the interface assumes the shape of a surface with constant mean curvature, when gravitational contributions and other external force fields are negligible. For a moving interface, the viscous dissipation in the fluid increases close to the contact line. This leads to a deformation of the free interface, as the viscous stress has to be balanced by interfacial stress.

One model for the dynamic contact angle observed on a moving contact line was introduced by de Gennes[29]. He argued that the dissipation in a slice of the moving interface has to be balanced by the energy gain through the uncompensated Young force of the deformed interface. The work due to the uncompensated Young force F takes the form

$$P_{\text{inj}} = FU = U\gamma(\cos\theta - \cos\theta_0)$$

with U giving the contact line velocity, γ the surface tension of the fluid and θ_0 the equilibrium contact angle. The shape of the fluid interface $h(x)$ is assumed to be close to the equilibrium configuration of a liquid wedge with constant slope, with an opening angle equal to the equilibrium contact angle. When the fluid velocity in the wedge is locally assumed to

correspond to a Poiseuille flow profile with a film thickness $\zeta = h(x)$,

$$u(z) = \frac{3U}{2\zeta^2}(-z^2 + 2\zeta z)$$

the energy dissipation rate in the wedge is given by

$$P_{\text{diss}} = \int_{x_m}^{x} \mathrm{d}\xi \int_0^{\zeta(\xi)} \mathrm{d}z\, \eta \left(\frac{\mathrm{d}u}{\mathrm{d}z}\right)^2 = 3\frac{\eta U^2}{\theta} \ln \frac{x}{x_m}$$

with x_m as the microscopic cutoff length (i.e. a molecular length scale) and x as the observation length. Setting these two equal, the de Gennes law for dynamic contact angles is obtained, with $l = \ln\left(\frac{x}{x_m}\right)$, as

$$U = \frac{\gamma}{6l\eta}\theta(\theta_0^2 - \theta^2)$$

This derivation does not hold for two immiscible liquids, as the dissipation in the second fluid is assumed to be negligible. With a more rigid derivation based on a self-similar solution for the shape of the interface close to the contact line Voinov[90] obtained the following relation for the dynamic contact angle of a liquid surrounded by an inviscid fluid:

$$\theta(x)^3 = \theta_0^3 + 9Ca\ln(x/x_m)$$

with θ_0 as the microscopic contact angle at the microscopic cut-off length x_m for given capillary number Ca and x as the distance from the contact line. While this derivation relaxes the requirement of small contact angles, a weakly curved interface with a slow change in the slope is still assumed. A more accessible derivation of the scaling law can be found in Ref. [24]. There is also a more generalized expression for two liquids with arbitrary viscosity ratio, as derived by Cox[18].

This scaling for the dynamic contact angle has been validated in a range of different scenarios[43, 72]. One problem with the validation of this model is that usually only the velocity-dependence of the macroscopic contact angle at fixed distance from the contact line is checked, with the slip length as fit parameter. One example where the height-dependent contact angle has been measured and fitted successfully with the Cox-Voinov scaling was published by Marsh *et al.*[44].

One point should be kept in mind when discussion this scaling law: Even in the original work[90] Voinov makes no claim that the microscopic cut-off is necessarily the slip length or attempts to discuss microscopic phenomena below the this length scale at which the microscopic contact angle is observed. Still it became canon that the microscopic length scale gives the slip length and θ_0 is the substrate contact angle according to Young. This is a good assumption for homogeneous substrates, but does not necessarily hold on heterogeneous substrates, where the substrate contact angle varies with the position on the substrate.

2.3.5 Unified modeling

As there were publications showing the validity of both approaches to model contact line dynamics in different limits and publications that attempted to show the transition between these two[26], the question of introducing a unified model incorporating both arose.

An attempt to unify the molecular-kinetic theory and bulk fluid dynamics was undertaken by Petrov and Petrov[51]. They argued to use a velocity-dependent contact angle of the form

proposed by Blake[11] as microscopic contact angle in the Cox-Voinov scaling. This gives a scaling according to Blake's predictions for low velocities, changing to a Cox-Voinov type scaling as the velocity increases.

As acknowledged by Blake[10] this approach gives a better experimental fit, at the price of introducing additional fitting parameters. It still does not account for the unavoidable mesoscopic defects on real surfaces.

2.3.6 Contact line dynamics on non-ideal substrates

Some analytical work has been done on the problem of contact lines on heterogeneous substrates. Raphael and de Gennes[59] gave analytical results for the pinning of a contact line at a single defect.

Joanny and Robbins[38] studied the problem of a driven contact line on a periodically patterned substrate, giving scalings for the effective contact line velocity with the driving force. Their work approximated the hydrodynamics of the contact line relaxation processes with an effective restoring force, an assumption that has not been adequately addressed to date.

Another work on the contact line dynamics on a heterogeneous substrate is the paper of Hocking[35]. He studied the response of a free interface when oscillating the substrate periodically both for homogeneous and heterogeneous substrates. The heterogeneity was assumed again to be represented by a constant advancing and receding contact angle over the whole substrate, though.

In general, most theoretical work on the dynamic contact angle observed on heterogeneous substrates was focused on the $f_{crit} + \varepsilon$ case where the driving forces in the system are only slightly above the depinning threshold f_{crit}. The scope of the present work are processes beyond this limit, where the time scales of interfacial relaxation and contact line motion are competing.

3 Methodology

The aim of this chapter is to introduce the methods used in this thesis to study the statics and dynamics of fluid interfaces in contact to solid surfaces. In the static case, when studying non-volatile liquids, the goal is to find a configuration of the free interface under a volume constraint where the sum of the energy of the fluid interface and the interfacial energy of the wetted substrate has a local minimum. When taking an alternative point of view, the conditions that an energetically extremal interface shape has to fulfill can be used to determine possible configurations. The two conditions that have to be fulfilled are the Laplace equation for the shape of the fluid interface and the microscopic contact angle that is determined by the wetting properties. Starting from a known droplet shape, the possible configurations can be followed under variation of the control parameters using numerical continuation. Control parameters in this context are for example the droplet volume, the amplitude of the wetting heterogeneity or the driving force. The numerical continuation was done using Auto07p[23]. The stability of the droplet shapes determined by this method can not be obtained by this method and has to be determined separately, for example by comparison to the energy landscape for the same system parameters.

In the third section, the main simulation method is introduced: To understand the dynamics of the droplet after depinning, the dynamics of a free interface in the Stokes limit are modeled using Boundary Element Methods (BEM). It is followed by a discussion of difficulties encountered during the implementation.

To compare the range of validity to another method for modeling the dynamics of fluid interfaces, this is complemented by a method to solve the thin film equation for systems with three-phase contact lines and Navier slip condition at the substrate. Additionally, the droplet dynamics are studied with a contact line dominated dynamics approach for comparison. In the contact line dominated dynamics model, the shape of the interface is assumed to be in the static equilibrium for a given contact line position, with the dissipation localised at the contact line. To account for the dissipation in this region, a constitutive law is introduced at the contact line that relates the deviation of the contact angle obtained by energy minimisation of the free interface from the contact angle determined by the substrate properties to the velocity of the contact line. With this law, the contact line position can change over time and droplet dynamics can be studied.

All systems discussed in the present work are two-dimensional / translationally invariant in the third dimension. Therefore, a droplet moving over a substrate does not have a contact line, but rather a front and a back contact point.

3.1 Static interface configurations from a free energy approach

Static fluid interfaces take energetically minimal configurations, i.e. the energy increases for any infinitesimal variation of the shape. On a homogeneous flat substrate, only one stable droplet shape exists, i.e. there are no additional local minima. On a heterogeneous substrate,

there can be a set of local minima. These describe different static configurations with different baselength, leading to contact angle hysteresis.

Introducing a volume force in the system is equivalent to introducing a potential that makes solutions that were displaced in direction of the volume force energetically more favorable. On a homogeneous substrate, the solution is invariant under translation. Therefore no more static solutions exist when a driving force is introduced, as the droplet can always reach an energetically more favorable state by displacement. In the heterogeneous case, stable droplet solutions are represented by local minima, which are generally not translationally invariant. Introducing a small volume force reduces the depth of the minimum, but does not necessarily eliminate it. Therefore, the locally stable solutions do not necessarily vanish when introducing a small driving force in the system.

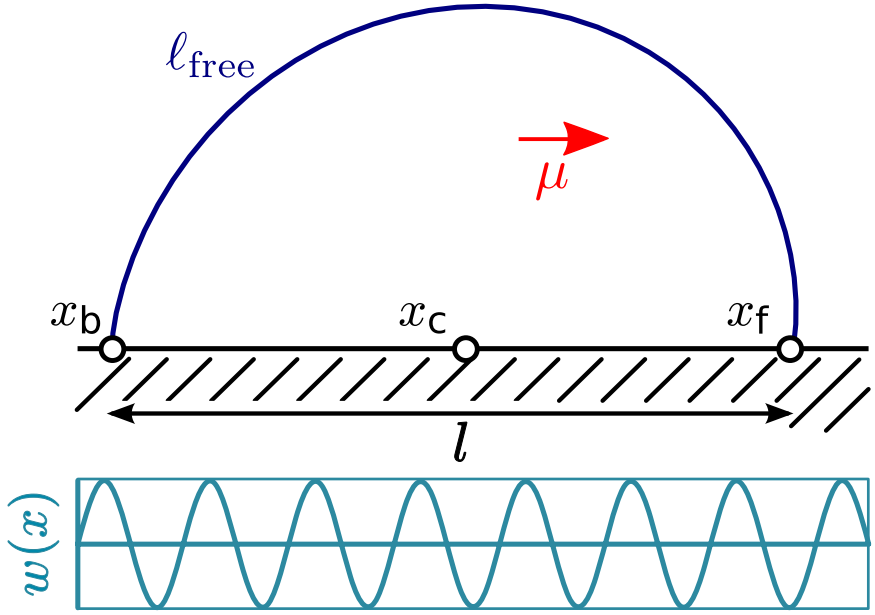

Fig. 3.1: Illustration of the model system, a droplet on a topographically flat substrate with position dependent wetting energy $w(x)$. The position of the front and back contact line are x_f and x_b, determining the droplet baselength l and center-of-base x_c. The driving force is given by μ, ℓ_{free} characterizes the length of the free interface. The droplet area and surface tension are normalized to unity.

In this section this approach is introduced for the model system of chapter 5, a droplet on a chemically heterogeneous substrate and a volume force pointing parallel to the substrate. Chemically heterogeneous in this context means that the substrate has a position dependent wetting energy. Figure 3.1 shows an illustration of the system. The position of the droplet on the substrate is described by the droplet baselength $l = x_f - x_b$ and the center-of-base $x_c = (x_f + x_b)/2$. The center of base is not necessarily the lateral position of the center of mass, as it can shift when the free interface is deformed by a driving force.

To model the static side of the depinning process, i.e. to determine for which range of parameters pinned solutions exist, a free energy consideration is employed. First, the minimal configuration of the free interface for any given position of the front and the back contact line is determined. This makes it possible to determine and present the energy of the droplet

configuration in dependence of of the baselength and center of base as energy landscape. By introducing this parameterization, the dimensionality of the system is reduced from the continuum of possible interface shapes of the droplet to the two coordinates describing the contact line positions. Minima in this energy landscape now represent stable stationary droplet solutions. When no more minima exist in this reduced configuration space, the only remaining class of solutions are moving droplets.

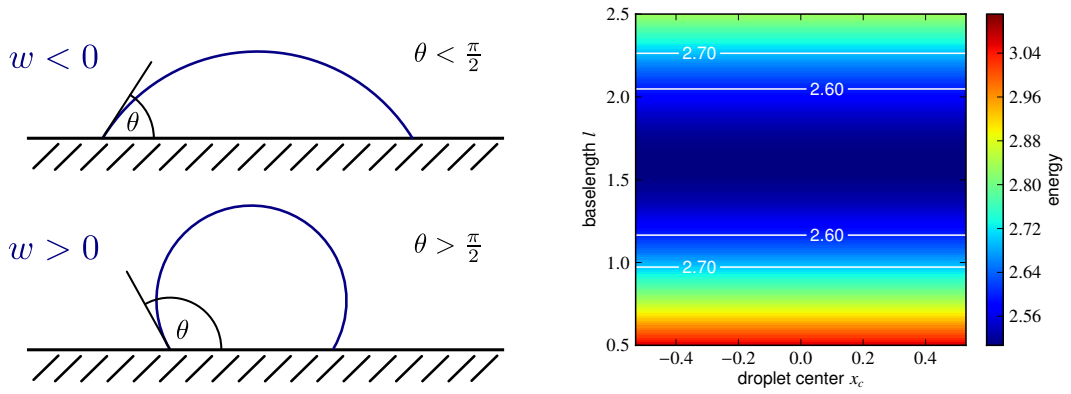

(a) (b)

Fig. 3.2: (a) Illustration of equilibrium droplet configurations on substrates with positive or negative wetting energies (b) Energy landscape for a droplet on a neutrally wetting substrate showing a translationally invariant local minimum for semi-circular droplets at $l = 1.59$, as this shape minimizes the length of the free interface

The total energy of the system can be separated in three contributions: E_{free}, the energy of the free interface, is determined by the length of the free interface and the surface tension plus the displacement of the center of mass compared to x_c:

$$E_{\text{free}}(x_c, l) = \min_{S \in S(l)} \{\gamma \ell + \mu(x_{cm} - x_c)\}$$

with $S(l)$ as the set of droplet shapes with the chosen baselength and x_{cm} as the center of mass. It depends on the base length l, and the volume force μ, deforming the droplet. This expression does not depend on the position of the droplet on the substrate, i.e. x_c, as the displacement of the center of mass to x_c stays constant. Therefore it gives a contribution to the energy landscape that is invariant along this dimension. The contribution $E_{\text{free}}(l)$ is determined by a minimization of the free interface for a given baselength l using Surface Evolver[15] in 2D mode with a fixed front and back contact point and the corresponding volume constraint. Figure 3.2(b) shows the energy landscape when only considering the contribution of the free interface. It is translationally invariant in x_c-direction and shows a minimum at the baselength that corresponds to a 90° contact angle, i.e. a half sphere.

E_{sub}, the wetting energy of the substrate covered by the droplet depends on the base length l, the center-of-base of the droplet x_c, and $w(x)$, the position-dependent wetting energy of the substrate and is determined by the integral

$$E_{\text{sub}} = \int_{x_c - l/2}^{x_c + l/2} w(x) \mathrm{d}x$$

It is independent of the driving force acting in the system or the shape of the droplet, if the position of the contact lines is the same. Summing up E_{free} and E_{sub} for a sinusoidal wetting pattern of the form

$$w(x) = w_0 + \Delta w \sin(2\pi k x)$$

results in the energy landscape displayed in Fig. 3.3, with a periodicity corresponding to the periodicity of the heterogeneity. This way, the

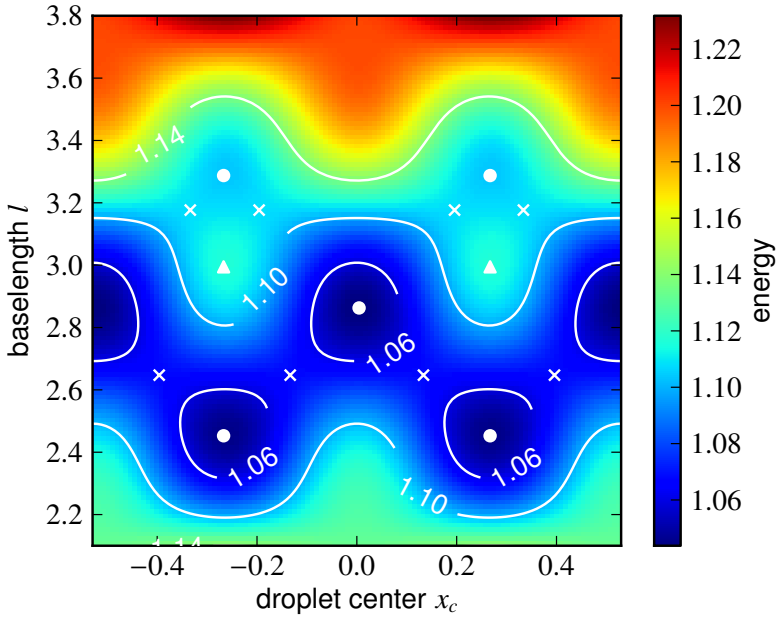

Fig. 3.3: Energy landscape of a droplet on a heterogeneous substrate with multiple local minima at different baselengths for $w_0 = -1/\sqrt{2}$, $\Delta w = 0.2$, $k = 5$. Points represent the local minima, crosses the saddle points and triangles the local maxima.

E_g, the contribution of the potential energy of the droplet, depends on x_c and the driving force μ. It is the energy obtained by displacing the droplet in the gravitational field driving the droplet, given by

$$E_g = -\mu x_c$$

. The total energy of a droplet configuration determined by l and x_c, depending on μ and $w(x)$ can be written as:

$$E(l,x_c)_{\mu,w(x)} = E_{\text{free}}(l)_\mu + E_{\text{sub}}(l,x_c)_{w(x)} + E_g(x_c)_\mu$$

While the first contribution has to be determined numerically for the case $\mu \neq 0$, as the interfacial shape deviates from the circular shape, the expressions for E_{sub} and E_g can be given analytically.

From this, the 2D energy landscape for a fixed driving force μ and heterogeneity $w(x)$ can be computed. Minima in this resulting $E(l,x_c)$ energy landscape represent pinned states of the droplet. As the driving force is increased, the amplitude of the heterogeneity can be reduced up to the point where no more local minima exist. This driving force where the

last minimum disappears defines the depinning force $\mu^{\uparrow}$ above which only moving droplets remain as solution.

Determining local extrema on a two-dimensional Energy landscape gets significantly faster when constraining the search to one-dimensional subspaces. This was done by first evaluating the expression

$$\frac{\partial E(l,x_c)}{\partial x_c} = 0$$

which contains only the analytical expressions for E_{sub} and E_g. Points where the derivative in x_c-direction vanishes have to fulfill the constraint:

$$\frac{\partial E_{\text{free}}}{\partial x_c} + \frac{\partial E_{\text{sub}}}{\partial x_c} + \frac{\partial E_g}{\partial x_c} = 0$$

which is equivalent to

$$0 + \frac{\mathrm{d}E_{\text{sub}}}{\mathrm{d}x_c} - \mu = 0$$

On the resulting one-dimensional subspace of the energy landscape where this constraint is fulfilled, the second requirement for a local extremum was evaluated numerically:

$$\frac{\partial E(l,x_c)}{\partial l} = 0$$

The signs of the eigenvalues of the Hessian obtained at these points determine the stability of the corresponding solutions.

3.2 Continuation of static interface configurations

An alternative to the interface minimization approach to obtain the static configurations of interfaces in a gravitational field is to compute shapes with a constant pressure directly. As the shape of droplets without overhangs can be written as $h(x)$ in the Monge representation, the goal is to find solutions to the equation

$$\text{const} = \gamma\kappa(x) - \mu x$$

with γ as the interfacial tension and μ as the volume force acting on the fluid. The curvature $\kappa(x)$ of the droplet given by

$$\kappa(x) = \frac{h(x)''}{(1+\alpha h(x)'^2)^{3/2}}$$

The boundary conditions of the problem are given by the contact lines that are constrained to the substrate and the substrate wetting energy at the contact line position, which determines the slope of the interface at the substrate, as described by Young's angle[95]. Additionally, an integral boundary condition is introduced for the volume constraint. Here, α represents a transition parameter to change the curvature term in the flat interface limit $\kappa(x) = h(x)''$ for $\alpha = 0$ to the full curvature term for $\alpha = 1$. Introducing this parameter is necessary, as the droplet shape using the reduced curvature term of the flat interface limit already deviates strongly from a spherical cap at a contact angle of 45°.

The solutions to this equation describing droplets on a chemically heterogeneous substate are obtained with the free software package Auto07p[23]. It is a tool for numerical continuation of solutions to ordinary differential equations. The code to treat this problem was developed with Prof. Uwe Thiele[33].

The process of numerical continuation of solutions starts with a solution of a differential equation with boundary conditions for an initial set of parameters. For a small change in one of the parameters, the variation of the solution can be computed. This way, solution families for different values of this parameter can be computed while keeping the other parameters constant. In this process, bifurcation points, where multiple solution branches meet, can be computed.

An example run for this problem takes the following form: The continuation was started with an analytical solution for the reduced curvature case $\kappa(x) = h(x)''$ on a homogeneous substrate without driving, so $\alpha = 0$, $w(x) = w_0$ and $\mu = 0$. This initial solution takes the form of a parabola with the appropriate slope at the contact points, with the curvature determined from the volume constraint. This initial solution was continued along the strength of the heterogeneity, giving the solution of a droplet on a substrate with the chosen strength of the heterogeneity. Then it is continued along the transition parameter α to enable the full curvature term, leading to a circular arc. From there, the solution is continued along the periodicity of the heterogeneity. For the chosen values of k, the obtained solution was continued along the driving force to the get the depinning diagram showing at which driving force no more stable solution exists. The free energy approach from the previous section was employed to determine the stability of the solution branches by comparing the obtained solutions to the extrema on the energy landscape for selected parameters.

Due to the Monge representation of the interface as $h(x)$, this method is limited to flat droplets without overhangs. While determining minima and saddle points in close proximity in shallow energy landscapes is difficult, with the continuation approach unstable solution branches can be followed up to the fold. This makes it possible to capture the turning points in the bifurcation diagram more precisely than the free energy approach. These states are especially important when studying the depinning transition.

Auto07p is also used in the section discussing the simplified coupled ordinary differential equation model for droplet dynamics to obtain static and time-periodic solutions.

3.3 Free interface flows in the Steady Stokes limit

To model the dynamics of the droplet after the onset of motion, we study the time evolution of a free interface in a flow dominated by viscous dissipation, as previously introduced. The idea is to determine the flow field corresponding to the distribution of normal stresses on the boundary and with this evolve the interface over time.

As the Stokes equation is a linear partial differential equation(PDE), the superposition principle holds. This implies that any flow field can be represented as a superposition of fundamental solutions to the PDE. The fundamental solution is the response of the system to a singular driving force acting on the system for a given set of boundary conditions, also referred to as Green's function. With the Green's function the Steady Stokes equation can be rewritten as a boundary value problem (BVP).

Following Pozrikidis[55, 56], the velocity field of the fundamental solution to the Steady Stokes equation in two dimensions with a singular driving force g located at x_0 of the form

$$0 = -\nabla p + \eta \nabla^2 u + \delta(x - x_0) g$$

$$\nabla u = 0$$

where p gives the fluid pressure, η the viscosity and u the velocity field has the form

$$u(x) = \frac{1}{4\pi\eta}\hat{G}(x,x_0)g$$

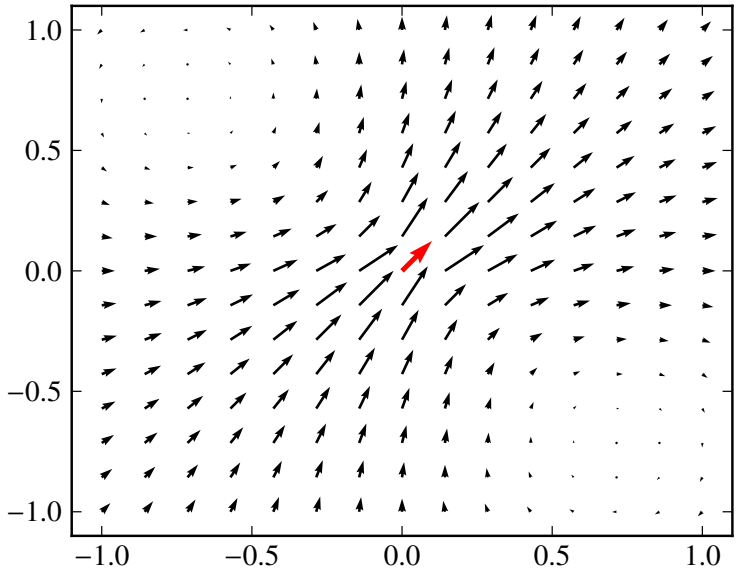

Fig. 3.4: Flow field (black) induced by a Stokeslet in the center of the system (red) pointing in (1,1) direction. Equivalent to the flow field around a small particle dragged with constant force through a viscous liquid in an unbounded domain. The distance at which the vortices are formed is determined by the characteristic length scale used for non-dimensionalisation.

with x as the position vector to the point where the flow field is evaluated and x_0 as the origin of the driving force. $\hat{G}$, the Green's function of a free Stokes flow, also known as Stokeslet, written in components, is given by:

$$G_{ij}(x,x_0) = -\delta_{ij}\ln r + \frac{(x-x_0)_i(x-x_0)_j}{r^2}$$

with $r = \sqrt{(x-x_0)^2}$ and i,j,k as indices for the component in Carthesian coordinates. The flow field corresponding to a points force pointing in (1,1) direction is illustrated in Fig. 3.4.

Together with the stress Green function, as given by

$$T_{ijk}(x,x_0) = -4\frac{(x-x_0)_i(x-x_0)_j(x-x_0)_k}{r^4}.$$

the flow velocity for a point x_0 within a closed domain C can be obtained from the velocity and surface force represented by $u(x)$ and the normal component of the stress $f(x) = \sigma(x)n(x)$ (with n as the normal vector on the domain boundary) from

$$u_j(x_0) = \frac{1}{4\pi\eta}\int_C G_{ji}(x_0,x)f_i(x)dl(x) + \frac{1}{4\pi}\int_C u_i T_{ijk}(x,x_0)n_k(x)dl(x) \tag{3.1}$$

C represents the contour of the droplet volume. The point x_0 can be taken at any point in the fluid volume, also at the domain boundaries. This gives a self-consistency problem to solve on the boundary in terms of $u(x)$ and $f(x)$, with x on the domain boundary. The idea is that the velocity obtained from eqn. 3.1 for a point at the boundary on the left hand side of the equation has to be consistent with the velocity on the boundary on the right hand side.

In the case studied here, there are two different kinds of boundary conditions: First, the boundary condition of a free interface, given by the normal stress. It is determined by the mean curvature plus the contribution of the volume force. Second, the boundary condition of a solid substrate with Navier slip condition, as introduced previously.

To treat this problem numerically, the boundary is represented by a linear elements with increased refinement close to the contact line region. After solving the boundary value problem self-consistently, the free interface is evolved in the time step with the obtained normal velocity. On the last element of the free interface at the contact line, a position-dependent microscopic contact angle is enforced to introduce the heterogeneity of the substrate wetting energy.

The advantage of BEM is that only the domain boundary has to be taken into account. Compared to finite element methods with volume elements where the bulk has to be resolved to calculate the time evolution of the flow field, less discrete elements are required to obtain the same resolution. With an appropriately chosen non-uniform distribution of interface elements, the relevant region around the contact line can be resolved over multiple orders of magnitude. The disadvantage of using BEM compared to directly solving the Stokes equation in the bulk is the densely populated interaction matrix representing eqn. 3.1, as the interaction terms from the Green function go beyond the next neighbours. Solving the boundary value problem involves inverting this matrix. As the matrix is densely populated, the inversion problem becomes computationally significantly more expensive compared to the sparse matrices occurring in volume-mesh-based methods.

A similar method was already utilized by Schleizer *et al.* in [67] to model moving droplets, but with the assumption of a no-slip boundary condition. Instead, the finite element size at the contact line which results in a non-vanishing velocity at the collocation point is used to implement a slip condition at the contact line. The discretization used for the simulations is chosen such that the "numerical slip" becomes negligible compared to the slip included in the model.

The following subsections discuss the implementation of the Stokes solver using boundary element methods with time evolution of the free interface. The two most important reference books for the implementation were Ref. [55] for the theoretical foundation and Ref. [54] for practical implementation recommendations. An overview article of Pozrikidis about "Interfacial Dynamics in Stokes Flow" is Ref. [56]. The basic flow of the BEM algorithm is:

1. Set up the geometry with the corresponding boundary conditions
2. calculate the interaction integrals
3. solve the matrix problem
4. evolve the interface, introduce the contact line model
5. remesh the grid, update boundary conditions
6. (write the current system status to disk, optional)

7. goto 2

Each of these parts posed certain challenges that are insufficiently documented in the literature and will be addressed in the following subsections separately. The code was developed mainly in Python (available at http://www.python.org) for the ease of use together with Scipy (available at http://www.scipy.org) for fast array operations. Especially performance critical parts of the program were written in C, as described in the section “Optimization”.

3.3.1 Set up the geometry

The boundary of the liquid domain forming the droplet can be considered to be composed of free interface segments and solid segments. The segments are composed of a series of linear elements, described by markup points at their ends and a collocation point in the center, where the stresses and velocities are determined. The boundary conditions parallel and normal to the free interface are

$$f_{\parallel} = 0$$

$$f_{\perp} = \kappa + \mu x$$

with κ representing the curvature of the interface over the segment and μ the equivalent hydrostatic pressure to represent the volume force. The curvature is given by:

$$\kappa = \frac{\mathrm{d}\theta}{\mathrm{d}S}$$

with θ, the tangential angle and S, the arc length parameter. A numerical estimation at the markup points between segments i and $i+1$ can be given as

$$\kappa = \frac{(\theta_{i+1} - \theta_i)}{(l_{i+1} + l_i)/2}$$

with θ_i as the angle of the tangent vector of the corresponding segment with the surface normal and l_i its length. The curvature at the collocation point was chosen as average of the two curvatures determined at the neighbouring markup points.

The boundary conditions for the solid segments are $u_{\perp} = 0$, the non-penetration condition, and $u_{\parallel} = u_0 + \frac{l_s}{\eta} f_{\parallel}$ to represent a wall driven with a constant velocity and Navier slip condition.

When driving a fluid interface over a heterogeneous substrate, the strongest variation of the interface shape is expected to occur close to the contact line. Therefore, a non-uniform distribution should be used with an increased refinement close to the contact line. The spacing has to fulfill the following criteria: The distance of the first collocation point from the substrate is an input parameter. The length of the elements should be approximately constant for the first elements and then increase continuously. The length scale up to which this non-uniform spacing should be employed can be chosen independently of the number of elements to be used in this region.

Therefore, the contact line region is resolved more detailed with a spacing between the elements of the form

$$h_i = i h_{\min} \left(\frac{h_{\max}}{N h_{\min}}\right)^{(i-1)/(N-1)}$$

with i as the counting variable, $h_{\min}$ as the height of the last element, $h_{\max}$ as the height up to which the system should be discretised and N as the number of elements in the contact line

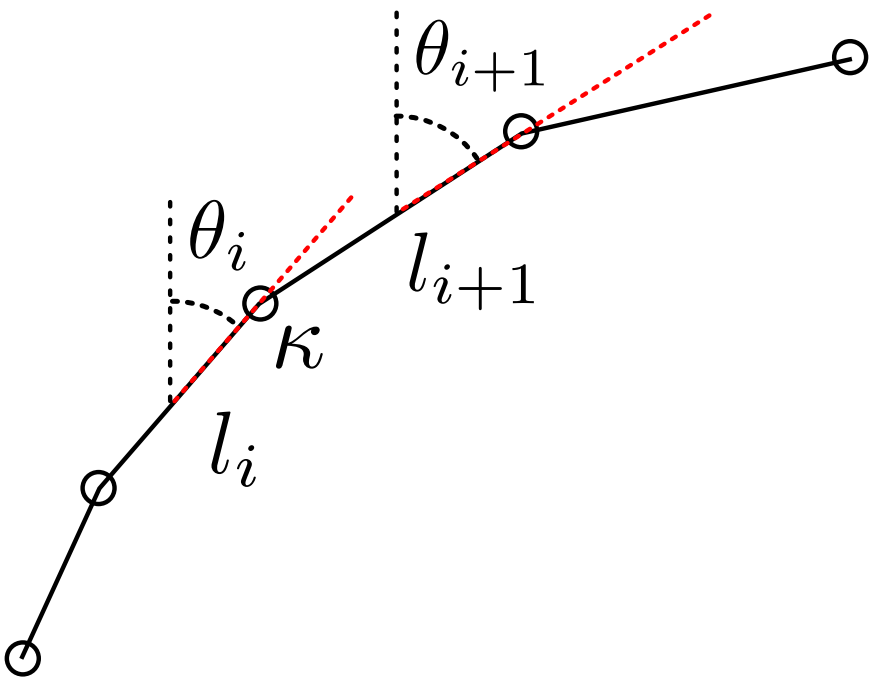

Fig. 3.5: Illustration of the curvature estimation on the free interface

region. This distribution of heights gives nearly uniform element length close to the contact line with $h_i \approx ih_{\min}$ that increases significantly as it approaches $h_{\max}$. The remaining part of the free interface is discretised using an element length approximately equal to $h_N - h_{N-1}$.

The minimal element size has been chosen approximately one order of magnitude smaller than the slip length in the system. When using an element size of the same scale as the physical slip length introduced in the system, the "numerical slip" due to the discretization will increase the effective observed slip length significantly.

3.3.2 Calculate the matrix entries

The matrix elements in the discretised form of eqn. 3.1 take the form of an integral over the ith element with a source stokeslet or stresslet at the position of the collocation point:

$$A_{ji} = \frac{1}{4\pi\eta} \int_{C_i} G_{ji} dl$$

for the Green function and

$$B_{ji} = \frac{1}{4\pi} \int_{C_i} T_{ijk} n_k dl$$

for the tensor of the stress Green function. These expressions are straightforward to evaluate, but the self-interaction integrals where $i = j$ will contain singular terms.

The entries for the A and B matrices were calculated by numerical integration over the corresponding element with the adaptive integrator for functions with an integrable singularity(QAGS function) of the Gnu Scientific Library[27]. It can integrate over the singularities of the Green function arising when x_0 lies on the element by adaptively applying the Gauss-Kronrod 21-point integration rule together with the Wynn epsilon-algorithm to speed up convergence, as described in the GSL manual.

It is possible to integrate first over the stress Green function and then take the product with the normal vector. But taking the product first is recommended, since it halves the number of required integrals. Also, for the self-interaction terms A_{ii} and B_{ii}, using the analytical expression where available is recommended. While the integrator works with integrable singularities, the performance is significantly lower than on non-singular elements.

3.3.3 Solve the matrix problem

First, the matrix entries have to be transformed in the normal/tangential basis of the individual elements to express the boundary conditions in terms of normal and tangential components, as presented previously. Equation 3.1 in the discretised form, with $*$ signaling the transformed base, takes the form:

$$u_j^* = A_{ji}^* f_i^* + B_{ji}^* u_i^*$$

Using the delta-function, the following linear equation has to hold for all j:

$$0 = A_{ji}^* f_i^* + (B_{ji}^* - \delta_{ji}) u_i^*$$

The coefficients in these equations can now be sorted to construct a vector of known quantities. This results in a matrix problem for the velocities and stresses not determined by the boundary conditions of the problem.

After solving the problem using a general solver suitable for dense matrices from a standard linear algebra package, the resulting normal and tangential velocities and stresses should be transformed back. At this point it is possible to reinsert the resulting velocity and stress terms in the original matrix equation to validate that the problem is solved self-consistently.

3.3.4 Evolve the Interface, introduce the Contact Line model

The obtained velocities at the collocation points in the center of the linear elements of the free interface are linearly interpolated to obtain the displacement velocity the markup points.

There are different approaches to introduce the local contact angle at the three-phase contact line in the model. An interfacial potential with a minimum at the substrate can be introduced to create a height dependent pressure term, similar to the precursor model. The estimator of the curvature at the contact line can be rewritten to incorporate the slope boundary condition or the slope of the last element can be set to the local equilibrium contact angle.

Since the interface is resolved down to an order of magnitude below the slip length, the interfacial contact angle is not expected to deviate strongly from the equilibrium contact angle. Therefore, the third option of enforcing the microscopic equilibrium contact angle on the last element was chosen.

3.3.5 Remesh, Refresh

Only moving the collocation points according to the normal velocities is insufficient, as the element length might change significantly over time. This leads to instabilities as the elements become too long or too short, making remeshing necessary. Two different approaches were taken for remeshing: In the channel geometry, the height distribution of the markup points was kept fixed, i.e. the markup points moved on horizontal rails with the projected velocity of the free interface.

The droplet case is not so straightforward, as the height of the droplet changes with time. In the contact line region, below a transition height chosen to be approximately 10% of the droplet size, the previously introduced non-uniform distribution of distances from the substrate for the markup points was chosen, and maintained. For the free interface of the droplet away from the contact line, the markup points were fitted with a third-order spline to obtain equally-spaced markup points again after the time evolution step.

Two other approaches proved unsuccessful: Simple linear interpolation to remesh the free interface lead to a significant volume loss. Algorithms that dynamically generated and eliminated segments at the point where the transition to the contact line region occurs encountered difficulties with the curvature estimator in this region. When an element became too short ($< 50\%$ of the target length) and was eliminated or stretched ($> 150\%$ of the target length) to the point that a new element was inserted, the local curvature became slightly discontinuous, which lead to an extra point stress and a displacement of neighbouring points.

3.3.6 Optimisation

There are two computationally expensive parts in the BEM code: the first consists of populating the matrix with the entries that result from evaluating the line integrals, the second is solving the matrix inversion problem. Calling the integrator from the gnu scientific library using the python wrapper introduced a significant overhead, as a python function call has to be handled whenever the Green function is evaluated at a point by it. Therefore this part of the code was handled in a C subroutine embedded in the code using `scipy.weave.inline`.

In test runs, the integrator still accounted for 80% of the runtime. This problem is easily parallelizable, since the integrals for computation of the matrix entries can be evaluated independently. This was done using an OpenMPI (http://www.open-mpi.org/) wrapper named mpi4py (http://code.google.com/p/mpi4py/) to distribute the calculation of the matrix elements over multiple processes. A significant speedup was achieved for up to 4 parallel processes performing the integrations, in which case the integrator accounted for about 55% of the runtime of the program. A point that might be addressed in the future is the implementation of a parallelized solver for dense matrix problem, but as this problem is still under active research in the computer science community[1], this was not attempted in the course of the present work.

The chosen discretization procedure with increased refinement close to the contact line keeps the number of elements low enough that the matrix inversion did not dominate the running time behavior of the code. The simulations in the present work were run with approximately 300-500 collocation points.

3.3.7 Testing

The correctness of the code has been checked with the following tests. They are used to ensure each part of the code behaves as intended and the physics is represented correctly:

- The integrator for the line integrals has been evaluated by setting up a closed domain of elements once around the singularity in the Stokeslet/Stresslet and once away from

[1] The content of a 2013 minisymposium at a SIAM conference on this topic can be found here: http://web.eecs.utk.edu/~luszczek/conf/siamcse2013_eigvalsolv/

it and checking the following identities, as presented in [54], with C as the contour of a control volume Ω:

$$\int_C n_i(x) G_{ij}(x,x_0) dl = 0$$

if x_0 is outside of the control volume, i.e. $x_0 \notin \Omega$:

$$\int_C T_{ijk}(x,x_0) n_k(x) dl(x) = 0$$

if x_0 is in the control volume, i.e. $x_0 \in \Omega$:

$$\int_C T_{ijk}(x,x_0) n_k(x) dl(x) = \delta_{ij}$$

If the precision of the integrator is insufficient, there will be a residue, i.e. the result of the integral will be not exactly zero or one.

- To validate the stress boundary conditions, a circular domain with a stress boundary condition of the form $f_\perp = \text{const}$, $f_\parallel = 0$ in an inviscid fluid was set up to confirm that the fluid velocities on the interface become zero.

- By replacing the circle with an ellipse and allowing for the ellipse to evolve, volume conservation has be verified and the relaxation time scale compared to published results, as presented in Ref. [78].

- For mixed boundary conditions, a box representing a gravity driven channel flow with periodic boundary conditions in x-direction and walls with partial slip in y-direction has been modeled. To confirm the slip condition is implemented correctly, this system has to exhibit a parabolic flow profile with an extrapolation length to zero velocity identical to the slip length. Another system that is suitable for testing is the deformation of a droplet in a shear flow, as discussed in Ref. [58].

- A simple free interface flow that has been studied extensively is a droplet spreading on a homogeneous substrate for different wetting conditions[82, 68]. In this system, the spreading velocity of a droplet depending on the baselength can be determined and compared to the analytical scaling given by Tanner[82].

As the main test if free interface flows are simulated physically correct, it was checked if the Cox-Voinov scaling for the shape of a moving fluid interface close to the contact line is obtained. For this, a droplet in a shear geometry is simulated. In this geometry a droplet is located between two substrates with Navier slip condition at the top and the bottom that move in opposing direction with constant velocity.

The free interface forms a straight line in equilibrium as the top and bottom wall were chosen to be neutrally wetting, i.e. with a substrate contact angle of 90°. Therefore, the observed interfacial configurations for moving substrates should agree with the predictions for interface configurations derived as perturbations from a moving fluid wedge.

The code can be validated by confirming that the obtained steady profile of the free interface for a homogeneous substrate fulfills the Cox-Voinov relation. The self-similar solution for the shape of a moving contact line, as discussed previously, is:

$$\theta(x)^3 = \theta_0^3 + 9Ca \ln(x/l_c) \tag{3.2}$$

with θ_0 as the microscopic contact angle, x the distance to the contact line, and l_c a microscopic length scale determining the lower cutoff.

The numerical simulations confirm the scaling for the intermediate length scales above the slip length and an order of magnitude below the system size. Above this length scale, the macroscopic solution determined by recirculation in the bulk flow away from the contact line determines the shape of the fluid interface. The scaling and the deviation for small and high distances can be seen in Fig. 3.6(b), which shows the obtained stationary solution plotted according to the equation 3.2. When studying the non-steady states of the interface before it reaches an equilibrium, the capillary velocity Ca used in the equation should not be determined with the driving velocity of the system, as shown in Fig. 3.6(a), but with the current velocity of the contact relative to the substrate, as shown in Fig. 3.6(b). Even before the global steady state is reached, the fluid interface follows the scaling law in a region close to the contact line, when rescaling with the local contact line velocity.

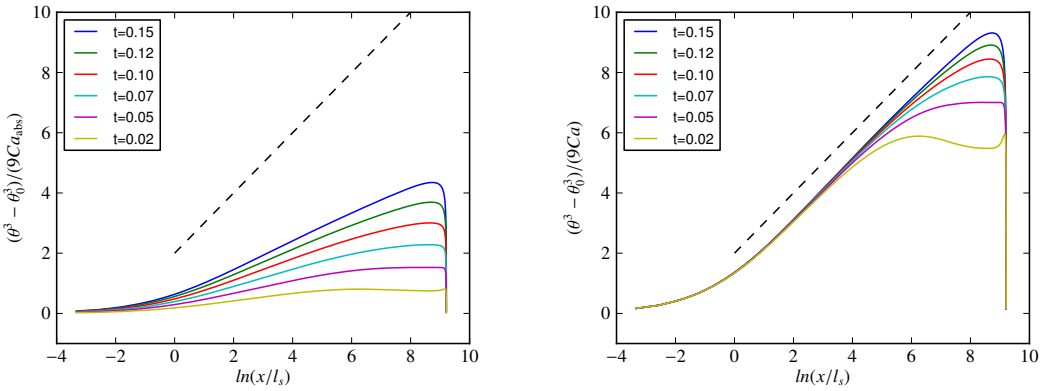

(a) (b)

Fig. 3.6: Slope of the fluid interface over distance to the contact line for different times as it approaches the steady state, rescaled to show logarithmic dependence with the distance from the contact line of the Cox-Voinov scaling for $l_s = 1.0 \cdot 10^{-4}$, $Ca = 0.05$. (a) rescaled with the capillary number of the system and (b) rescaled with the capillary number determined by the contact line velocity relative to the substrate. The dashed line shows a unit slope.

An interesting aspect is the fact that the microscopic length scale, i.e. the point where the scaling law approaches θ_0, in the equation is not exactly the slip length of our system. If this was the case, the extrapolated line from the linear regime in the plot would cross the origin (0,0) in the graph. The most probable explanation for this is that during the derivation of the scaling law it is assumed that the microscopic contact angle θ_0 gives the slope of the interface at the lower cut-off height l_c. In contrast to that, in our system the microscopic contact angle is enforced on the last element, given by the last data point in Fig. 3.6(b), around one order of magnitude below the slip length. That means the contact angle observed at l_s will already deviate slightly from the equilibrium contact angle due to the hydrodynamic deformation taking place in the slip region.

It was also attempted to show the Cox-Voinov scaling for initially curved interfaces. The influence of the curvature on the equilibrium shape of the fluid interface is not negligible

for more than one order of magnitude below the system size and could not be corrected for, therefore the attempt to resolve the scaling in space for that system did not succeed.

3.4 Time dependent thin film equation

To compare the results obtained for droplets with the boundary element method with the results from the lubrication approximation, a solver for the thin film equation with "sharp" contact lines and Navier slip condition was implemented. Implementing code for the thin film equation with a precursor film is easier, as it allows for periodic boundary conditions with a fixed domain on which the function is evaluated. On the other hand, with the sharp contact line approach the results can be compared directly to the BEM simulations. Also, as there is no precursor film, no flow through the precursor film has to be considered.

If the film thickness is small compared to the length scale on which the film thickness changes and the slip is small compared to the film thickness, it can be assumed that the flow profile is locally equal to the profile in a film with homogeneous thickness and constant pressure gradient[6, 48], given by a parabola. In this case the fluid mobility, i.e. the volume flux Q over the pressure gradient $\partial_x p = \frac{\partial p}{\partial x}$ is given by

$$\frac{Q}{\partial_x p} = \frac{h^3}{3} + l_s h^2$$

with h giving the film thickness and l_s the slip length of the substrate. For non-dimensionalization, the surface tension γ, the viscosity η and droplet volume were set to unity. Together with the approximation of the curvature for flat interfaces where $\kappa = \partial_{xx} h$, as introduced previously, the thin film equation takes the form

$$\partial_t h(x,t) = -\partial_x Q = -\partial_x((h^3/3 + l_s h^2)(\partial_x(\partial_{xx} h + \mu x)))$$

with h as the position and time dependent film thickness, l_s as the slip length and μ as the driving force parallel to the substrate.

The position of the droplet on the substrate and the microscopic equilibrium contact angles θ_l, θ_r give the boundary conditions at the position of the contact lines x_l and x_r as $h(x_l) = 0$, $h(x_r) = 0$, $h'(x_l) = \tan(\theta_l)$, $h'(x_r) = -\tan(\theta_r)$.

To determine the time evolution of the free interface, the fluid interface is discretised in space as (h_i, x_i) with a second-order estimator for the curvature[75]. As the droplet base-length changes with time, it is necessary to introduce an additional evolution equation for the support according to the kinematic boundary condition on the contact lines. This allows for a varying baselength while making sure that the support points are maintained at equal spacing. The height evolution equation was modified accordingly to account for the moving frame of reference.

Directly enforcing the microscopic contact angle on the last element lead to numerical instabilities in this system, therefore the slope boundary condition is accounted for by a numerical estimator for the third derivative that incorporates the boundary condition. The modified curvature estimator is presented in the work of Souza[75]. A standard curvature estimator is based on inverting a Taylor expansion. Instead using higher derivatives of a function in a point x_i to estimate the shape of the function in the proximity, the shape of the function is used to estimate a higher derivative in x_i. This can be rewritten to consider not only the function values at neighbouring points $x_{i\pm1,2,\ldots}$, but also derivatives at those determined by

the boundary conditions. This approach can also be extended to non-constant spacings of the support points. The resulting set of 2N ordinary differential equations is integrated using the LSODA[52] library. The result is a time series $(h_i, x_i)_{t=t_j}$ of the interface profiles.

3.5 Effective contact line dynamics

It was proposed by Santos *et al.*[63] that in the limit of small slip lengths, it can be assumed that the dynamics is dominated by effects close to the contact line. To study droplets in this limit and to validate up to which point this model holds, a quasi-static model of contact line dynamics can be introduced, similar to the work of Joanny and Robbins[38]. The assumption is that the macroscopic droplet shape represents a minimum of the interfacial energy for a given contact line position without hydrodynamic contributions, as described in section 3.1.

The motion of the contact line is now determined by the uncompensated Young stress due to the difference between the macroscopic contact angle θ given by the droplet shape and the prescribed microscopic equilibrium contact angle θ_0. The contact line velocity is given by

$$x' = \alpha(\cos(\theta) - \cos(\theta_0))$$

with α being a friction coefficient setting the time scale of the droplet motion. It can be argued if instead of the stress imbalance at the contact line, as used here, an expression in higher powers of θ should be used. One example would a law similar to Cox-Voinov, where the contact line velocity u displays a scaling of the form $u \propto \theta^3 - \theta_0^3$. As this model can only hold for small velocities and correspondingly small contact angle deviations, most models of such a form can be linearized to a form as presented here.

When considering the specific case of a droplet on a substrate, the shape of the droplet is determined by minimizing the energy functional under a volume constraint for different base length l at the chosen driving force using Surface Evolver, as described in the previous section. The obtained front and back contact angles depending on the driving force and base length were stored in a lookup table. On this dataset, a linearly interpolating function was applied, giving functions $\theta_{f,b}(l)$. Using this, the system of ODEs given by

$$x'_{(f,b)} = \pm\alpha(\cos(\theta_{(f,b)}(x_f - x_b)) - \cos(\theta_0(x_{(f,b)})))$$

was integrated to obtain the droplet motion in the quasi-static limit. The advantage of this approach is that it is not necessary to run the shape minimization after every time step to obtain the solution.

The model can be extended when a characteristic length scale on which the effect of the heterogeneity can be observed has been established. This is one of the points to be discussed in the following chapter.

4 Dynamic contact angles on heterogeneous substrates

Moving contact lines on homogeneous substrates received a lot of attention over the last 40 years[18, 90, 91, 25], as mentioned previously. When treating the problem of a fluid interface driven with constant velocity analytically, the goal is to obtain stationary solutions to the Stokes equation describing the time evolution of a free interface flow that fulfill the boundary conditions, as given by the slip length and the contact angle. On a substrate with a wetting energy that varies with the position on the substrate, a stationary solution will not fulfill the condition of a varying contact angle at the contact line. Therefore understanding the dynamics on a spatially periodic patterned substrate requires the computation of time periodic solutions. This is a step towards a deeper understanding of contact line dynamics on generalized, i.e. not necessarily periodic, heterogeneous surfaces.

For the case of a homogeneous substrate, predictions can be made for the slope of the interface that can be observed at a given distance from the contact line[18]. This is not the case for surfaces with a position dependent wetting energy. There, such a simplified model that relates the dynamic contact angle, i.e. the slope of the interface at a certain distance from the contact line, with the wetting properties of the substrate and the driving applied to the system for a given macroscopic geometry is missing.

Two main cases can be distinguished in which driven contact lines can be studied: In one case, the fluid front is driven with a constant velocity and in the other case, with a constant force. In this chapter, the case of driving with a constant velocity is studied. In the following chapter, the problem of a droplet driven by a constant force is considered.

This section first presents the observations from studying the time evolution of free interfaces driven over a topographically flat substrate with a sinusoidally varying wetting energy in the Steady Stokes limit. In the geometry shown in Fig. 4.1, the observed dynamic contact angles in dependence of the substrate wetting energy and observation height are studied. It shows how the interface fluctuations are reduced with increasing distance from the contact line and increased driving velocity. It also shows how the sampling of the microscopic contact angle through the contact line influences the dynamic contact angle observed away from the contact line.

To separate the deformation of the free interface due to viscous stresses from the deformation of the global shape due to the variation of the microscopic contact angle, this is followed by a section on the response of a stationary fluid interface to a contact angle that is varied periodically in time. The response of the contact line depending on frequency and amplitude of the contact angle variation is studied. The response of the contact line is characterized the displacement over time and the height up to which the variation can be observed. As the driving frequency is increased for a given wetting energy contrast, the displacement is reduced and a phase shift between the driving signal and the displacement occurs.

The problem of a contact line moving over a structured substrate is closely related to a time periodic variation of the contact angle. In both cases the microscopic contact angle at

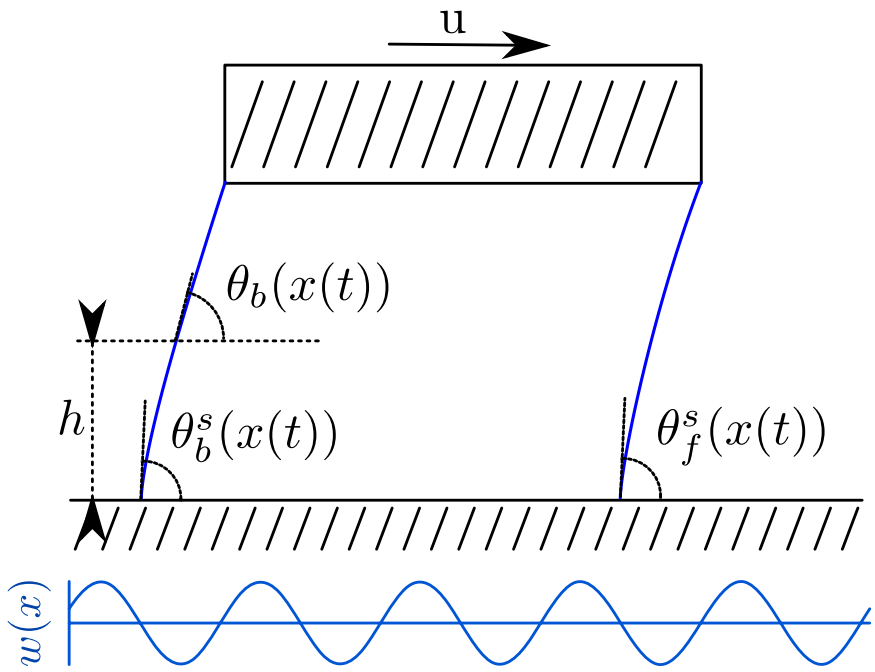

Fig. 4.1: Illustration of the system with the droplet pinned at the top moving over a substrate with fixed velocity u. The position dependent wetting energy $w(x)$ of the substrate is sketched underneath. It determines the contact angles $\theta^s_{(f,b)}$ at the contact lines depending on time and contact line position. At every height h a macroscopic contact angle $\theta_{(f,b)}$ can be defined from the local slope of the interface.

the contact line varies with time. In one case, it varies with the position of the contact line on the substrate, that changes with time as the contact line moves. In the other case, it varies directly with time. This connection makes it possible to construct a simplified model for the contact line motion over a heterogeneous substrate. The idea is to use a mode expansion of the displacement to represent the displacement of the contact line compared to the equilibrium position as superposition of responses to time periodic contact angle variations. From this, the effective velocity dependent microscopic contact angles can be obtained. The relations for the contact line displacements and time averaged microscopic contact angles are compared to the full dynamical simulations and show a good agreement. Finally, this is compared to a simplified model based on a contact line friction approach currently considered suitable, similar to the work of Joanny[38].

4.1 Droplet in a shear geometry

The system under consideration, as presented in Fig. 4.1, is a droplet with pinned contact lines at the front and back end of the top plate. This plate pulls the droplet with constant velocity over a topographically flat substrate with a position dependent wetting energy. The droplet is surrounded by an inviscid fluid. In this geometry both the time dependent dynamic contact angle at the advancing and receding front can be studied at a given distance from the contact line for different driving velocities. One example where a similar geometry might be

used is an immersion lithography setup, where the droplet is pulled by the projection optics over the wafer[49].

The spatially periodic wetting energy that determines the local equilibrium contact angle of the substrate was chosen as

$$w(x) = w_0 + \Delta w \cos(2\pi k x),$$

with w_0 being the spatial average wetting energy, Δw determining the amplitude of the wetting energy variation and k as the periodicity. The system is non-dimensionalized with the characteristic length scale given by the channel width, the surface tension and viscosity set to unity. For the simulations presented here, the distance between the pinning sites of the front and the back contact line at the top was chosen as two times the channel height. Including both contact lines makes it possible to study the case of an advancing and of a receding contact line in one simulation run. Additionally, it provides a natural closure for the domain under consideration.

Unless noted otherwise, the simulations presented here were run with an average wetting energy $w_0 = 0$, resulting in a 90° contact angle and a straight interface in equilibrium, by setting the droplet volume to 2. This brings the initial configuration of the system closer to the assumption of moving contact lines as perturbations of a wedge solution and eliminates the difficulties associated with separating between the dynamic deformation and the inherent curvature of a macroscopic solution with non-zero Laplace pressure.

4.1.1 Different measures for the dynamic contact angle

Before considering heterogeneous substrates, the case of a contact line moving over a homogeneous substrate has to be considered. Obtaining a good estimation for a dynamic contact angle is difficult, especially in experiments. A commonly used approach is fitting the observed interface shape close to the contact line with an analytical function to obtain an extrapolated macroscopic contact angle. This approach is sensitive to the resolution limits of the method used to visualize the fluid interface in the experimental setup. This point is highlighted in the experimental work of Marsh *et al.*[44], which studied the dependence of the dynamic contact angle on the distance from the substrate.

In numerical simulations the shape of the interface can be evaluated at arbitrary heights. This makes the local slope of the interface easily accessible and makes it possible to investigate the effect of the length scale on which the slope is observed. The observed interface shapes at different driving velocities are illustrated in Fig. 4.2(a). The advancing fluid interface is depicted, with the point fixed at height $h = 1$ moving to the right. As the driving velocity is increased, the viscous bending and the displacement of the contact line compared to the equilibrium position increases. Fig. 4.2(b) shows the obtained dynamic contact angles over the driving velocity when measuring at different interface distances from the contact line. As expected, the deviation from the microscopic contact angle increases with the shear velocity and the distance from the contact line.

All of these datasets are outside of the range of validity of the Cox-Voinov scaling, which breaks down already an order of magnitude below the system size, as shown in section 3.3.7. Nonetheless, when taking only the advancing or receding contact angles, all of them can be fitted reasonably well with the scaling law

$$\theta^3 = \theta_0^3 + 9Ca\ln(h/l_{\text{fit}}) \tag{4.1}$$

when fixing the equilibrium contact angle $\theta_0 = \pi/2$ but leaving the slip length in the logarithm as fitting parameter, as shown in Fig. 4.2(b). There, the dashed lines represent the result of a least-squares fit of the Cox-Voinov scaling and the legend gives the obtained microscopic length scale from the fit. Even though the agreement appears reasonably when considered visually, the obtained slip length from the fit significantly underestimates the slip length in the system, especially for high distances h.

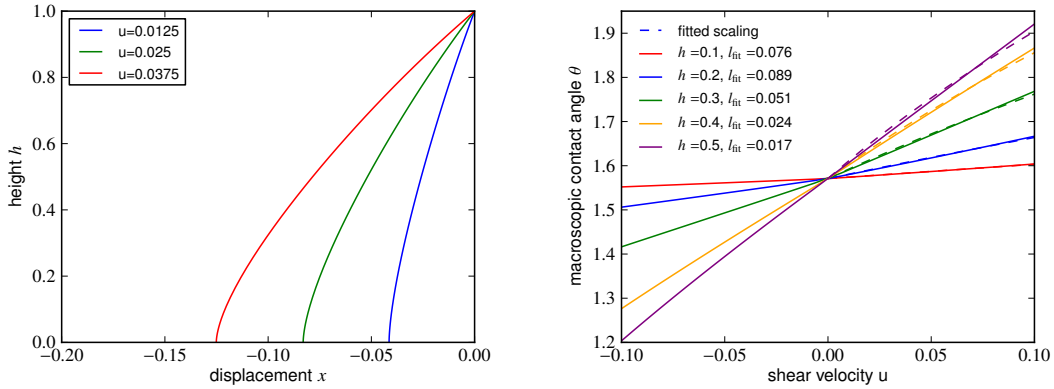

(a) (b)

Fig. 4.2: (a) Stationary profiles of an advancing fluid interface for different driving velocities u showing increased viscous bending with increasing velocity and distance from the contact line, $l_s = 0.1$ (b) Observed contact angle at different heights h in the channel with homogeneous, neutrally wetting substrate over driving velocity u. The graph illustrates the hydrodynamic deformation of free interface with increasing distance from the contact line. Dashed lines show the result of fitting the advancing contact angles with the Cox-Voinov scaling (eqn. 4.1) with the slip length l_{fit} determined from the fit, as shown in the legend. For all graphs: $w_0 = 0$.

Unless indicated otherwise, the macroscopic contact angle in the remaining section was chosen as the contact angle derived from the slope of the interface at $h = 0.5$, in the center of the channel.

4.1.2 Variation of contact angle over time

When introducing a position dependent wetting energy on the substrate, this system goes from a stationary solution for a given velocity u, where the moving contact line has a constant shape over time, to a time periodic solution. There, over the course of one period, the contact line will approach a defect, get displaced until the depinning point is reached and then relax back. Depending on the deviation of the initial configuration from the final state, it will take multiple periods for the system to reach this periodic state.

Most studies do not consider these fluctuations of the observed contact angle, as they are measuring on a length scale significantly above the characteristic length scale of the fluctuations, even on significantly heterogeneous substrates. This changes when going closer to the characteristic defect length scale, as done in this section, where the fluctuations and

their decay is still observable. Understanding these microscopic processes is fundamental to predicting the macroscopic contact angle that is observed in experiments.

Fig. 4.3(a) displays the microscopic contact angle at the position of the contact line, i.e. the wetting energy that the contact line is sampling over time for different velocities. A transition from a strongly stick-slip dominated motion to a more uniform sampling of the surface takes place. For high velocities, the time dependent microscopic contact angle at the substrate approaches the sinusoidal form of the spatial variation of the substrate wetting energy.

In the limit of high velocities, it can be expected the microscopic contact angle at the contact line over time approaches the spatial structure of the heterogeneity, as the relative effect of the wetting properties compared to the external driving decreases. In the limit of slow velocities, the system approaches the quasi-static limit of being trapped in the a local equilibrium with a relaxation process that occurs fast compared to the periodicity of the motion when the depinning event takes place and system moves to the next minimum. The contact line velocities observed for the different driving velocities are depicted in Fig. 4.3(b). While the variation in the contact line speed, i.e. the difference between the minimum and maximum contact line velocity, does not decrease with the shear velocity, the average velocity does increase. This reduced relative variation leads to a more uniform motion over the substrate.

Fig. 4.3(c) and 4.3(d) show the corresponding macroscopic dynamic contact angles that were observed at $h = 0.25$ and $h = 0.5$. The presented driving velocities are the same as in Fig. 4.3(a). It shows the constant offset in the observed contact angle that can be attributed to the deformation of the fluid interface due to viscous stresses. It also shows that the amplitude of the fluctuations decreases with increasing driving velocity. This indicates that the variation over the course of one period becomes increasingly localized at the contact line. Another interesting feature is the smoothening of the perturbation. While the deviation of the macroscopic contact angle at $u = 0.02$ is still clearly non-sinusoidal, it is less sharp than the jump of the microscopic contact angle. This localization of the fluctuations of the fluid interface is studied in the next section by employing a time periodic variation of the microscopic contact angle.

4.1.3 Dynamic contact angles on heterogeneous substrates

After studying how the contact angle varies over time at different distances from the contact line, the systematic change with the driving velocity and contact angle hysteresis can be considered. The relevant variables are now the minimum and maximum observed contact angle at a given height, in addition to their time averaged values.

Considering the macroscopic contact angle as the time averaged angle of the interface at the center of the channel, an increase compared to the homogeneous substrate can be observed for the advancing fluid interface and a decrease for the receding fluid interface. This is expected for a substrate with contact angle hysteresis. This is shown in Fig. 4.4(a), which presents the averaged macroscopic contact angle both for the homogeneous (blue) and heterogeneous (green) case, together with the minimal and maximal observed contact angle over one period (red).

An interesting point to consider is the offset between the time averaged macroscopic contact angle at fixed height for the homogeneous and heterogeneous case. With increasing velocity, the difference between the two contact angles is decreasing. This is at odds with the assumption that there is a static advancing and a static receding angle, that can be employed as microscopic contact angle in dynamic laws obtained for homogeneous substrates to describe

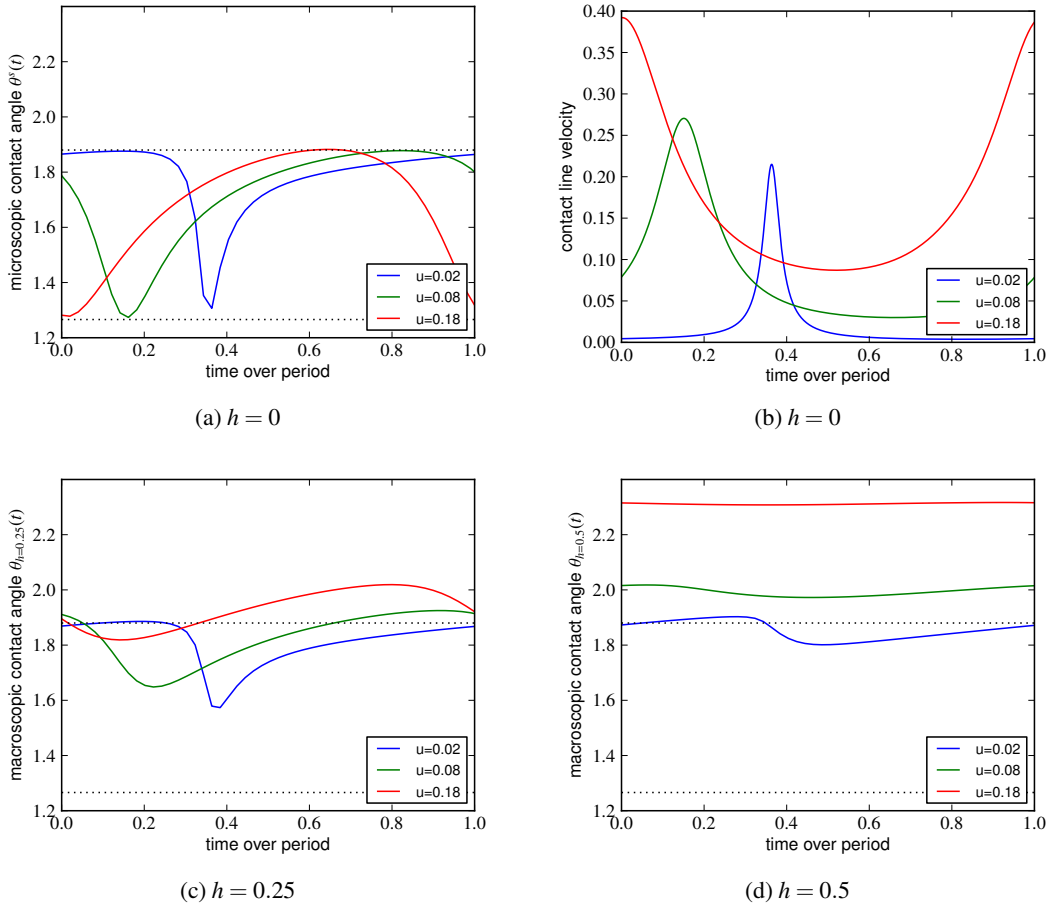

(a) $h = 0$ (b) $h = 0$

(c) $h = 0.25$ (d) $h = 0.5$

Fig. 4.3: (a) microscopic contact angle over one period for different driving velocities for $\Delta w = 0.3$, $k = 5$ showing the more pronounced stick-slip motion of the interface for lower velocities. In all cases, the full range of wetting energy gets sampled as the contact line moves continuously over the substrate, just with varying velocities. The dotted lines represent the minimum and maximum of the microscopic contact angle. (b) corresponding contact line velocities over time showing the transition from a pronounced stick-slip motion to a more continuous motion for higher velocities (c,d) macroscopic contact angle observed at $h = 0.25$ and $h = 0.5$, respectively, over one period for different driving velocities for $\Delta w = 0.3$, $k = 5$ showing the increased hydrodynamic deformation for higher velocities but decreased propagation of the contact angle variation. In all cases: $w_0 = 0$

the hydrodynamic bending. Having a constant advancing and receding contact angle would imply that the line is offset by a constant value in first order.

Another relevant measure is the minimal and maximal angle observed at that height. The strength of the fluctuation is decreased, as the driving velocity increases. It also decreases when observing the slope at a higher distance from the contact line. This indicates that there is a decay length associated with the fluctuations that decreases with the frequency of the

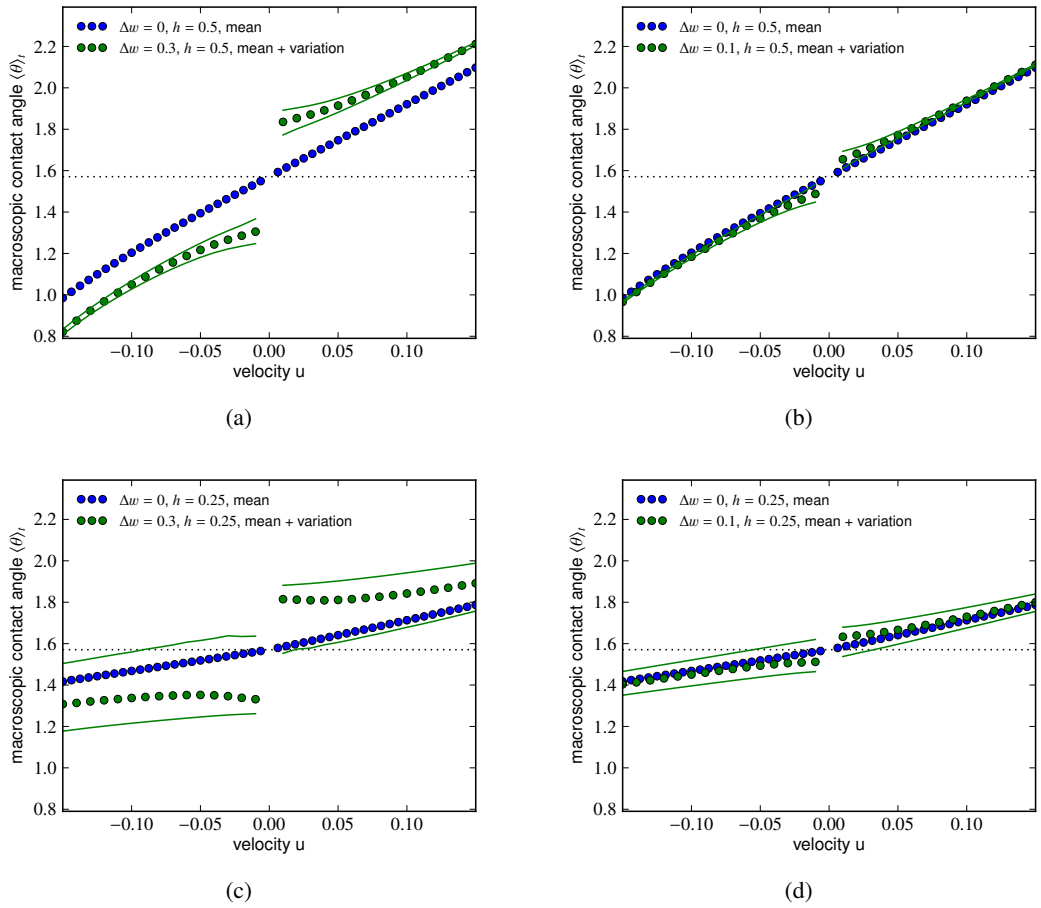

Fig. 4.4: Illustrating the effect of varying strength of the heterogeneity and observing at different distances from the contact line, (a) dynamic time averaged contact angles in for homogeneous (blue), heterogeneous (green) substrate with fluctuation of the contact angle over one period (red) for $\Delta w = 0.3$, $h = 0.5$; (b) dynamic contact angles in for homogeneous, heterogeneous substrate for $\Delta w = 0.1$, $h = 0.5$, showing reduced deviation for smaller heterogeneity
(c) dynamic contact angles in for homogeneous, heterogeneous substrate for $\Delta w = 0.3$, $h = 0.25$, showing increased fluctuation, small bulk contribution to contact angle compared to Fig. (a); (d) dynamic contact angles in for homogeneous, heterogeneous substrate for $\Delta w = 0.1$, $h = 0.25$. For all graphs: $w_0 = 0$, $k = 5$.

driving. Due to the constant periodicity of the substrate, a higher contact line velocity leads to an increased perturbation frequency. This point will be addressed later on in this chapter.

Figure 4.4(b) shows the same system with reduced heterogeneity and subsequently reduced contact angle fluctuation and hysteresis. The homogeneous case does not change, as the mean wetting energy of the substrate stays the same. The question is if it is possible to separate the contribution of the bulk fluid dynamics and of the wetting heterogeneity.

When changing the height at which the contact angle is evaluated from center of the channel (h=0.5) to a quarter of the height (h=0.25), as done in Fig. 4.4(d), the deformation due to viscous stresses and thus the apparent contact angle is decreased. On the other side, the fluctuation of the contact angle increased significantly, as the fluctuation of the free interface due to the heterogeneity is apparently damped with increasing distance from the contact line.

An special case is depicted in Fig. 4.4(c), as it shows how the time averaged macroscopic contact angle is first decreasing for a range of small velocities before, above $u = 0.05$, the hydrodynamic contribution overtakes. This can be accounted for by the microscopic contact angle, as will be discussed later. Another interesting aspect is the range of fluctuations, i.e. the difference between the minimum and maximum observed macroscopic contact angle. When going to $h \to 0$ it can be expected that the range of fluctuations will approach the advancing and receding microscopic contact angle determined by the minimum and the maximum of the substrate wetting energy.

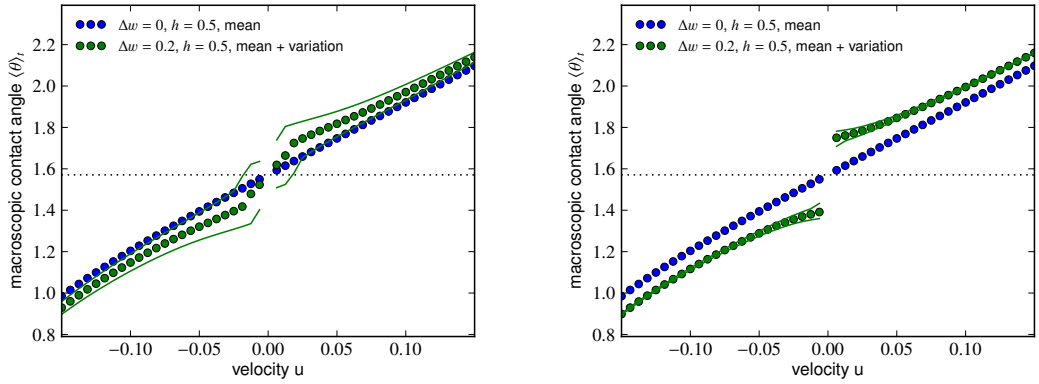

(a) (b)

Fig. 4.5: (a) Minimum, maximum and mean macroscopic contact angle for homogeneous and heterogeneous case with $k = 2$ (b) Minimum, maximum and mean macroscopic contact angle for homogeneous and heterogeneous case with $k = 10$ showing the decreased fluctuation of the angle with smaller characteristic length scale of the substrate heterogeneity. For both graphs: $\Delta w = 0.2$, $w_0 = 0$

The effect of a changed periodicity is shown in Fig. 4.5(a) and 4.5(b). With an increased periodicity, the fluctuation amplitude observed for a given velocity is decreased. The largest difference is visible in the regime of low velocities, there the $k = 10$ case approaches smoothly a constant value, while the contact angle observed on the heterogeneous substrate in the case $k = 2$ seems to decrease and approach the average contact angle of the substrate. The underlying process of this effect will be revisited at the end of the chapter.

On a homogeneous substrate, the microscopic contact angle approaches the macroscopic contact angle as the velocity goes to zero and the system approaches the quasi-static case. Comparing the time averaged microscopic and macroscopic contact angle for the heterogeneous substrate, as done in Fig. 4.6(a), shows that this also holds for the case with inhomogeneous wetting energy. There, the system stays in the pinned, locally stable state until it becomes unstable. The onset of instability results in a sudden transition to the next stable state that is fast compared to the driving speed. This is equivalent to the quasi-static limit,

as this process is independent of the capillary number. For increasing velocities, it can be observed that the time averaged microscopic contact angle decreases, as it approaches the spatial average of the substrate contact angle. The observed macroscopic contact angle on the heterogeneous substrate also approaches the macroscopic contact angle observed on the homogeneous substrate.

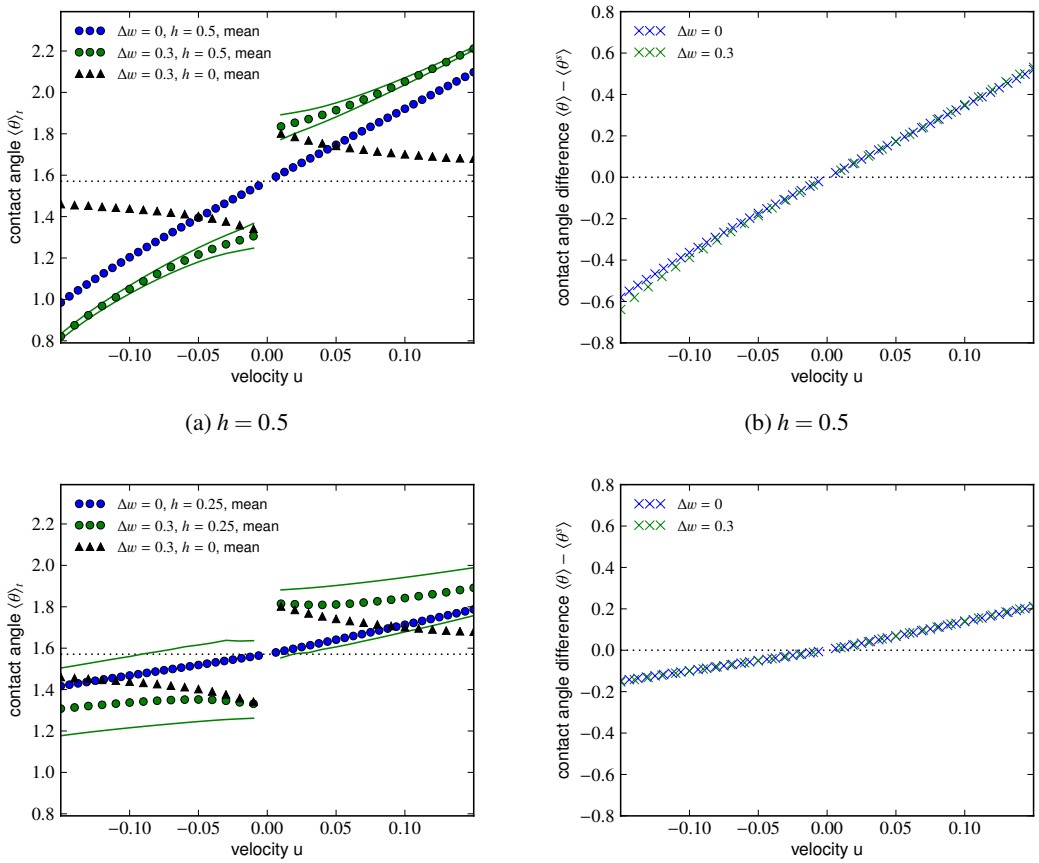

(a) $h = 0.5$ (b) $h = 0.5$

(c) $h = 0.25$ (d) $h = 0.25$

Fig. 4.6: (a) Time averaged microscopic and macroscopic contact angle for homogeneous and heterogeneous case with $\Delta w = 0.3$, $k = 5$ showing the more uniform sampling of the substrate wetting energy with increasing velocity (b) Difference between microscopic and macroscopic contact angle for homogeneous and heterogeneous case for $\Delta w = 0.3$, $k = 5$ showing that for moderate velocities the hydrodynamic contribution to the dynamical contact angle does not vary strongly between the homogeneous and the heterogeneous case (c) time averaged microscopic and macroscopic contact angle at $h = 0.25$ (d) corresponding difference at $h = 0.25$. In all cases: $w_0 = 0$.

The difference between the microscopic and the macroscopic contact angle is approximately the same in the homogeneous and heterogeneous case, as shown in Fig. 4.6(b). The contribution of the bulk fluid dynamics in the heterogeneous case seems to be quite similar

to the ideal, homogeneous case, only with a changed effective microscopic contact angle. It starts to deviate at higher velocities around $Ca > 0.1$.

Having this substrate dependent contribution to the dynamic contact angle indicates that it is possible to introduce the velocity dependent time averaged microscopic contact angle as effective microscopic contact angle in the model for the motion of a contact line on a homogeneous substrate, like Cox-Voinov. This simplification is expected to capture the fundamental physics associated with the contact line dynamics on a substrate with varying wetting energy. The approximation should especially hold for the case of a clearer separation between the fluctuation and the observation length scale, as the fluid follows the scaling laws obtained for an interface moving on a homogeneous substrate in this range. The heterogeneities are then represented through the effective microscopic contact angle introduced at the lower cutoff. This observation also holds at lower distance $h = 0.25$ to the contact line, as shown in Fig. 4.6(c) and 4.6(d).

To get a better understanding for the mechanism underlying the non-uniform sampling of the substrate the dynamics of free interface with a time periodically changing microscopic contact angle is studied in the following section. The observed response of the fluid interface will lead towards a model to predict the velocity-dependent effective microscopic contact angle. The idea is that the system can not distinguish if the wetting energy is determined by the position on the substrate over time or by varying the contact angle with time directly, as for example in an electrowetting setup[47]. In both cases, a change in the microscopic contact angle at the contact line leads to a displacement of the fluid interface. The local response of the fluid interface to a variation of the microscopic contact angle apparently influences the observations on the macroscopic scale, even beyond the range where the fluctuations of the interface due to the heterogeneities are visible. Therefore, characterizing the response of a contact line to a time periodic driving leads for a better understanding of the dynamics observed for a fluid interface driven over a heterogeneous substrate.

Before this line of thought is pursued, another important measure in the study of contact line dynamics should be addressed: As presented in the theory section when discussing the de Gennes argument for dynamic contact angles, the dissipated energy in the system is directly related to the observed dynamic contact angle. Therefore, the next section shows the change in the dissipated energy when introducing a heterogeneous wetting energy.

4.1.4 Dissipated energy in the system

For the Steady Stokes equation, the energy dissipation is equal to the work done on the system by acting on the domain boundaries since there are no internal degrees of freedom, as inertia, in the bulk of the fluid that can store energy. Due to this, the dissipation rate P_{diss} in the volume V can be expressed by a line integral over the domain boundary D of the droplet in the following form[55]:

$$P_{\text{diss}} = -2\eta \int_V \sigma^*_{ik} \sigma_{ik} dV = \int_D u^*_i f_i dS$$

with η as the viscosity, σ as the stress tensor in the fluid, u as the velocity on the fluid boundary and f as the projection of the stress tensor on the boundary normal, as previously introduced. The variables i and k are indices to be summed up according to the Einstein summation convention. The droplet considered here is bounded by solid interfaces at the top

and the bottom, with free fluid interfaces at the sides. The dissipated energy is the difference between the energy introduced in the system when pulling the droplet over the substrate with Navier slip condition and the energy that is stored by deformation the free interfaces.

It is possible to obtain the energy input into the system over time by measuring the shear stress at the solid interfaces over one period. While energy can be stored in deformations of the free interface, in the case of a periodic motion the total energy in the system after one period has to be the same, i.e. the free interface must have returned to its initial condition. Therefore, any energy that went into the interface deformation was subsequently released and dissipated in the bulk.

The analysis can be extended by separately measuring the work done on the free interface, P_{free}. This way, the energy stored and released by the free interface over time can be characterized and compared to the work injected at the solid boundaries P_{sub}.

$$P_{\text{sub}} = \int_{D_{subs}} u_i^* f_i dS = -2\eta \int_V \sigma_{ik}^* \sigma_{ik} dV - \int_{D_{free}} u_i^* f_i dS = P_{\text{diss}} - P_{free}$$

For the homogeneous substrate, only the bottom substrate contributes to the line integral, as no work is done on the free interface. At the top substrate, the no-slip condition is enforced, setting the local velocity to zero in the co-moving frame. On the free interfaces, the tangential component of the projected stress tensor and the normal fluid velocity vanish, resulting in zero contribution.

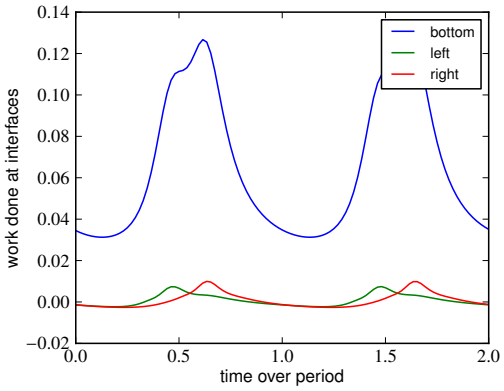

Fig. 4.7: Work performed on the different interfaces of the system over two periods. Energy goes into the deformation of the free interface, until it gets released at the depinning event, characterized by the spike, for u $= 0.11$, $k = 10$, $\Delta w = 0.2$, $w_0 = 0$.

On the substrate with a periodic variation of the wetting energy, the free interfaces are deformed periodically, leading to a variation of the energy input, as displayed in Fig. 4.7. Over the bigger part of the period energy is absorbed by the free interface as it is stretched until it is released when the depinning event occurs. This release of stored energy creates the spike in the contribution of the free interfaces. The work done on the system decreases slightly when the depinning event occurs, but the sum of the components, i.e. the total dissipation in the system, is significantly increased at the depinning event.

The depinning events at the front and the back contact line are not exactly synchronized as the baselength of a moving droplet does not exactly match the equilibrium baselength. This

leads to the shift in the depinning of the front and the back contact line.

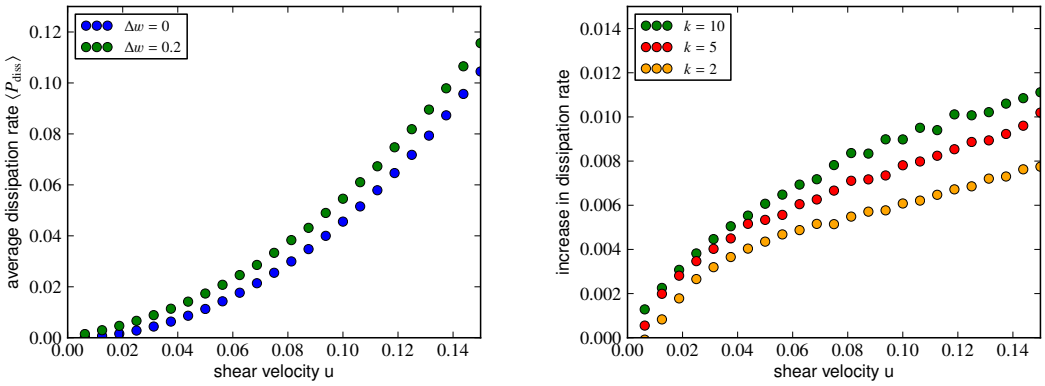

(a) (b)

Fig. 4.8: (a) Dissipation rate for the system driven over a homogeneous (blue) or heterogeneous (green) substrate with $k = 10$, $\Delta w = 0.2$, $w_0 = 0$ showing the increase associated with the period deformation of the free interface (b) Difference in dissipation between the heterogeneous and the homogeneous system for different periodicities k of the substrate

Fig. 4.8(a) shows the dissipation rate over the shear velocity both for a homogeneous and a chemically heterogeneous (green) substrate. The observed dissipation rate in the heterogeneous case is consistently higher than in the homogeneous case, which agrees with the argument of de Gennes that an increased dissipation leads to an increased dynamic contact angle[29]. The difference in dissipation for different periodicities is shown in Fig. 4.8(b). It is increasing with the driving velocity and systematically higher for the case of higher periodicities. But in all cases, the difference between the dissipation compared to the homogeneous substrates continuously approach zero for increasingly small driving velocities. As the contact angle hysteresis is also observed in the limit of small velocities, attempting to rely solely on a dissipation argument without taking into account the varying microscopic contact angle is insufficient. While the dissipation still contributes to the observed dynamic contact angle, it is not useful to predict the static contact angle hysteresis observed in the system.

While it is interesting to understand this change in the dissipation in the system on a heterogeneous substrate, it can not be directly mapped to the dynamic contact angle observed in the system. When attempting to follow the argument of de Gennes, the dissipated energy makes it possible to determine the uncompensated Young force which leads to a deviation from the microscopic equilibrium contact angle θ_0. At this point, it is not clear what is the value of the effective microscopic equilibrium contact angle in case of a heterogeneous substrate. To get a better understanding for the effect of the heterogeneity it is helpful to observe the motion of the contact line over the substrate directly.

4.2 Driven oscillations on a free interface

Given the observation that the response of the contact line is strongly velocity dependent, it is more instructive to study a system where it is possible to separate the effect of the varying

contact angle from the velocity-dependent effect of the bulk fluid dynamics. This is done in this section by studying the response of a resting free interface when varying the substrate contact angle with time. Independent of the chosen oscillation frequency, the solution will be a perturbation of a straight interface, not an interface with a shape that changes with the driving velocity.

In this system, the response of a fluid interface to driving with different frequencies and the dependence on the slip length can be characterized. One point from the previous chapter that can be addressed that way is the varying penetration depth of the fluctuations observed for different driving velocities.

4.2.1 Simulation results from thin film model

The response of a free interface to a periodic variation was studied in the thin film limit, with a droplet resting on a topographically flat substrate. The microscopic contact angle was varied periodically with a wetting energy of the form

$$w(t) = w_0 + \Delta w \cos(2\pi\omega t)$$

with w_0 as the average wetting energy, set to $w_0 = -1/\sqrt{2}$ unless mentioned otherwise, Δw as the oscillation amplitude and ω as the employed driving frequency. The change of the interface slope over the distance from the contact line was measured. Varying the contact angle on both contact lines symmetrically drives a bulk deformation of the droplet away from the contact line due to volume conservation. To be able to study the decay of the fluctuations caused by the periodic perturbation of the contact angle, the left and the right contact angle were varied anti-symmetrically. In linear approximation, the fluid flow induced by the displacement of the fluid interface when decreasing the contact angle on one side is compensated by the flow due to the increasing contact angle on the other contact line. To provide the connection to the previous section: The frequency of the periodic motion ω for a contact line that is pulled with velocity u over a substrate with periodicity k is given by $\omega = ku$.

Fig. 4.9(a) and 4.9(b) show the observed variation in the interface slope over the interface height for different driving frequencies and slip lengths. With increasing distance from the contact line, the oscillations decay due to the finite propagation speed of perturbations of the free interface.

The two characteristic length scales in the context of contact line dynamics are the slip length l_s and the penetration depth of the fluctuation, given by $l_{\mathrm{osc}} = \frac{u_{Ca}}{\omega}$ the driving frequency ω and the capillary velocity. A reasonably good collapse can be obtained with the scaling factor $\sqrt{\omega/l_s}$. The amplitudes of the contact angle oscillations were small enough to keep the response of the fluid interface in the linear limit, i.e. the displacement amplitudes for systems with different levels of contact angle variations $\Delta w < 0.1$ were collapsing well when rescaled with the strength of the heterogeneity.

As the results shown here for the slope $h_0' = 1$ were obtained in the lubrication approximation, they can be rescaled to give predictions for different contact angles. To study higher contact angles beyond the thin film equation, this system with time periodic variations of the contact angle is studied using the full Stokes simulations in the next subsection.

4.2.2 Simulation results from BEM model

In the geometry with the droplet pinned at the top substrate that was introduced previously, the contact angle at the bottom substrate is varied periodically. The phase between the two

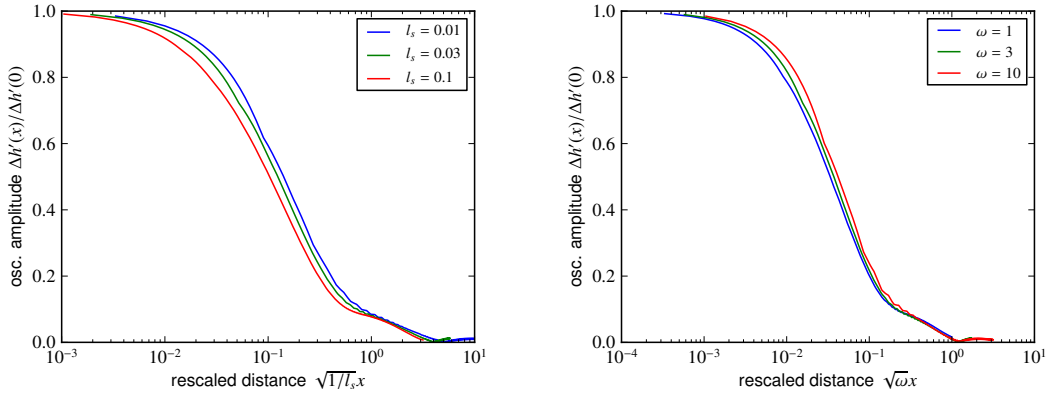

(a) $\omega = 3$ (b) $l_s = 0.03$

Fig. 4.9: For simulations in lubrication approximation: (a) Slip dependence of the slope oscillations of a periodically driven free interface for driving frequency $\omega = 3$ rescaled with $(1/l_s)^{-1/2}$ to collapse. (b) Frequency dependence of the slope oscillations of a periodically driven free interface at $l_s = 0.03$ showing a good collapse with $\omega^{1/2}$. For both graphs: $w_0 = -1/\sqrt{2}$

contact lines is shifted by half a period to reduce the macroscopic deformation mode, as the volume change is compensated in linear approximation. The displacement and deformation of the contact line changes with the driving frequency, as shown in Fig. 4.10. The figure shows the displacement of the free interface over the channel height for three different values of the driving frequency. As the driving frequency is increased, the oscillation amplitude decreases and the displacement is localized closer to the contact line.

From these simulations, the local slope of the interface was determined over the distance from the substrate and over one period of oscillation. Based on this data, Fig. 4.11(a) shows the observed fluctuation of the slope of the free interface over the distance from the contact line for different slip length and driving frequencies. The substrate contact angle was 90° in these simulations, i.e. it was a straight vertical fluid interface in the equilibrium configuration.

The rescaling obtained from the thin film limit works reasonably well and, as previously, the oscillations are nearly dampened out when the characteristic length scale is reached. The plotted amplitude is rescaled with the amplitude of the contact angle oscillation, $\Delta w = 0.2$.

While the amplitude of the contact angle oscillations is enforced through the boundary condition, the displacement of the contact line depends both on slip length and driving frequency. This dependence determines how strongly the contact line position can be displaced over one period of substrate sampling.

Fig. 4.11(b) shows the observed oscillation amplitude of the contact line position over the driving frequency for different slip lengths. As expected, the displacement is decreased with increasing oscillation frequency and decreasing slip length and goes linear with the amplitude of the contact angle variation Δw. With increasing driving frequency, the contact line has less time to be displaced and with decreasing slip length the displacement time scale increases, respectively.

Assuming that the system is still operating in the linear limit, the obtained relationship between the time dependent contact angle and the time dependent displacement makes it

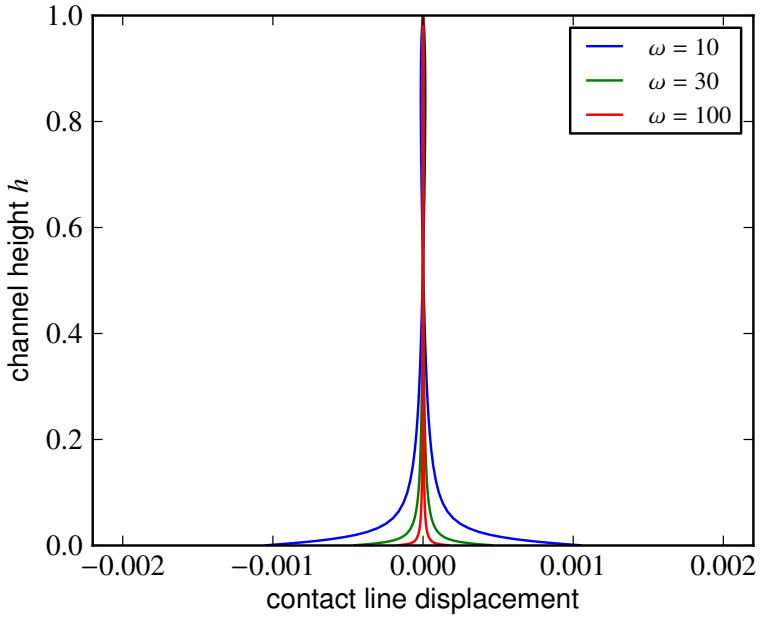

Fig. 4.10: Minimum and maximum of the free interface position for one period with the channel height for $l_s = 0.03$, $w_0 = 0$, $\Delta w = 0.1$ and varying frequency. Increasing the frequency leads to a reduced displacement and stronger localization at the contact line.

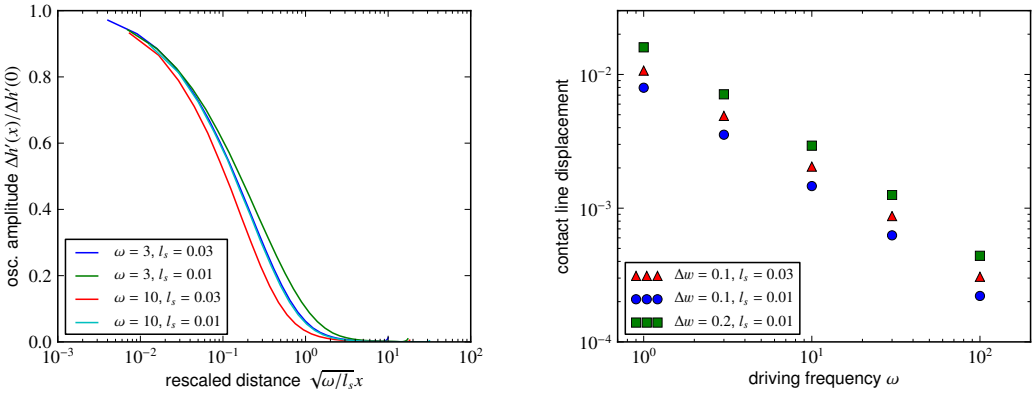

(a) (b)

Fig. 4.11: Results from BEM simulations: (a) Oscillation of the slope of the interface over distance from the contact line for different driving frequencies and slip lengths, showing that the rescaling from the thin film results also works for higher contact angles (b) Amplitude of the oscillation for different driving frequencies, slip lengths showing the decrease of the displacement with slip length, amplitude and driving frequency. For both graphs: $w_0 = 0$

possible to construct a mode coupling model for the velocity dependent contact line dynamics

on a heterogeneous substrate. The idea is to represent the contact line motion over one period as superposition of time periodic contact line displacement modes. For this, the coefficients relating the contact angle signal and contact line displacement have to be obtained first. This is done in the following section.

4.3 Linear response of the interface

The response of the contact line to the driving can be characterized by two terms in first order: The amplitude ratio between the contact line displacement and contact angle signal plus the phase shift between them. The problem was approached in collaboration with M. Brinkmann.

First, the periodic variation of the contact angle at the contact line can be treated in the limit of small perturbations with a linearized thin film equation. Assuming small deviations from the wedge solution $h_0(x) = x$ in the form $h(x,t) = h_0(x) + \varepsilon\delta h(x,t)$ and truncating after terms in $O(\varepsilon)$, it takes the form

$$\partial_x((x^3/3 + x^2 l_s)\partial_x^3 \delta h(x,t) = \partial_t \delta h(x,t).$$

With the separation ansatz $\delta h(x,t) = a_\omega(x)\exp(i2\pi\omega t)$, assuming a time periodic solution with frequency ω, and allowing for complex a_ω, this problem can now be solved numerically. The goal is to find solutions that have a time dependent microscopic contact angle $\theta(t) = \Delta\theta\exp(i2\pi\omega t)$.

The coefficient a_ω can now be split into two components: The ratio $\delta h/\delta\theta = |a_\omega|$ representing the contact line displacement for a given contact angle oscillation is given by $\xi(l_s,\omega)$. The phase shift, between the contact angle signal and the displacement of the contact line is given by $\phi(l_s,\omega)$.

Three major regimes could be distinguished, depending on the characteristic length scale associated with the driving frequency. The characteristic length scale l_{osc} is given by the capillary velocity u_{ca}, which is unity in our case due to non-dimensionalization, and the driving frequency ω, giving an approximation how far the oscillations will penetrate along the free interface:

$$l_{\mathrm{osc}} = \frac{u_{\mathrm{ca}}}{\omega}$$

In the quasi-static limit, where $\omega \to 0$ and l_{osc} approaches the system size, the displacement becomes independent of the driving frequency in first approximation. In this limit the system is locked to the contact angle signal. Therefore the phase shift vanishes, too. This means:

$$\xi \propto \mathrm{const}$$

$$\phi \approx 0$$

The other extreme is characterized by very fast oscillations where the decay length l_{osc} is in the range or below the slip length, giving rise to the scaling

$$\xi \propto \sqrt{\frac{l_s}{\omega}}$$

$$\phi \approx -\frac{\pi}{4}$$

with the contact line displacement trailing the contact angle driving signal. This is the regime observed in the previously presented simulations. In the intermediate regime, where

the characteristic length scale is above the slip length but below the system size, for the amplitude signal, a transition region is observed. The amplitude decreases faster than the square root scaling, but the separation of the length scales in the simulations is insufficient to make a definitive statement. From the characteristic length scale introduced previously, a scaling along the lines of $\xi(\omega) \propto \omega^{-1}$ can be expected.

The dependence of the phase shift is more complicated in this range, as visible in Fig. 4.13(b), where the phase shift displays a local minimum that depends on the slip length. It can still be approximated reasonably well with $\phi(l_s, \omega) = -\pi/4$.

This is the regime especially relevant for experimental systems, where the separation of scales between slip length and system size is given more clearly. Most oscillations that can be observed in such a system should have a decay length between those two length scales.

It is also possible to obtain these coefficients from solving the thin film equation in the described geometry directly, as shown in Fig. 4.12(a). It shows the amplitude coefficients approaching a constant value and the phase shift going to zero (or, in the plotted case, 2π) as the oscillation frequency goes towards 0, i.e. the quasi-static case (shown in Fig. 4.13(a) and 4.13(b)). The amplitude ratio decays with increasing driving frequency, approaching the $\sqrt{l_s/\omega}$ scaling, as predicted, and the phase shift, after an initial dip, goes to $-\pi/4$ in the limit of characteristic length scales close to or below the slip length.

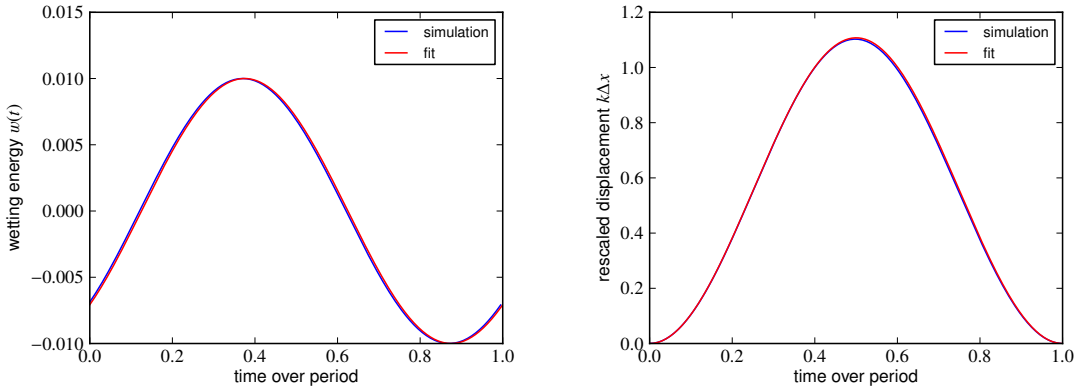

(a) (b)

Fig. 4.12: Simulation results of the thin film wedge driven with $\omega = 5$, $\Delta\omega = 0.01$, $l_s = 0.1$ (blue) and fitted response curve (red) that determined the coefficients of the mode coupling model, with (a) showing the wetting energy and (b) the displacement of the contact line, rescaled with k, over one period of driving. The resulting coefficients for the amplitude ratio and phase shift are plotted in Fig. 4.13(a) and 4.13(b)

4.4 Mode coupling model

From a_ω the ratio between the amplitude of the contact line displacement and contact angle heterogeneity for a given driving frequency and slip length and the phase shift between these two has obtained. With this, a linearised model for the contact line motion over the a heterogeneous substrate can be constructed.

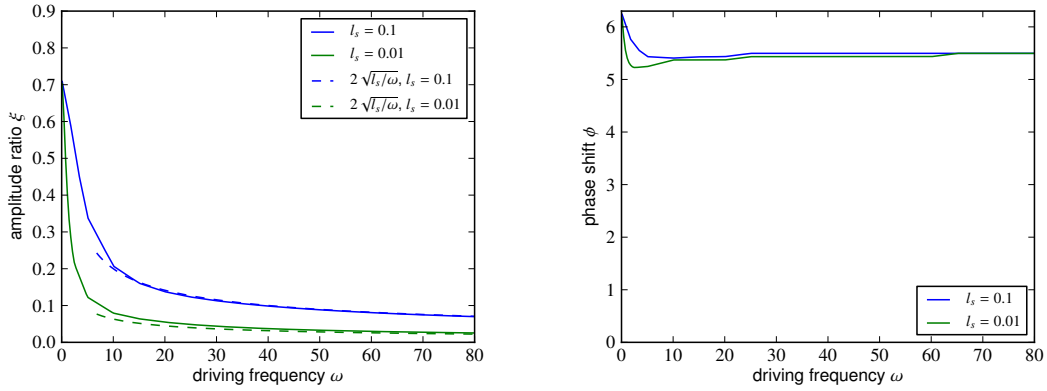

(a) (b)

Fig. 4.13: (a) Amplitude ratio between variation of wetting energy and contact line displacement over driving frequency for different slip lengths showing decreasing displacement of the contact line with increased driving frequency and decreased slip length. For low frequencies, in the quasi-static limit, the displacement approaches a constant value independent of the slip length. For high frequencies, the displacement approaches the $\sqrt{l_s/\omega}$ scaling (dashed lines). (b) Corresponding phase factor approaching 0 for quasi-static driving, as the system follows the contact angle change nearly instantaneously, and $-\pi/4$ for very high frequencies where the characteristic length scale is below the slip length with a transition region in between

The assumption is that one period of the motion of the contact line can be expressed in terms of a mode expansion of the form:

$$x(t) = ut + \sum_n a_n \sin(2\pi nkut) + b_n \cos(2\pi nkut)$$

with t in the interval of one period, given by $[0,(ku)^{-1}]$. The coefficients a_n, b_n are the displacements amplitudes for $n \in [1, N-1]$ for the cases presented here, with $N = 30$ as the number of modes used, unless denoted otherwise. In the same form, the contact angle at the contact line can be expressed as:

$$w(t) = \alpha_0 + \sum_n \alpha_n \sin(2\pi nkut) + \beta_n \cos(2\pi nkut)$$

In this form, each of the modes of the wetting energy corresponds to a time periodic driving of the fluid interface and can thus be related with the displacement of the contact line described by $\xi(l_s,\omega)$ and $\phi(l_s,\omega)$ presented in the last section. The constituting set of linear equations for the mode expansion is

$$\begin{pmatrix} a_n \\ b_n \end{pmatrix} = \xi(l_s,n\omega) \begin{pmatrix} \cos\phi(l_s,n\omega) & \sin\phi(l_s,n\omega) \\ -\sin\phi(l_s,n\omega) & \cos\phi(l_s,n\omega) \end{pmatrix} \begin{pmatrix} \alpha_n \\ \beta_n \end{pmatrix} \tag{4.2}$$

correlating the displacement amplitudes a_n, b_n of the nth mode with the amplitude of the contact angle variation α_n, β_n. The goal is to find a set of displacement amplitudes a_n, b_n such

that the mode expansion of the microscopic contact angle at the contact line over time results in the coefficients α_n, β_n determined by the equation above.

The system under considering has the wetting energy described previously of the shape

$$w(x) = w_0 + \Delta w \cos(2\pi k(x + \mathrm{u}t))$$

over which a contact line is pulled with driving velocity u. The periodic motion of the contact line over the heterogeneity now has a base frequency $\omega_0 = k\mathrm{u}$. The modes from which the solution will be constructed now have the frequencies $\omega = n\omega_0$ with $n \in \mathbb{N}$.

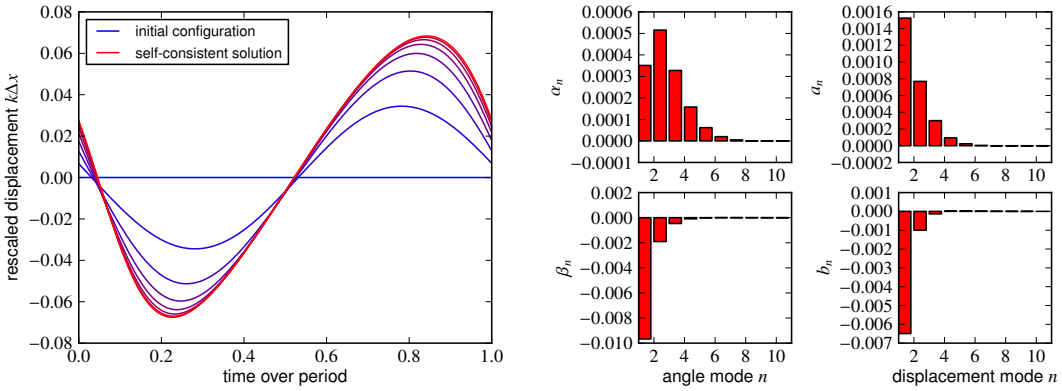

(a) (b)

Fig. 4.14: a) Convergence of the trajectories for $k = 10$, u=-0.01, $\Delta w = 0.01$ from initial configuration assuming a constant contact line velocity (blue) to the final, self-consistent state where the contact angle at the contact line position over time as input in the mode coupling model returns the contact line displacement (red). b) first 10 amplitudes of the mode decomposition of the contact angle (left) and displacement (right) of the self-consistent solution (red).

To obtain the self-consistent solution, a contact line that moves over the substrate with a constant velocity was assumed as initial configuration, i.e. $a_n = 0$ and $b_n = 0$. This gives a microscopic contact angle at the contact line position over time that can be expanded in Fourier modes, giving an initial set of α_n, β_n. Using the displacement associated with these coefficients, the microscopic contact angle over time for this updated trajectory is determined. This process is repeated until convergence is achieved, i.e. the displacement over time corresponding to the set of modes agrees with the microscopic contact angle at the contact line for the given trajectory in space.

Depending on the studied scenario, it is now possible to use either the obtained scalings or the numerically obtained coefficients directly to find self-consistent solutions to the pulled contact line problem. The idea is to start with a contact line moving over the heterogeneous substrate with constant speed, evaluate the contact angle at the contact line over time and use mode coupling equation 4.2 to update the displacement of the contact line over time. After repeating this, the system approaches a state where the contact line displacement agrees with the displacement that would be expected when driving the system with the contact angle signal corresponding to this trajectory.

The process of iteratively approaching the solution is illustrated in Fig. 4.14(a). Here, the amplitude ratio and the phase ratio obtained from the numerical simulations were employed in the model. It shows the trajectories over time for the different iterations, starting with the initial configuration, the blue line and ending with the red line, where the system converged. Fig. 4.14(b) shows the amplitudes of the modes corresponding to the solution plotted in red. The base mode corresponding to the periodicity of the substrate heterogeneity dominates the dynamics, with five more modes having a non-negligible contribution. Their contribution increases for smaller driving velocities, as the displacement becomes more non-sinusoidal.

Now it is possible to obtain the contact angle and velocity signal over time, as previously presented for the full dynamical simulations. Fig. 4.15(a) shows the obtained microscopic contact angle over time for solutions with different driving velocity. It shows the same deviation away from the sinusoidal pattern of the substrate wetting energy with decreasing velocity that could be observed in the full dynamical simulations.

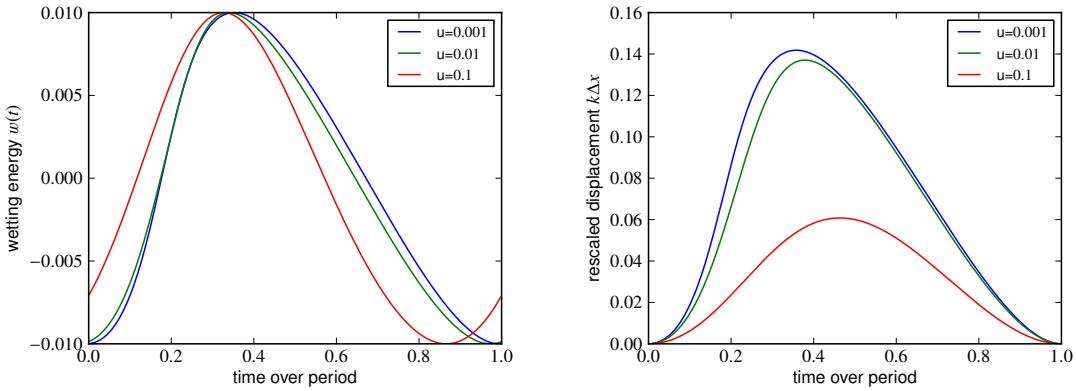

(a) (b)

Fig. 4.15: Mode coupling model: (a) Local contact angle deviation over time for different driving velocities u showing the increasingly sinusoidal profile over time with increasing driving velocity, $k = 10$, $\Delta w = 0.01$ (b) Rescaled contact line displacement over the period showing the stick slip motion and the decreased oscillation amplitude with increasing velocity

Fig. 4.15(b) shows the corresponding contact line displacements with the transition from a significant stick-slip motion to a more sinusoidal perturbation of the contact line velocity, as the higher modes are suppressed with increasing velocity. For sufficiently high driving velocities, the contact line is moving with nearly constant speed, the contact line displacement goes towards zero, and the spatial average of the substrate wetting energy approaches the time average.

Here it becomes clear at which point the model breaks down. The maximum steepness of the slipping motion is limited due to the mode expansion. So when representing a trajectory that is getting increasingly close to a discontinuity it fails to converge. For this, a representation in real space with a time dependent kernel instead of Fourier space could be more successful.

Already earlier, convergence issues will be encountered due to overshooting and subsequent numerical instability if the updated displacements are chosen directly from eqn. 4.2.

By using the average of the old and new displacement coefficients as update step, the stability of the convergence is improved significantly. The corresponding slowdown of convergence is, compared to the numerical cost of running full dynamical simulations, negligible.

4.4.1 Scalings from the mode coupling model

These results can now be evaluated to obtain the time averaged microscopic contact angle for different velocities and slip lengths over a wide parameter range. The obtained deviations from the equilibrium contact angle are presented in Fig. 4.16(a). As the driving speed increases, the frequency of the perturbation increases, leading to a stronger localization and thus reduced deviation. One point that was observed in some of the full simulation runs, but not understood, was an apparent dip of the wetting deviation for small k and low velocities u. This effect appeared also here in the mode coupling model.

The corresponding displacement variation is plotted in Fig. 4.16(b). For high velocities, it decays as the average wetting deviation, but for low velocities it does not decrease, but rather approaches a constant value.

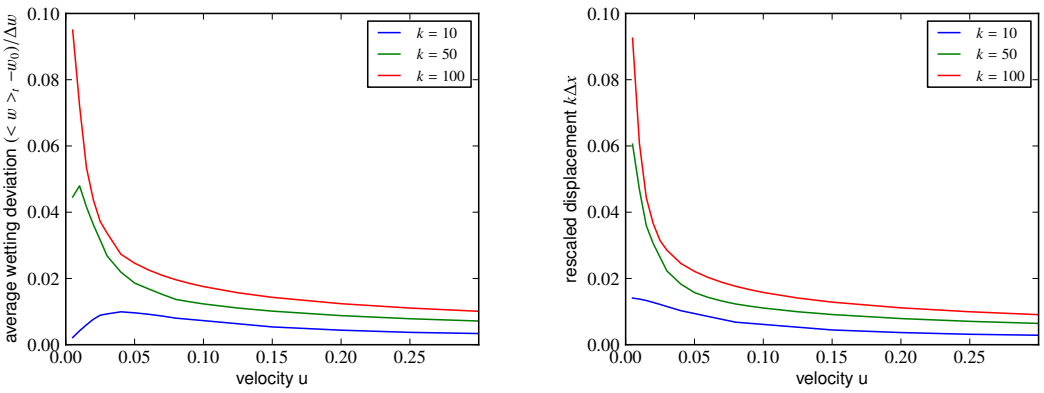

(a) (b)

Fig. 4.16: Mode coupling model: (a) Average contact angle deviation for different driving velocities u and periodicities k for $l_s = 0.1$, $\Delta w = 0.01$ showing the decrease for low velocities in case of small k (b) Corresponding rescaled variation of the contact line displacement that decreases with increasing driving driving force and approaches a constant value for u$\rightarrow 0$

The observations for high velocities can be explained by comparison to the amplitude ratio ξ. As the phase shift approaches a constant value and the system is dominated by the lowest-frequency mode $\omega_0 = k$u. The rescaled displacement and thus the deviation of the wetting energy is directly determined by the decreasing $\xi(l_s, \omega)$ with increasing velocity.

The low velocity case is more interesting, as it is not intuitively clear which length scale might determine if the system approaches the static advancing and static receding contact angle in the limit u$\rightarrow 0$ or if it decreases again, as for the case $k = 10$ shown here. An indication for the underlying mechanism is given by Fig. 4.16(b), where Δx approaches a constant value for low velocities and low k.

The limit of the amplitude ratio $\xi(\omega = 0)$ determines a maximum displacement distance $l_{\text{disp}} = \xi(\omega = 0)\Delta w$ for a given wetting heterogeneity contrast of the substrate. This length scale is independent of any dynamical properties of the system. If the heterogeneity length scale $l_{\text{het}} = 1/k$ is below l_{disp}, multiple locally stable contact line positions would exist. In this limit, the contact line jumps from pinning site to pinning site in the quasi-static limit.

On the other hand, if $l_{\text{disp}} \ll l_{\text{het}}$, the variation of the contact angle is small in the range of possible displacements of the contact line. Therefore, for low velocities, it will approach the equilibrium value again. Only when the relaxation timescale after depinning approaches the driving frequency of the system, dynamical effects play a role again.

4.4.2 Comparison to thin film simulations

The results obtained from the mode coupling model have to be compared to the results from the dynamical simulations to validate this approach of modeling contact line dynamics. After running the numerical simulations for the fluid wedge pulled over a heterogeneous substrate and obtaining the self-consistent solution from the mode coupling model, the displacement over time and the wetting energy over time can be compared, as done in Fig. 4.17(a) and 4.17(b). It shows how in both cases the contact angle deviates from the sinusoidal pattern due to the nonlinearity of the driving.

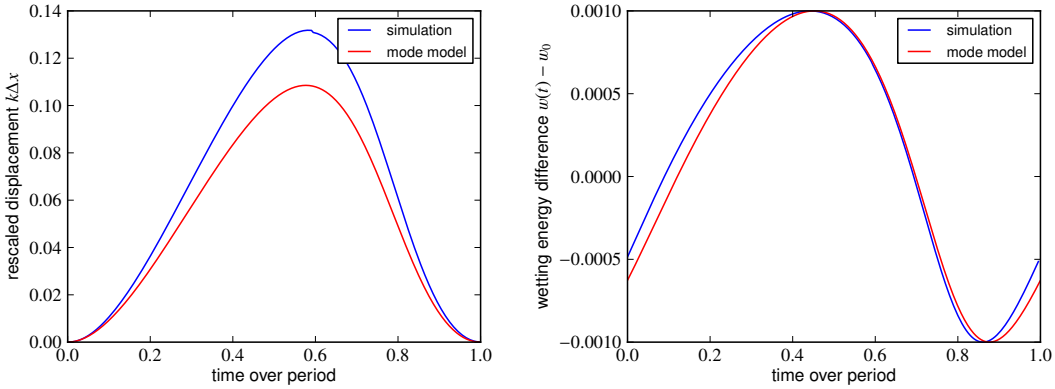

(a) (b)

Fig. 4.17: Comparison of the results for a position dependent wetting energy in a driven system (a) Wetting energy over time for dynamical simulations (blue) with $l_s = 0.1$, $\Delta w = 0.001$, $k = 500$, $u = 0.01$ and mode coupling model (red) (b) Obtained contact line displacement, rescaled with the periodicity from dynamical simulations (blue) and mode coupling model (red) showing reasonable agreement of wetting energy with time, but deviation in displacement

One significant difference can be observed, though: the obtained spatial displacement observed in the simulations is higher than predicted from the mode coupling model. The displacement observed with the position dependent wetting energy is nearly the same as shown for the time periodic driving in Fig. 4.12(b). Up to this point it is not clear if this is an issue with the assumption that a moving, deformed contact line will respond exactly as a stationary contact line to the driving or if it is an issue with non-negligible coupling between the modes.

This question can be resolved by studying a system with the direct numerical simulations that does not have a direct experimental analogy. For a fluid wedge at rest a position and time dependent contact angle is enforced of the same form as introduced in the ode model in eqn. 4.4. This is similar to the case of very small capillary numbers where the hydrodynamic deformation of the interface is negligible. Here, u takes now the role of a driving frequency. If the resulting displacement and time averaged wetting energy agree with the pulled contact line, it is clear that the disagreement is due to an insufficiency of the mode coupling model.

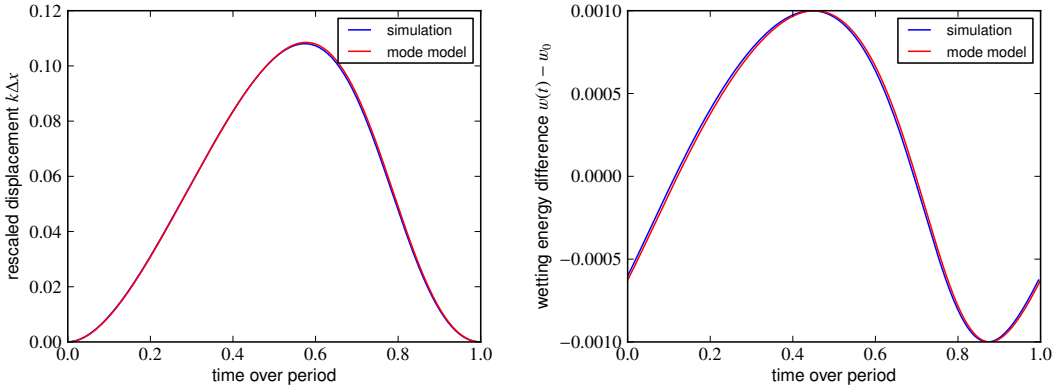

(a) (b)

Fig. 4.18: Equivalent position dependent wetting energy introduced in a system without driving, similar to a very slowly moving contact line (a) Wetting energy over time for dynamical simulations (blue) with $l_s = 0.1$, $\Delta w = 0.001$, $k = 500$, $u = 0.01$ and mode coupling model (red) (b) Obtained contact line displacement, rescaled with the periodicity from dynamical simulations (blue) and mode coupling model (red) showing very good agreement, proving that the model works if hydrodynamic deformation is negligible on the characteristic length scale of the fluctuation

Fig. 4.18(b) and 4.18(a) now show the observed contact line displacement and wetting energy obtained from the direct numerical simulations of the fluid interface (blue) and the mode coupling model (red). They show a very good agreement. That means for very low velocities and low wetting amplitudes, the mode coupling model for the motion of a contact line over a heterogeneous substrate reproduces the results from the direct numerical simulation.

To understand why the pulled contact line did not show such a good agreement as well, it helps to realize that the corresponding driving frequency for the chosen parameters is $\omega = 5$. This corresponds to a propagation length scale of a fifth of the system size, a length scale on which hydrodynamic bending of the interface can not be neglected. Going to lower driving speeds and significantly higher periodicities to obtain a lower penetration depth of the fluctuation while reducing the deformation of the interface was unfortunately not possible. This is due to the numerical costs associated with using a discretization on the length scale of this heterogeneity together with the appropriate time step. The agreement could be improved by obtaining the amplitude ratio and phase shift coefficients by varying the contact angle on a moving contact line over time.

For a more systematic comparison, the time averaged wetting energy and the displacement

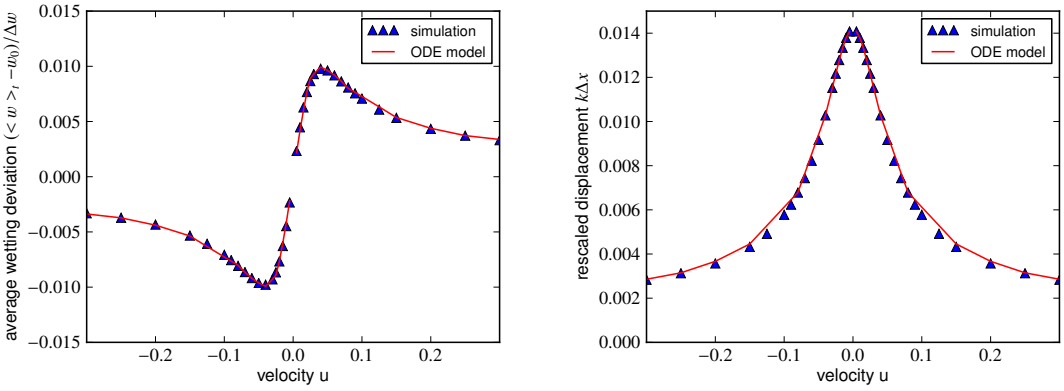

(a) (b)

Fig. 4.19: (a) Time averaged wetting energy for different driving speeds, periodicities of numerical simulations (blue) and mode coupling model (red) showing good agreement, for $l_s = 0.1$, $k = 10$, $\Delta w = 0.001$ (b) Displacement of the contact line over one period for different driving speeds for numerical simulations (blue) and mode coupling model (red) showing a very good agreement of the two models for varying driving velocities

of the contact line can be compared for different driving velocities. The results are presented in Fig. 4.19(a) and 4.19(b). Both measures for the similarity of the solutions obtained from the direct numerical simulations and the mode coupling model agree very well. The graph presented here, for $k = 10$, reproduces the behavior described previously for widely spaced heterogeneities where the residue is around zero for the quasi-static limit, approaches a maximum when the relaxation time scale of the interface and the driving frequency match and decreases again towards zero as the fluid interface can not follow the driving anymore.

At this point, the speed advantage of the mode coupling model should be pointed out again: Instead of requiring the time integration of a set of more than 300 ODEs, using the mode coupling model required less than 100 iterations with 20 modes to obtain the results presented here. This way, the contribution of the heterogeneity to the dynamic contact angle can be predicted significantly faster than by running the full numerical simulation for each velocity. With a thin film code that resolves the full three-dimensional problem with contact angles varying in z-direction, it should be possible to generalize this approach by introducing an extra parameter k_z that characterizes the variation of the contact line displacement along the fluid interface.

4.4.3 Results on random substrates

This mode coupling model not only makes it possible to study sinusoidal variations of the wetting energy, but arbitrary periodic structures. To represent random substrates, a wetting energy obtained as sum of sinusoidal contributions with random phase shift was used. It takes the form:

$$w(x) = w_0 + \Delta\theta \sum_{i=1}^{N} \frac{1}{i} \sin(2\pi i k x + \Phi_i)$$

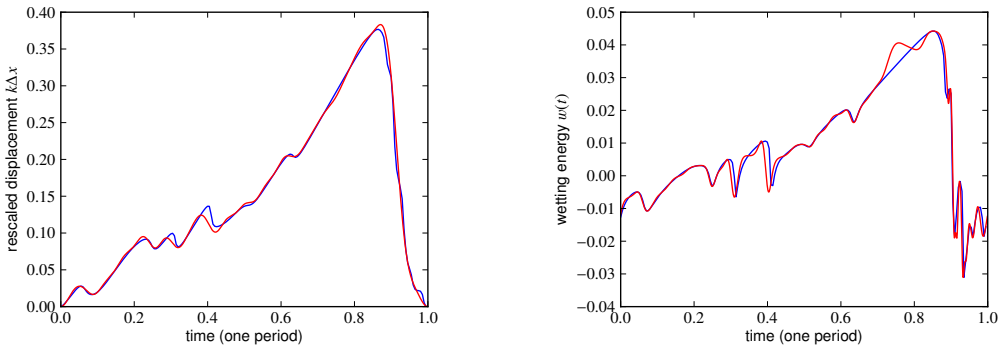

(a) (b)

Fig. 4.20: Random substrates: (a) Wetting energy at the contact line from thin film equation (blue) and mode coupling model (red) on a random substrate $k = 10$, $l_s = 0.1$, $u = 0.01$, $\Delta w = 0.02$ (b) corresponding contact line displacement over time

Using this model with $N = 20$ modes for the wetting energy, trajectories were determined for different realizations of Φ_i. The observed wetting energies and displacements over time for three sample trajectories are depicted in Fig. 4.21(a) and 4.21(b). It is visible that the contact line displacement does follow the wetting energy signal. The displacement curve shows a smoothing of the higher frequency components. This can be expected from the monotonously decreasing amplitude ratio $\xi(\omega)$, which corresponds to a reduced displacement with increasing frequency for a given variation of the wetting energy.

The deviation of the time averaged wetting energy and the displacement of the contact line over one period can now be determined for a high number of realizations, 1000 in the case presented here). Fig. 4.21(c) shows the histogram of the deviation of the time averaged wetting energy. It displays a strong variation with the chosen realization, compared to the average value. The second measure for the effect of the heterogeneity, the contact line displacement distribution, is clustered more strongly, as shown in Fig. 4.21(d).

4.5 Contact line friction model

Following the reasoning behind the effective contact line friction model, the periodic de- and repinning of the contact line can be modeled in the quasi-static limit. There, the interface configuration is static for the given contact line position and the contact line velocity is determined by the stress imbalance between the contact angle and the substrate wetting energy. This reduces the system to a single ordinary differential equation. This model is designed for slow contact line velocities, bulk hydrodynamics is basically completely neglected.

It is very similar to the model described by Joanny and Robbins[38], who made an early attempt to model the dynamics of a contact line moving over a periodically structured plate. While they discussed the effect of the heterogeneous substrate on the mean displacement of the contact line, they did not study the fluctuation of the interface observed over one period.

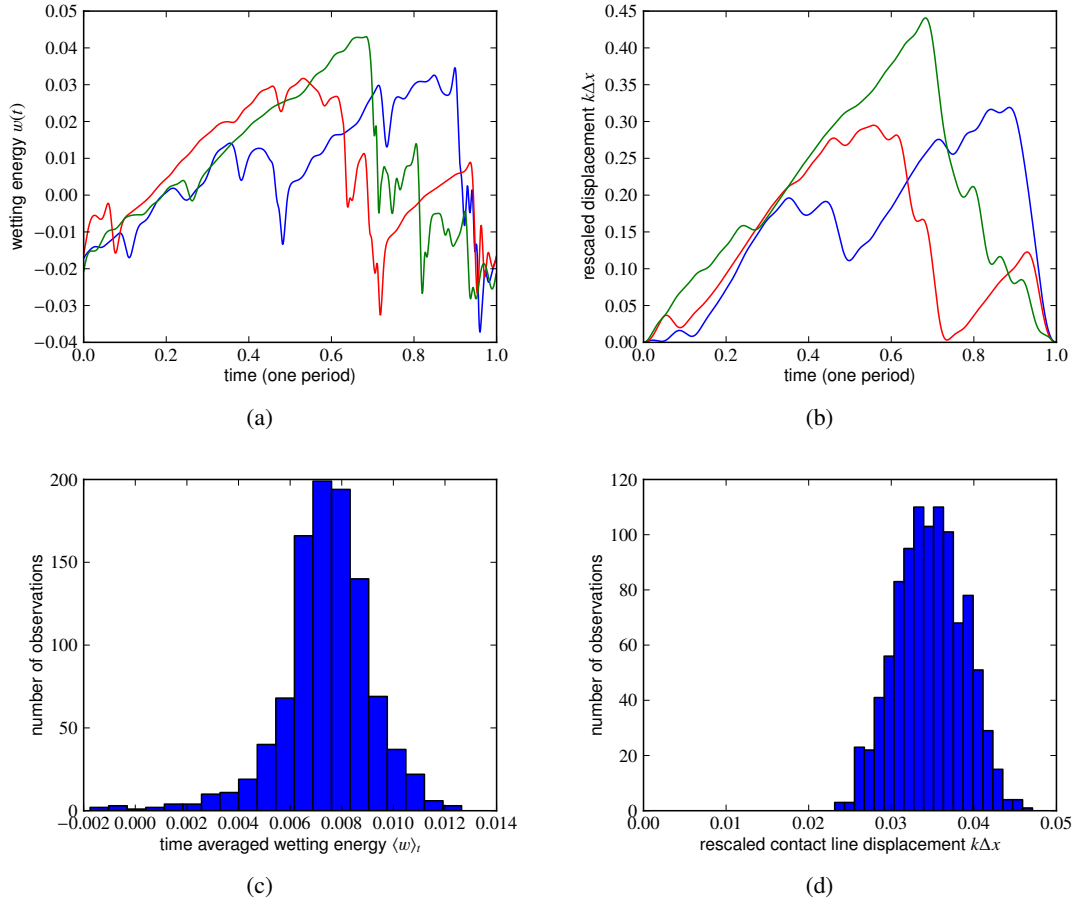

Fig. 4.21: Random substrates: (a) wetting energy at the contact line for three different realizations of a random substrate $k = 10$, $l_s = 0.1$, $u = 0.01$, $\Delta w = 0.02$ (b) corresponding contact line displacement over time (c) distribution of time averaged wetting energies of 1000 realizations for $k = 10$, $l_s = 0.1$, $u = 0.01$, $\Delta w = 0.02$ (d) corresponding distribution of variations in the contact line position over one period

4.5.1 Model ODE

To understand the velocity-dependence, a simplified model can be introduced. In a quasi-static approach the interface is assumed to be always straight and the contact line velocity is given by a simplified linear friction law of the form:

$$x' = a(\cos(\theta) - \cos(\theta_0(x))) \tag{4.3}$$

with θ_0 as the sinusoidally varying position dependent local contact angle, θ as the current contact angle and a as a friction factor. The position dependent local contact angle was chosen as in the previous sections. Assuming a channel geometry where the interface is pinned at unit height, the contact angle can be determined from the contact line displacement.

Integrating this equation with a with a position dependent θ_0 on a moving substrate gives a time dependent contact angle, as in the full dynamics simulations. The crucial difference

is that the height dependence is non-existent in this quasi-static model. Also, the full fluid dynamics and slip issues are reduced to the single coefficient a.

To establish the analogy to the previously introduced model: when expanding the cosine with $\theta = \theta_0 + \Delta\theta$ and linearizing eqn. 4.3, it can be written in the form of eqn. 4.2 with $\xi = a^*(\theta, l_s)/\omega$ and $\phi = -\pi/2$. Especially the discrepancy in the phase shift raises the question which model represents reality better and should be addressed experimentally.

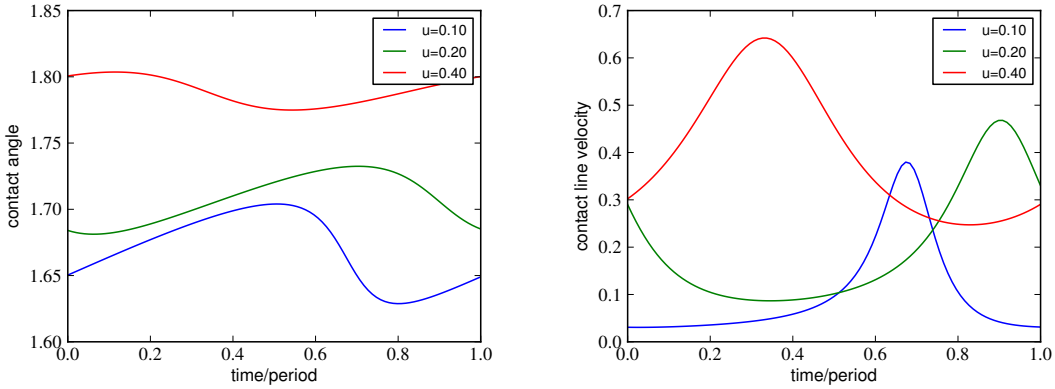

(a) (b)

Fig. 4.22: (a) Contact angle over one period for different driving velocities, $k = 10$, $\Delta w = 0.1$, $a = 1$ (b) Corresponding contact angle over one period for different driving velocities

Fig. 4.22(a) shows the contact angle observed over one period for different driving velocities after the initial relaxation process. As in the full simulations, the fluctuations are decreasing and becoming more sinusoidal as the driving frequency goes above the characteristic relaxation time scale of the system.

The corresponding contact line velocity over the period is plotted in Fig. 4.22(b). It shows the same stick-slip structure observed in the full dynamical simulations that becomes more sinusoidal with increasing velocity.

These results can be evaluated for minimum, maximum and mean contact angle, as done previously. Fig. 4.23 shows these for different driving velocities and both a homogeneous and a heterogeneous substrate. The results show the same characteristic features as the full BEM simulations. For the case with heterogeneity, the observed contact angle is generally increased and with increasing velocity, the fluctuation of the contact angle decreases.

There are a few issues with this model, though. First of all, with only one free parameter a, the two competing effects of the hydrodynamic deformation due to the interface motion and the relaxation dynamics can not be captured. This could be fixed by introducing a cutoff length for this quasi-static model, above which a stationary hydrodynamic profile is assumed. If this cutoff length should be made velocity dependent is not clear and significantly increases the amount of assumptions necessary to improve this model and additional fitting parameters.

The second issue is the disagreement, especially of the phase shift, with the direct numerical simulations for higher velocities. Both models approach a constant phase shift, though. Therefore the difference would be mainly in the ratio of the average contact angle deviation to the amplitude of the contact line displacement. The disagreement in the amplitude ratio coefficient in the intermediate regime is the logarithmic component, which is difficult to discuss

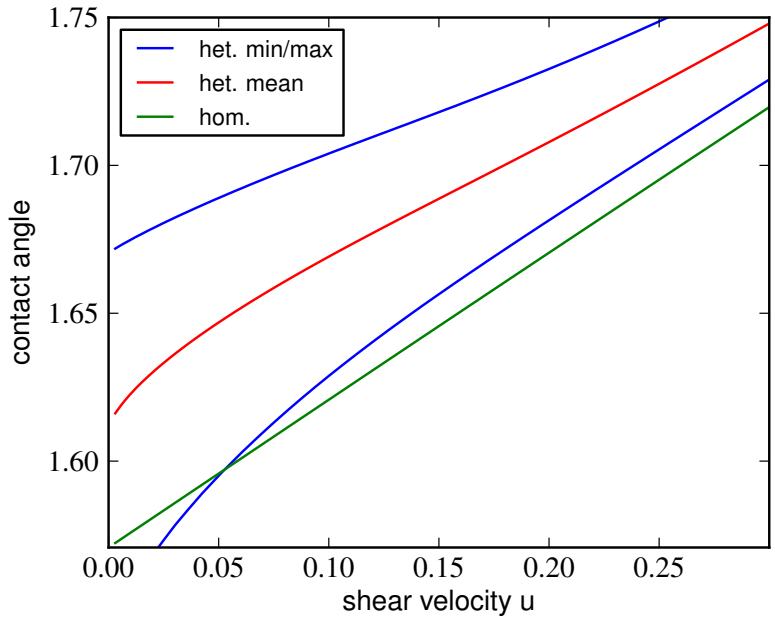

Fig. 4.23: Obtained minimum, maximum and mean contact angle for homogeneous case, heterogeneous case, e=0.1, k=10, a=1, showing the decreasing variation with increasing shear velocity and change in contact angle due to heterogeneity

unless the velocity is varied over multiple orders of magnitude.

4.5.2 Observed scalings

The previous results already showed that the qualitative features of contact angle hysteresis and a slowly decaying deviation from the spatially averaged contact angle are fulfilled. The predictions for the scaling from the mode expansion make it possible to check up to which point, if at all, this model gives similar results concerning the scaling of time averaged contact angle and contact angle fluctuation.

A similar scaling is observed for the difference between the observed time averaged contact angle for the homogeneous and the heterogeneous case, as shown in Fig. 4.24(a). Here, the difference between the homogeneous and heterogeneous slope decays with $1/\omega$. As discussed for the mode coupling model, this is directly connected to the scaling of the amplitude ratio $\xi(\omega)$, as the mode with the frequency $\omega = k$u dominates for higher velocities.

Fig. 4.24(b) shows the slope fluctuation over the driving velocity. It shows the same $1/\omega$ decay as long as the driving velocity is not becoming too small. For slow velocities, the curve bends down, as the maximum slope variation is limited by the substrate wetting energy contrast. At very low velocities, the system follows the substrate contact angle directly, i.e. $\theta = \theta_0$, and this quasi-static model becomes purely static.

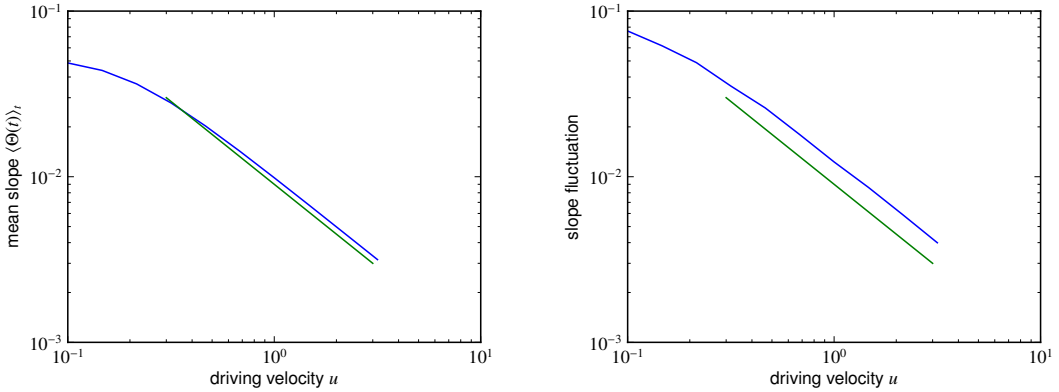

(a) (b)

Fig. 4.24: (a) Decay of the difference between the homogeneous and heterogeneous mean contact angle with increasing driving velocity for $k = 10$, $\Delta w = 0.1$, $a = 0.1$ (b) Corresponding decay of the slope fluctuation with increasing driving velocity

4.6 Summary

In this chapter, the motion of fluid interfaces over substrates with a periodic variation of the wetting energy was studied. The change of the macroscopic contact angle away from the contact line compared to the equivalent homogeneous substrate with the same average wetting energy was presented. For low velocities, a pronounced stick-slip motion was observed, that became increasingly smoothed out with increasing velocity. With increasing velocity, the oscillations of the free interface were shown to be increasingly localized at the contact line.

The first section showed that only considering the static advancing and static receding contact angle is insufficient to describe the dynamics observed on a substrate with spatially varying microscopic contact angle. As alternative, a velocity dependent effective microscopic contact angle based on the sampling of the substrate by the contact line over time was proposed. Together with the deformation due to viscous stresses observed on the homogeneous substrate, it provided a good approximation for the velocity dependent macroscopic contact angle.

To get a better understanding for the oscillations of the free interface due to the heterogeneities, the response of a fluid interface to a periodic variation of the contact angle was studied. An increased localization with increasing driving frequency and decreasing slip length was shown. The localization is characterized both by the distance from the contact line up to which the deformation is observed on the free interface and the displacement of the contact line on the substrate.

Based on the frequency dependent amplitude ratio and phase shift between the contact angle signal and the displacement response, a simplified model to obtain the contact line motion over a heterogeneous substrate is proposed. The model represents the contact angle at the contact line as it moves over a periodically patterned substrate as a superposition of sinusoidal variations of the contact angle. These variations lead to a displacement of the contact line. If the displacement of the contact line over time leads to the contact angle signal that was used to determine the displacement, the problem is solved self-consistently.

In the limit where the motion can be represented by a linear superposition of the perturbations and viscous bending on the length scale where the oscillations occur is negligible, the model reproduced the trajectory obtained from direct numerical simulation of the thin film equation. For higher velocities, the accuracy decreases as the displacement ratio and phase shift change compared to the resting fluid interface. To show a possible application, the trajectories of the contact line on multiple substrates with random substrate wetting energies constructed as a superposition of sinusoidal variations of the wetting energy was determined.

5 Droplet depinning and mobility

This chapter is focused on the problem of the statics and dynamics of droplet depinning and motion in two dimensions. In this limit, the droplet consists of two contact points connected through the bulk interface. It is placed on a topographically flat substrate with a periodic variation in the substrate wetting energy surrounded by an inviscid fluid. In the previous chapter, the system was driven with a constant velocities. In contrast, the droplet in this chapter is driven by a constant volume force parallel to the substrate, as in the case of a droplet sitting on a vertical wall.

For the case of a chemically homogeneous substrate, the droplet would start moving the moment an infinitely small driving force is applied. For a heterogeneous substrate, the energy landscape describing the possible droplet configurations displays energy barriers between the stable solutions. Therefore, a finite driving force is required to overcome the energy barriers and depin the droplet. The goal is to understand how the strength and periodicity of the substrate heterogeneities influence the depinning, mobility and repinning of such a droplet. As the periodicity changes, the system goes from pinning at a single defect to the case where the periodicity is significantly below the droplet size. In this limit, the position dependent, well-defined contact angle approaches the limit of a homogeneous contact angle hysteresis where a range of contact angles is allowed for any position of the contact line on the substrate.

In this chapter the system is non-dimensionalized with the surface tension γ, the viscosity η, density ρ and droplet volume set to unity. With these non-dimensional units, the capillary number Ca corresponds to the non-dimensional velocity u of the droplet. The position of the droplet on the substrate is characterized by the location of the front and the back contact line, x_f and x_b. Alternatively, the contact line position can be represented through the center of the base, $x_c = (x_f + x_b)/2$, and the baselength $l = x_f - x_b$. This parameterization is used for this chapter.

This chapter discusses fundamental questions arising when looking closer into this problem: In the beginning the static solutions of the system for a given heterogeneity and driving force are studied. Depending on the characteristic length scale of the heterogeneity compared to the droplet size and the amplitude, multiple stable droplet solutions can coexist. Starting from this set of multiple local equilibria, they annihilate until one stable equilibrium remains, and finally none, at which point depinning is inevitable.

It continues with a study of the depinning process, showing how the depinning scenario can change when moving beyond the single defect case. It turns out that this strongly depends on the dynamical properties of the system. The depinning scenario changes qualitatively with varying slip length l_s of the substrate while the static wetting properties remain the same.

Having observed this phenomenon, the question arises if it is possible to give a simplified model reproducing this change. One possible approach is to reduce the dimensionality of the system to the contact line positions, as used to obtain the static solutions. With a contact line friction law, as used in the model of contact line driven dynamics, does not capture the change in the bifurcation scenario. Allowing for the ratio of translation and deformation mobility of the droplet to change leads to the transition observed in the full dynamical simulations,

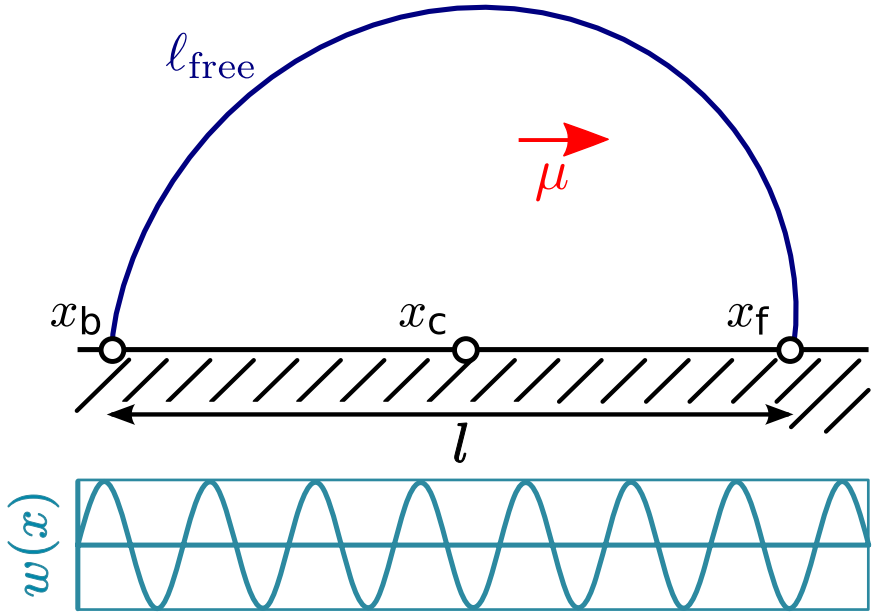

Fig. 5.1: Illustration of the model system, a droplet sitting on a chemically heterogeneous substrate, characterized by the wetting energy $w(x)$, driven by a volume force μ parallel to the wall. The droplet position can either be represented with the contact line positions x_f and x_b or the base-length l and the center-of-base x_c. The length of the free interface is given by ℓ_{free}.

though. The goal is to study this system at different levels of approximation to understand which components of the relevant physics are captured.

5.1 Statics

Before discussing the dynamics of droplet depinning, it is helpful to get an understanding of the statics of pinned droplets on such a heterogeneous substrate. Independent of the chosen model to study the dynamics of moving droplets, the static droplet configurations as energetically extremal configurations of the fluid remain the same[1]. This section shows how the number of possible configurations depends on the chosen strength and period of the heterogeneity. It also shows how the number of static solutions is reduced as the driving force approaches the depinning threshold.

5.1.1 Upper bound for the depinning

The most straightforward system to consider is a droplet pinned by a single point defect on an otherwise homogeneously wetting substrate. An upper limit for the force required to depin a two-dimensional droplet is given by the fact that the equilibrium state has to be stable under variational displacement on the substrate given the assumption that the droplet does not deform. This can be represented by the following equation:

[1] When using the full curvature term. With the thin film approximation of $\kappa = h''$, the static solutions differ.

$$\mu(\Delta x) = (w(x_f) - w(x_b))(\Delta x)$$

The energy gain through the displacement Δx in the gravitational field, μ, has to be compensated by the difference in substrate surface energy between the front and the back contact line, $(w(x_f) - w(x_b))$ if the droplet should stay pinned. This naive model assumes that the shape of the droplet has no influence at all. If the wetting energy depends on the contact line position, this value can be reduced. The correlation of the wetting energy with the contact line positions and therefore the droplet shape plays a crucial role in the wetting on substrates with a position dependent contact angle.

5.1.2 Static drop morphologies on periodic substrates

Another case to study - and the case mainly considered in this chapter - is a substrate where the contact angle varies periodically in space. The substrate wetting energy takes the following form:

$$w(x) = w_0 + \Delta w \sin(2\pi(k/l_0)x)$$

with w_0 as the average wetting energy, Δw as the strength of the heterogeneity and k/l_0 as the rescaled periodicity of the heterogeneity. The length l_0 gives the equilibrium baselength of the droplet for a given w_0. The case $k = 1$ corresponds to a substrate where exactly one period fits below a droplet in the limit of a weak heterogeneity. This means a droplet with different equilibrium contact angle covers the same number of defects for the same wavenumber k.

If the wavelength of the substrate is big compared to the droplet size, the depinning process is similar to the depinning at a single defect. The pinning force is not determined by the minimum and maximum wetting energy, but the maximum wetting energy gradient. It determines the difference between the wetting energy at the front and the back contact line in this case.

The energy of the minimal droplet configuration for a given baselength and center of base without driving force can now be determined as the sum of the contribution from the free interface and the wetted substrate, as presented in section 3.1:

$$E(l, x_c) = \gamma \ell_{\text{free}}(l) + \int_{x_f}^{x_b} w(x)\mathrm{d}x$$

As the characteristic length scale of the heterogeneity goes below the characteristic length scale of the droplet the system goes from the case with only one locally stable solution to the case where multiple local minima can occur in the energy landscape. Fig. 5.3(b) shows an example energy landscape in the baselength-center-of-base space with local minima at three different base lengths. These three different baselengths correspond to solutions covering three different numbers of periods on the substrate. The system is periodic in center-of-base direction with the substrate periodicity.

The extrema in this energy landscape can be tracked through parameter space. Fig. 5.3(a) shows the result of following the solution branches when varying the characteristic length scale of the heterogeneity k, while keeping the amplitude Δw constant. This was done with the numerical continuation code based on Auto07p. The minimum and maximum baselength are determined by the minimum and maximum wetting energy, respectively. As the periodicity is increased, the number of solutions increases. The minimum and maximum baselength of solutions for a given k do not necessarily correspond to the baselengths determined by

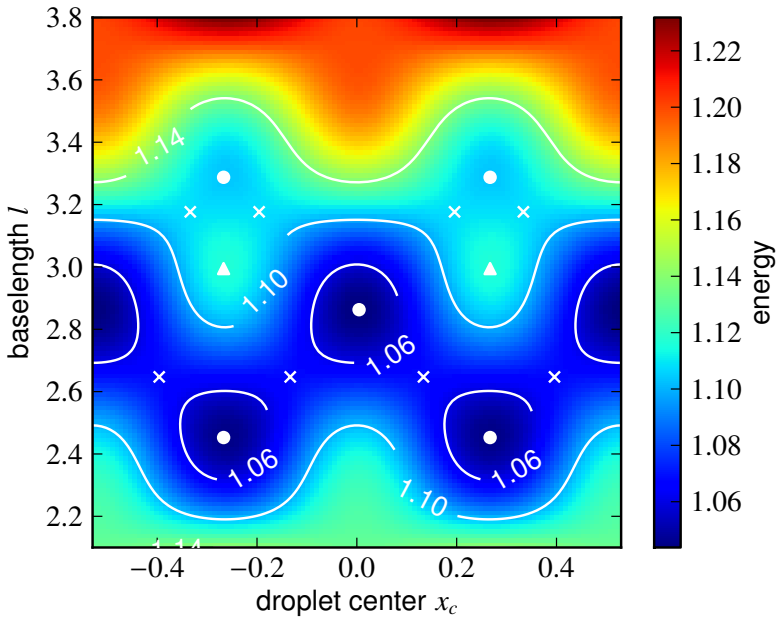

Fig. 5.2: Energy landscape for a heterogeneous substrate in absence of driving force showing the multiple stable droplet solutions with different baselengths, with circles representing local minima, triangles for maxima and crosses for saddle points; $w_0 = -1/\sqrt{2}$, $\Delta w = 0.2$, $k = 5$

the minimum and maximum wetting energy. Only for higher k, as the density of solutions increases, the whole range of possible baselengths is covered.

Two different kinds of solutions can be distinguished: The two solution branches plotted with full lines represent droplets sitting symmetrically on a minimum or a maximum of the energy landscape. The dashed lines represent droplets symmetric to maxima of the wetting energy gradient. The dashed branches are inherently unstable, as these droplet configurations can gain energy by translation on the substrate. The stability of the symmetric solutions varies. This information could not be extracted directly from the Auto07p continuations, but has to be extracted from the corresponding energy landscapes.

In the presence of a volume force, the liquid interface is deformed, changing the baselength-dependent potential of the energy landscape. An extra gradient in center-of-base direction is introduced as the droplet can gain energy by translation. The system is still periodic in center-of-base direction, but with an offset proportional to the driving force, as shown in the energy landscape of Fig. 5.4(a). This graph shows that one pair of solutions already annihilated, compared to Fig. 5.3(b). The other solution branches started to approach each other pairwise, with either a minimum or a maximum and a saddle point coming together.

In a system with constant wetting energy, no more stable solutions exist whenever a driving force is introduced. The situation is different for a heterogeneous system, as the local minima become increasingly shallow with increasing driving and vanish only at a finite driving force.

Fig. 5.4(b) shows the result of following the static solutions from Fig. 5.3(a) at $k = 5$ when varying the driving force. As the driving force is increased, pairs of solution branches approach each other and annihilate, as marked by the red circles. Note the symmetry of the problem, as changing the sign of the driving force has to yield the same result.

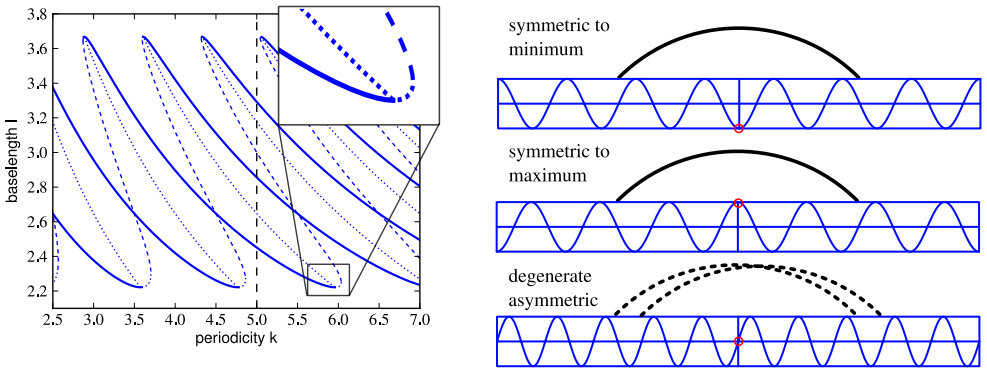

(a) (b)

Fig. 5.3: (a) Stationary solutions for different periodicities of the substrate with $w_0 = -1/\sqrt{2}$, $\Delta w = 0.2$. Full blue lines represent stable droplet states, dashed blue lines twice unstable droplet states and dotted lines represent saddle points in the energy landscape with one stable and one instable direction. With increasing periodicity the number of stable solutions for the given heterogeneity increases. The black line represents the parameter corresponding to the energy landscape on the left side, the inset shows the change in stability at the turning point in detail.
(b) Illustration of the droplet configurations corresponding to the different solution branches. The stable solutions are either symmetric to a minimum or a maximum of the substrate wetting energy.

At certain driving forces, the solutions annihilate pairwise until, no more pinned solutions exist above a critical driving $\mu^{\uparrow}$. For higher driving forces, only moving solutions can exist. Fig. 5.5 shows the driving force, where the last pairs of solutions annihilate, over the strength of the heterogeneity at the top plus the contact angle at the front or the back contact line of that solution below.

The first observation is that the proportionality between the strength of the heterogeneity and the critical driving force, expected from the single defect case, can be broken for the case of small defect strength. This is caused by a comparably strong coupling of the contact line positions through the free interface. While it would be more favorable to bring the contact lines closer to the regions of minimum or maximum wetting energy, the increase in the length of the free interface due to the corresponding change in the droplet baselength prevents it. The strength of this effect depends strongly on the periodicity of the heterogeneity.

The second point is that, with increasing strength of the defects, the pinning scenario can actually change from a system being pinned at the front, where the contact angle at the front of the static droplet corresponds to the maximum substrate contact angle, to a system being pinned at the back. This is illustrated by the two solutions marked by the green and blue circles.

Fig. 5.6 plots the critical driving force where the solution branch annihilates over the periodicity k for the different solution branches. Each branch already annihilates at a very low driving force when it initially appears, reaches a maximum as the number of covered periods that it is associated with approaches the equilibrium baselength of the droplet and

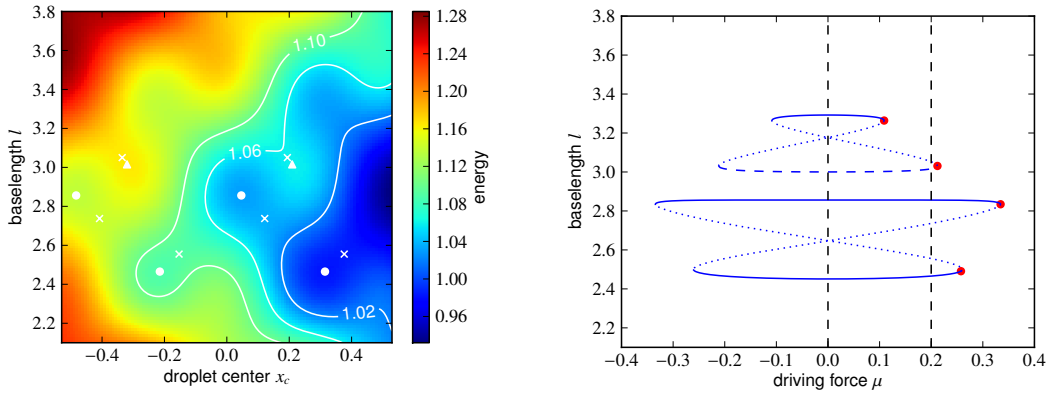

(a) (b)

Fig. 5.4: (a) Energy landscape for a heterogeneous substrate with finite driving force showing the deformation due to the driving term coupling to the droplet center. Due to the heterogeneity pinned solutions still exist, even though the number of stable solutions decreases with increasing μ; $w_0 = -1/\sqrt{2}$, $\Delta w = 0.2$, $k = 5$, $\mu = 0.2$
(b) Baselength l of the solution branches over driving force μ of the system showing the pairwise annihilation of solution branches. The full lines represent minima, the dotted lines saddle points and the dashed line maxima in the energy landscape, the red dots represent the critical driving forces where solution branches annihilate. For driving forces where no more stable solutions exist, only periodically moving solutions remain. Parameters: $w_0 = -1/\sqrt{2}$ (45°), $\Delta w = 0.2$, $k = 5$. The black lines represent the energy landscapes plotted on the left side and in Fig. 5.3(b)

subsequently vanishes again as k increases even further. One can imagine it as the underlying checkerboard pattern of Fig. 5.3(b) being compressed, with the solutions moving towards smaller baselengths as the wavenumber k increases.

Fig. 5.6 also shows how strongly the critical driving force where the last pinned solution disappears can differ from $2\Delta w$, as expected for the case of two independent pinning sites. When the periodicity of the substrate matches, a critical driving force of 0.4 can be observed for a defect strength of 0.2, but it can go down to nearly half of it, if the length scales are mismatched.

In this case, due to the restoring force of the free interface, the two contact lines can not get to the minimal and the maximal wetting energy ares at the same time, reducing the effective pinning strength. With increasing periodicity k, the distance between minima and maxima in the wetting energy is decreased. Therefore, the relative change in the energy of the free interface compared to the change in wetting energy per unit is decreased. This allows for the contact lines to get closer to the minimal/maximal wetting energy configuration and leads to a less pronounced reduction of the critical depinning force.

When comparing this figure to Fig. 5.3(a), it becomes clear how solutions that are initially close to the homogeneous baselength l_0 have the highest depinning force. As the solution branch moves farther away from this case toward a solution with minimum/maximum equi-

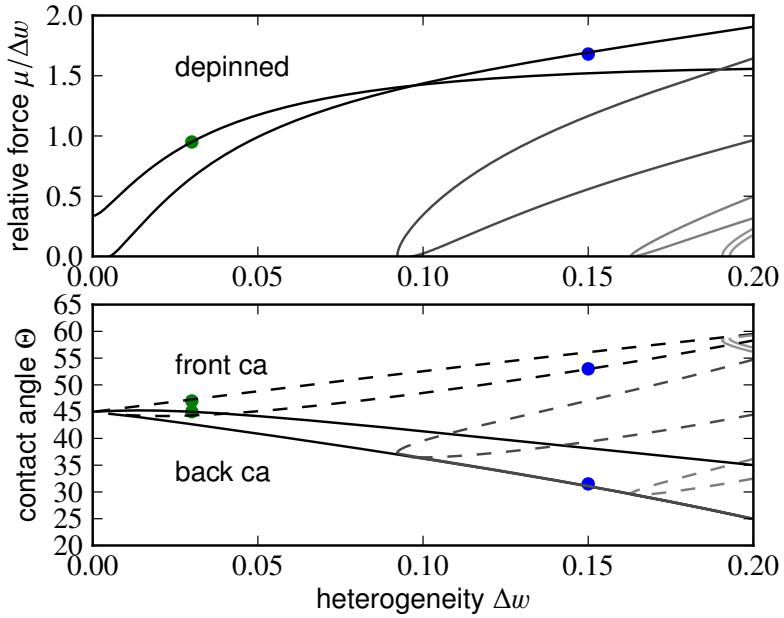

Fig. 5.5: Critical driving force (top) and contact angle at the front and back contact line (bottom) over strength of the heterogeneity. It shows the system changing from pinning at the front contact line to pinning at the back contact line with increasing pinning strength. The dots represent two individual solutions (green and blue) with circles marking the critical force and corresponding front contact angle, and back contact angle at the depinning point $w_0 = -1/\sqrt{2}$, $k = 7.1$. It shows that the depinning force is below the force predicted from single defects and that the periodicity of the substrate does not determine if the droplet will be pinned at the front or the back.

librium baselength, the pinning force decreases. This can be understood as the gradient of the free interface contribution increases for baselength l farther away from l_0, the equilibrium baselength. This contribution to the total configuration energy reduces the depth of the potential well and thus the required driving force for this solution to annihilate.

5.1.3 Scaling of the depinning forces

The case where the equilibrium baselength of the droplet matches the periodicity of the substrate can be treated semi-analytically to give a better understanding of the changed scaling of the driving force. In this case, the integrated substrate wetting energy does not change with translation when assuming a constant baselength. Therefore, depinning is determined in second order by the change of the baselength over one period to accommodate for the local wetting energies.

With the contribution of the free interface replaced by an harmonic approximation around the equilibrium baselength l_0 for the homogeneous substrate (with $\Delta w = 0$), the total energy of the system takes the following form:

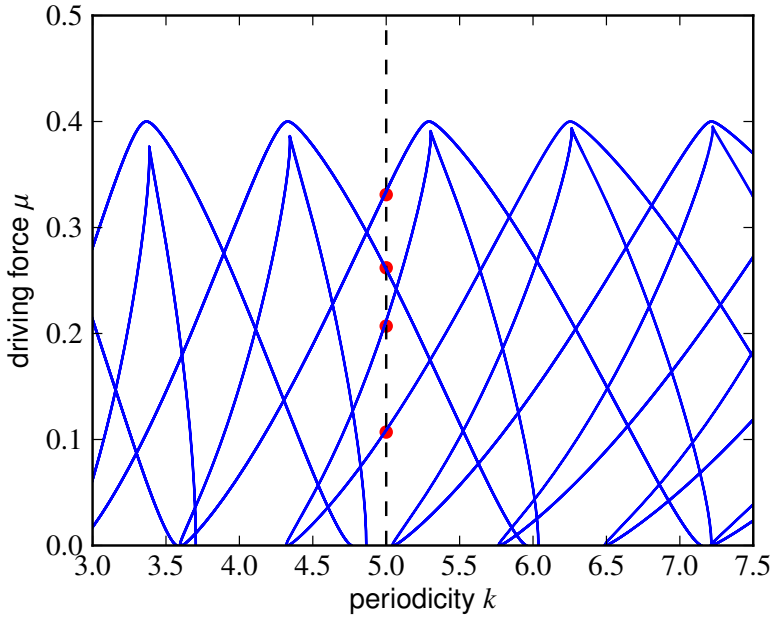

Fig. 5.6: Critical driving force where the different solution branches annihilate over the periodicity of the substrate showing commensurability effects for $\Delta w = 0.2$, $w_0 = -1/\sqrt{2}$. The black line represents the parameters of Fig. 5.4(b), the red points representing the intersections with the blue branches are the turning points marked there.

$$E(l,x_c) = a(l-l_0)^2 - \mu x_c + \Delta w \int_{x_c-l/2}^{x_c+l/2} \cos(2\pi k x) dx$$

Here, l represents the current baselength of the droplet, x_c represents the center of the base of the droplet, μ the driving force and Δw the strength of the heterogeneity. The periodicity is represented as k, as previously, and a is the spring constant of the potential representing the configurational energy of the free interface.

A local minimum exists if both $\frac{dE}{d\,x_c} = 0$ and $\frac{dE}{dl} = 0$ hold for a point (l,x_c). This can also be expressed in terms of the position of the front and the back contact line, $x_b = x_c - l/2$ and $x_f = x_c + l/2$. Then it takes the form:

$$\frac{dE}{d\,x_b} = -\Delta w \cos(2\pi k x_b) - 2a(x_f - x_b - l) - \frac{\mu}{2}$$

$$\frac{dE}{d\,x_f} = \Delta w \cos(2\pi k x_f) + 2a(x_f - x_b - l) - \frac{\mu}{2}$$

In the case of weak coupling, the spring constant a approaches 0. Then the two contact lines, and thus the conditions decouple, i.e. the contact line can take the energetically most favorable position without consideration for the resulting droplet baselength. This leads to the expression:

$$\frac{dE}{d\,x_b} = -\Delta w \cos(2\pi k x_b) - \frac{\mu}{2}$$

$$\frac{dE}{dx_f} = \Delta w \cos(2\pi k x_f) - \frac{\mu}{2}$$

As the cosine can only take values in the range $[-1,1]$, the condition where no more minima exist is given by

$$\mu = 2\Delta w,$$

the same scaling as expected for the case of two independent contact lines.

In the case of strong coupling and a substrate periodicity such that the droplet covers an integer number of periods of the substrate, i.e. $k\,l_0 \in \mathbb{N}$, the contribution of the integral over the equilibrium base length vanishes. The only remaining contribution comes now from the deformation of the droplet from the equilibrium baselength, denoted as $z = (l - l_0)/2$, with changing center-of-base position x_c relative to the substrate.

$$E(\mu = 0) = a(2z)^2 + \int_{x_b - z}^{x_b} \cos(x)dx + \int_{x_f}^{x_f + z} \cos(x)dx$$

The two extremal cases are when both contact lines are now close to the minimum/maximum. Then the cosine is approximately constant, giving us

$$E = a(2z)^2 \pm 2\Delta w z.$$

This energy term has minima at $z = \pm\frac{\Delta w}{4a}$, leading to an energy difference scaling with Δw^2:

$$\Delta E = -\frac{\Delta w^2}{4l_0}$$

This leads to the scaling $g \propto \Delta w^2$, as observed in the numerical simulations for small heterogeneities and substrate wavelengths that are commensurable to the equilibrium baselength of the droplet.

5.1.4 Stability of solution branches

One important bit of information is missing from the analysis up to that point. Stability information can not be obtained directly from the Auto07p model, but only from the energy landscape perspective. The quality of the estimator of the local curvatures on the 2D-array giving the configurational energies is insufficient when the energy landscape becomes flat, close to the point where the solution branches annihilate. To improve the precision compared to numerically estimating derivatives in both dimensions on a 2D landscape, it is instructive to revisit the criteria a local extremum has to satisfy:

$$\frac{\mathrm{d}E_{sub}(x_e, l_e)}{\mathrm{d}x_c} = -\mu$$

$$\frac{\mathrm{d}E_{sub}(x_e, l_e)}{\mathrm{d}l} + \frac{\mathrm{d}E_{free}(x_e, l_e)}{\mathrm{d}l} = 0$$

with x_e, l_e as the giving the location of the local minimum. For the case $\mu = 0$, the first criterion can only be fulfilled on lines of constant baselength or constant center-of-base of the droplet. This makes it possible to give an analytic constraint from the first condition, so the second criterion only has to be evaluated on one-dimensional subspaces.

When going to a system with a finite driving force, the manifolds on which to evaluate the second expression are given by an implicit equation that can still determined numerically. This gives a tool to track saddle points, i.e. points that are stable in one dimension but unstable in the other, in the bifurcation diagram close to the annihilation point with precision similar to the level obtained with Auto07p for small contact angle droplets. It also makes it possible to compute the stability information of the local extrema, unlike the Auto07p analysis.

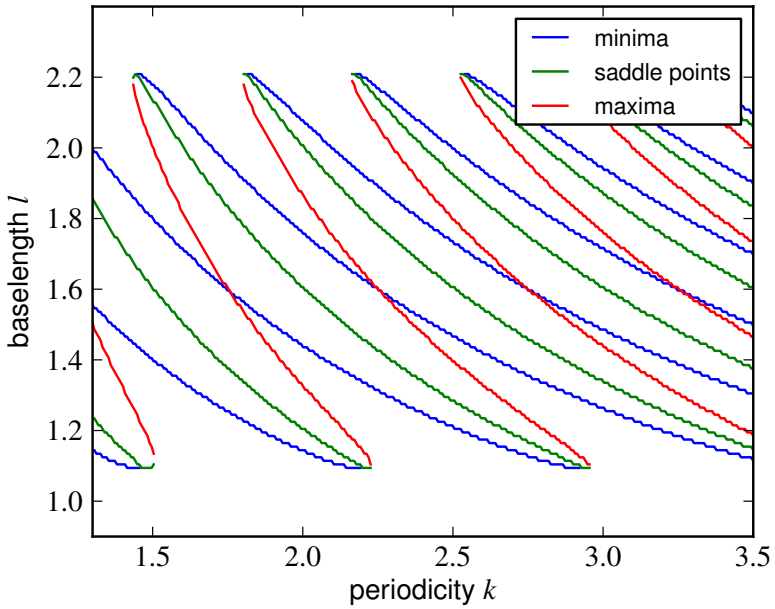

Fig. 5.7: Stability of the solution branches obtained from the energy landscape for different k in a neutrally wetting system without driving force, showing the same snaking behavior. The solution branches change from a stable solution to a saddle point whenever the periodicity is commensurable with the solution corresponding to the minimum or maximum wetting energy of the substrate. Parameters: $w_0 = 0$, $\Delta w = 0.2$

This gives a snaking diagram similar to Fig. 5.3(a), but with corresponding stability information, as presented in Fig. 5.7. Seeing that the two main branches switch between stable and unstable was expected, but there is a certain subtlety in the transition. As the stable branch reaches the minimum or maximum baselength and annihilates with the antisymmetric solution branch, it first becomes a saddle point with one stable and one unstable direction. Only at the turning point it becomes completely unstable, turning the saddle into a maximum.

For very low periodicities, i.e. the limit of sparse defects, this transition to a maximum actually does not occur, but the branch only switches between minimum and saddle-point. With increasing periodicity, the number of stable solutions increases, leading to the point where it resembles a continuum of solutions with contact angles between the static advancing and static receding contact angle.

The baselength of the minimal or maximal stable solution branch also increasingly approaches the baselength given by the minimum or maximum wetting energy. So for droplets significantly larger than the characteristic length scale of the defects, the minimum and maximum wetting energy give a good estimator for the minimal or maximal observed contact

angle.

5.2 Dynamics

The discussion up to this point only covers the conditions under which pinned droplets exist. These results can now be combined with the results from full dynamical simulations to give a full picture of the depinning/repinning process of droplets on heterogeneous substrates.

With BEM simulations for the case of $k = 10$ and a low slip length, the depinning point from the static limit was recovered. That means at the driving force where no more stationary solutions exist, the first moving droplet solutions were found. For driving forces higher than the depinning force, the classic stick-slip motion was observed.

5.2.1 Introduction: Sniper bifurcation

A classical model for a stick-slip motion of a droplet on a periodically patterned substrate[85] is a point mass in a sinusoidal potential with over-damped dynamics and a volume force acting on it. The governing equation of motion that describes the motion of the particle position x over time t, also known as Adler equation[2, 79], takes the following form:

$$x(t)' = \mu + \sin(x(t))$$

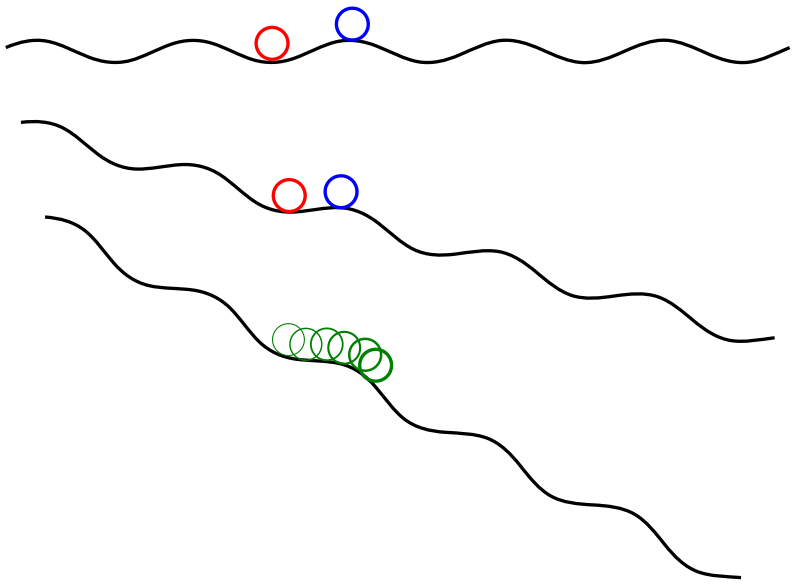

Fig. 5.8: Illustration of a particle on a periodically structured substrate. The driving force points down, so an increased slope represents an increased driving force. In the over-damped limit and for small heterogeneities, the observed dynamics can be approximated by the Adler equation.

with the prime denoting the derivative with respect to time. This system can be thought of as a particle on a sinusoidal substrate that gets tilted with a constant volume force pointing down, as illustrated in Fig. 5.8. As the inclination increases, the local energy minimum

becomes more and more shallow, until the stable static solution (red) and the unstable static solution (blue) annihilate and a periodically moving solution (green) appears, when no more local minima exist.

The periodically moving solution features a stick-slip motion where the system slows down in the region where the stable and the unstable solution branch annihilated. The velocity of the solution (i.e. the inverse of the periodicity of the motion τ) after depinning, for $\mu > 0$ scales as $u \propto (\mu - \mu_{\text{crit}})^{0.5}$, with $\mu_{\text{crit}} = 1$ for the Adler equation. The occurring bifurcation is called "Saddle-Node Infinite PERiod" (SNIPER) bifurcation, as the period diverges close to the critical point.

5.2.2 Observations

Using the BEM code, the time evolution of droplets driven on substrates with different periodicities and different wetting heterogeneities was modeled. The simulations did not only display the classical stick-slip motion associated with a single Adler equation. Depending on the periodicity of the substrate, either a synchronized stick-slip motion can be observed or a desynchronized motion, where the maximum of the front and the back contact line are phase shifted by approximately half a period. This is shown in Fig. 5.9. The strength of the heterogeneity and the driving force were kept constant, but the periodicity of the heterogeneity was changed by a quarter of a period from $k = 10$ to $k = 10.25$.

This desynchronized motion is especially pronounced when the droplet baselength matches the periodicity of the substrate, i.e. the previously discussed case in the static limit where the critical depinning force is reduced. In this case the velocity variation is significantly lower than in the synchronized case. A small increase in the velocity of the other contact line occurs whenever a contact line has maximum velocity. That means, while they are moving desynchronized, a coupling of the dynamics of the two contact lines takes place.

Fig. 5.10(a) shows the average velocity of the droplet over the driving force for different slip lengths. While the droplet velocity increases with increasing slip length and increasing driving force acting on the droplet, another phenomenon is observed: For higher slip lengths, the point where no more depinned state is observed shifts to lower driving forces. That means there is not one critical driving force where the system changes from pinned to periodically moving solutions, but rather a range of bistability where both periodically moving and pinned solutions coexist.

Together with this, a discontinuity in the droplet velocity at the transition was observed, indicating that the square root scaling of the velocity does not hold anymore. These imply a change in the bifurcation scenario away from the SNIPER bifurcation.

To show how the dynamics change, Fig. 5.10(b) displays the minimum and maximum observed baselength over one period of motion for periodically moving states, together with the static states. As the driving force, and thus the droplet velocity increases, the change in baselength decreases, as the droplet has less time to respond to the varying substrate wetting energy.

With increasing slip length, the variation in the baselength decreases too, i.e. the droplet deforms less over the course of one period. Also, the lowest driving force where a periodically moving solution is observed decreases. As the static energy landscape and therefore the static solutions not change with the slip length an increased range of bistability can be seen. This implies that two competing time scales play a role, one determining the deformation of the droplet and the second one determining the periodicity of the motion.

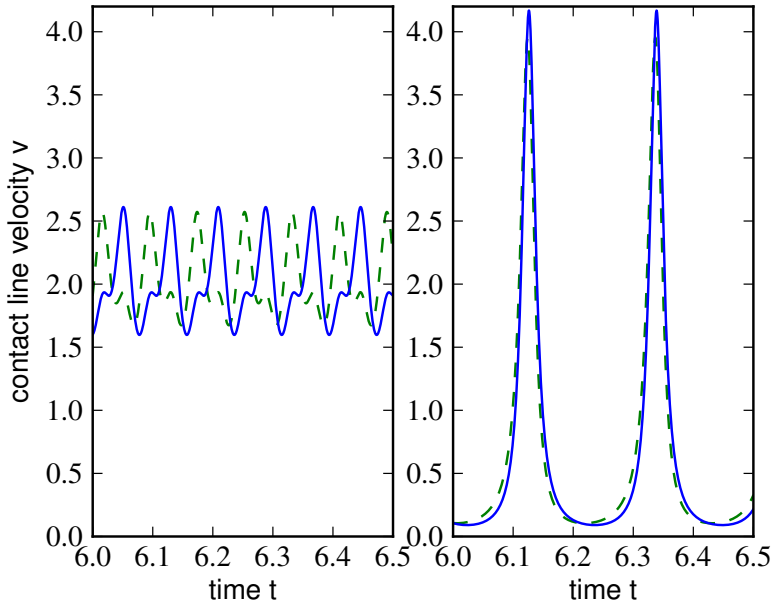

Fig. 5.9: Velocity of the front and the back contact line for $k = 10$ (left), $k = 10.25$ (right), showing desynchronized and synchronized motion with a small change in the periodicity of the substrate for $w_0 = 0$, $\Delta w = 0.2$, $\mu = 0.35$

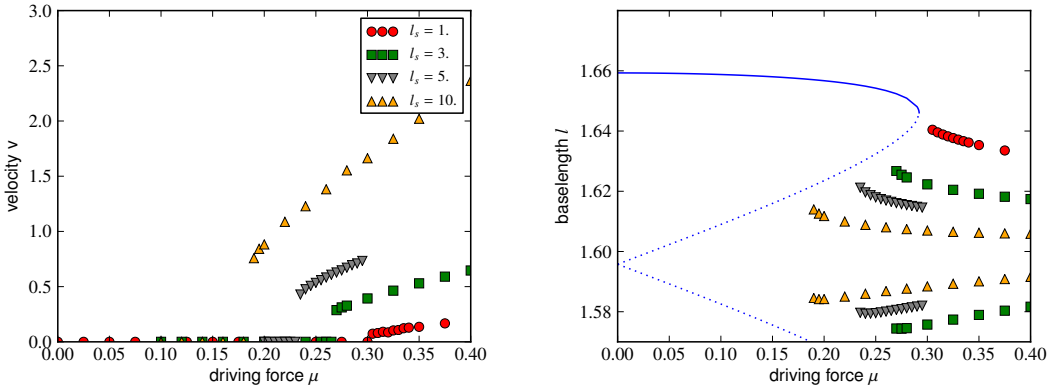

(a) (b)

Fig. 5.10: (a) Observed average droplet velocity over driving force for different slip lengths showing varying range of bistability for $w_0 = 0$, $\Delta w = 0.2$, $k = 10$

(b) Observed minimum and maximum droplet baselength in one period (symbols) plus static solution branches (full lines for stable, dotted lines for unstable) over driving force for different slip lengths, $w_0 = 0$, $\Delta w = 0.2$, $k = 10$.

5.2.3 Mechanism

To get a better understanding for the dynamics, it is instructive to observe the interfacial energies and contact line velocities over the position of the droplet on the substrate. This might provide an insight in the change of the dynamics. The curves were reconstructed from dumps of the droplet shape taken from multiple periods and smoothed with an interpolating spline for presentation.

Fig. 5.11(a) shows how the droplet baselength varies over over period in space. While the average baselength is quite similar for both slip length, the oscillation is significantly smaller for the high slip length case as indicated by the minimal/maximal baselength plot presented previously.

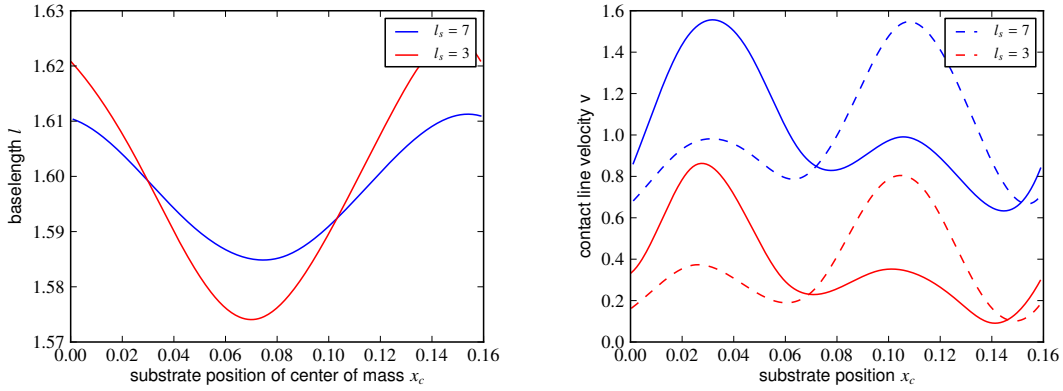

(a) (b)

Fig. 5.11: (a) Baselength of the moving solution over center of mass for different slip lengths, showing increased variation in baselength with reduced slip. System parameters: $w_0 = 0$, $\Delta w = 0.2$, $k = 10$
(b) Contact line velocity over the center of mass for different slip length, showing the alternating oscillation and decreased average velocity for decreased slip length for $w_0 = 0$, $\Delta w = 0.2$, $k = 10$. The total fluctuation amplitude is changed only slightly compared to the change in the average velocity.

When comparing the graph to the contact line velocities in Fig. 5.11(b), it becomes clear that the velocity of the front or the back contact line is maximal when the baselength is close to the average baselength. The desynchronized contact line motion is observed again, with the second small maximum synchronized with the maximum of the other contact line.

It is interesting to observe that the difference between the minimal and maximal contact line velocities is similar for both slip lengths. The total velocity is significantly higher for the high slip length case, giving the droplet less time to adapt to underlying substrate by deformation.

One of the hypotheses for the origin of the observed bistability is that a faster moving droplet is strongly deformed due to hydrodynamic stresses. This allows the droplet to store in the configuration of the free interface to overcome energy barriers. To test this hypothesis, Fig. 5.12 shows the total energy (excluding the gravitational energy) of the configuration at different substrate positions. While it displays the same oscillating behavior, the absolute

change is very small with less than 0.5% of the total configurational energy.

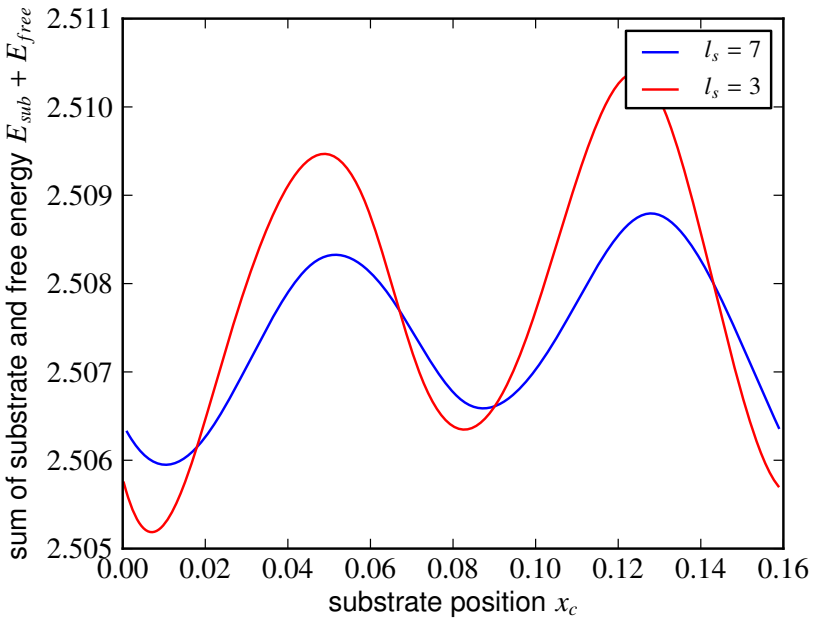

Fig. 5.12: Sum of wetting and free interface energy over the center of mass for different slip length, showing slightly decreased fluctuation for higher slip for $w_0 = 0$, $\Delta w = 0.2$, $k = 10$

This observation indicates that the droplet does not so much store energy to cross the energy barriers, as it bypasses them by not going through each local minimum in the energy landscape. This might be explained by the increased translational velocity with increasing slip length, with only a smaller change in the velocity variation over one period. The question is which underlying process is responsible for this behavior and if there is a reduced model capable of reproducing this change in the bifurcation scenario.

5.3 Droplet motion as coupled ODEs

A single Adler equation captures the relevant dynamics of the depinning at a single defect[85], as mentioned previously. The dynamics of an Adler equation can also be written as gradient dynamics of a particle in a one-dimensional energy landscape. In this form, the velocity for a given configuration is determined by the gradient of the energy landscape at that point and a mobility factor that relates the gradient to a velocity.

One approach to modeling a moving droplet with two contact lines would be to couple two Adler equations, but this requires picking arbitrary coupling constants and friction coefficients. To give a more robust derivation, this section presents a model for the droplet motion as gradient dynamics on the static energy landscape given by the center and baselength of the droplet presented previously.

As the last section showed that there is only a small change in the total configurational energy, it can be assumed that the free interface is now close to the equilibrium configuration. This makes it possible to introduce a simplified, energy independent expression for the energy

of the free interface depending on the baselength. The question is if such a simplified droplet model consisting of two coupled modes for translation and deformation can reproduce the behavior observed in the full Stokes simulations.

5.3.1 Obtaining the coefficients

The naive assumption is to apply a friction law with a contact line velocity proportional to the deviation from the equilibrium contact angle at both contact lines. This leads to equal mobilities for the translation and deformation mode. Previously, on droplets simulated with the full dynamics, the observation was made that apparently the time scales of translation and deformation vary with the slip length. This indicates that the assumption of equal mobilities for these two modes does not capture the underlying dynamics.

A suitable approach to estimate mobilities for the two modes is by determining them in two different systems where the contributions are decomposed: The deformation mobility, i.e. how fast the droplet changes its baselength for a gradient in the configurational energy, can be determined by studying the relaxation of a droplet with a non-equilibrium baselength on a homogeneous substrate. The translation mobility can be obtained by introducing a volume force and plotting the final translation velocity over the gradient of the free energy corresponding to the force.

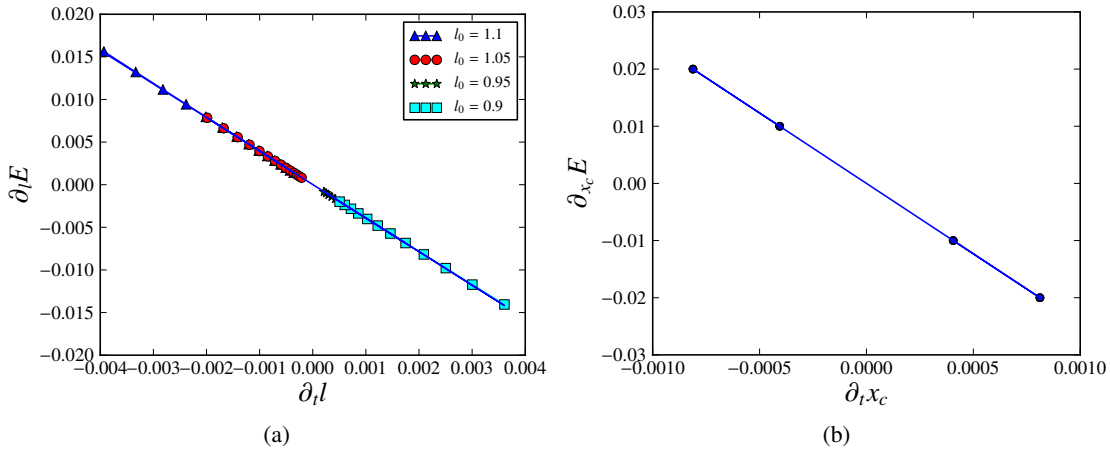

Fig. 5.13: (a) Energy gradient over velocity of the baselength mode close to equilibrium, used to obtain the mobility. The systems were initially perturbed by $\pm$ 5 and 10%, with the initial baselength l_0 given in the legend, $l_s = 0.01$, $w_0 = -1/\sqrt{2}$
(b) Energy gradient over center-of-base velocity to obtain the mobility, $ls = 0.01$, $w_0 = -1/\sqrt{2}$

For the center-of-base direction, the gradient is given directly by the driving force and the velocity is the steady state velocity the droplet approaches. Determining the local gradient of the free energy for the deformed droplet is less straightforward. To obtain it, first the configurational energy over time was determined from the shape of the droplet. The information of the baselength over time and the free energy over time were used to estimate the local gradient

from the time series E_i, l_i as

$$\frac{\partial E}{\partial l}\left(\frac{(l_{i+1}+l_i)}{2}\right) \approx \frac{E_{i+1}-E_i}{l_{i+1}-l_i}$$

giving the velocity of the deformation change for a gradient in the configurational energy. By using a linear fit on both datasets, the mobility of the translation and the deformation mode are estimated.

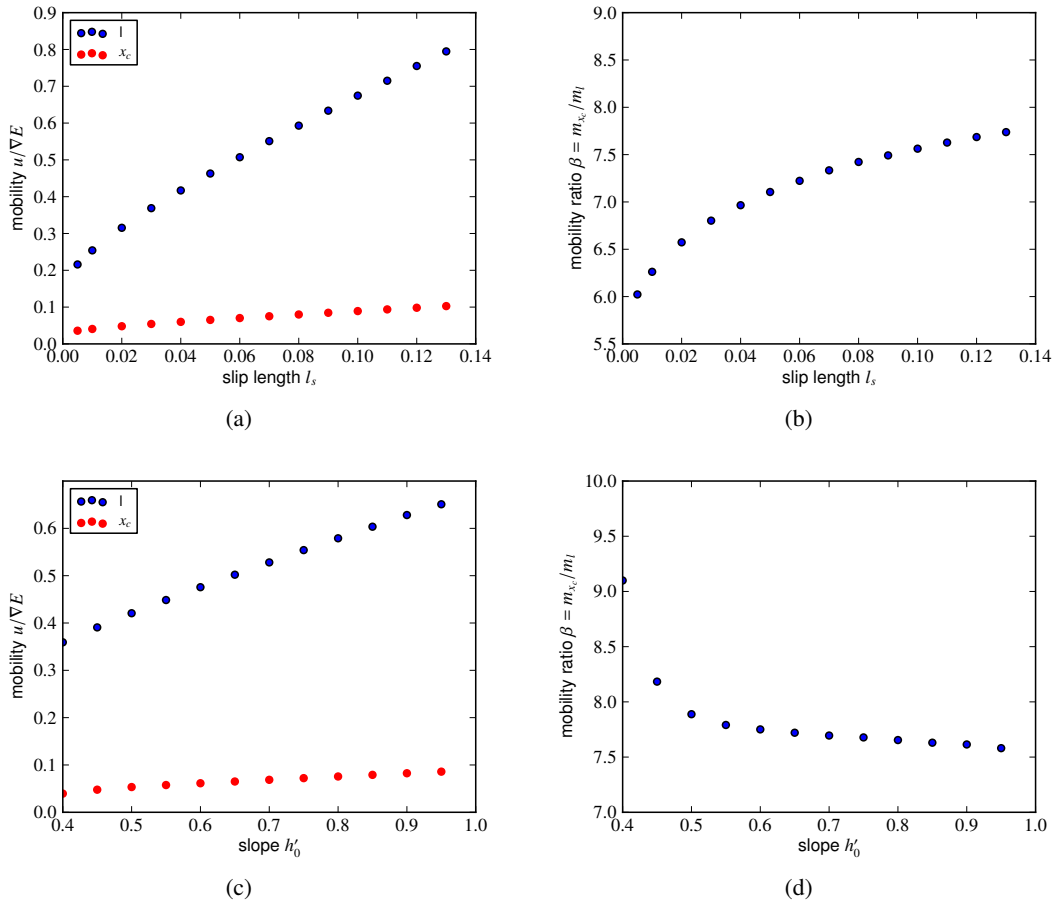

Fig. 5.14: (a) mobility of the center-of-mass mode and the deformation mode over the slip length for a contact angle of 45° (slope $h' = 1$) (b) ratio of the mobilities over the slip length of Fig. 5.14(a)
(c) mobility of the center-of-mass mode and the deformation mode over the slope of the fluid interface at the contact line $h'_0 = \tan\theta_0$, with θ_0 as the microscopic contact angle, for fixed slip $l_s = 0.1$ (d) ratio of the mobilities over h'_0 of Fig. 5.14(c)

Figure 5.13(a) shows the obtained trajectories of a 45° droplet in the thin film limit that was initially deformed by 5 and 10% in either direction. After an initial relaxation process (not displayed here), all initial conditions approach a similar state while approaching the equilibrium shape. This is confirmed by the collapse of the trajectories in the plotted region.

Fig. 5.13(b) shows the gradient in the energy landscape over the translation velocity of the droplet in the same system. The observed mobility of the translation mode is significantly lower than the mobility of the deformation mode. At this point, it should be remarked that a model of two independent contact lines would exhibit a mobility ratio of 4, as discussed later on, due to the chosen parameterization in terms of baselength and center-of-base.

From these simulations, the mobility as ratio between the free energy gradient and the velocity was derived for different slip lengths, as shown in Fig. 5.14(a), and different contact angles, as shown in Fig. 5.14(c). It shows that both mobilities are increasing with increasing slip length and contact angle, with the mobility of the deformation mode always being significantly higher than the mobility of the translation mode.

Another very relevant quantity to consider is the ratio of the two mobilities. When considering the droplet dynamics as two independent contact lines only coupled through the energy functional of the free interface, the ratio between the two mobilities should be independent of slip length and equilibrium wetting energy. This does not hold for the presented parameter range. Fig. 5.14(b) shows the ratio increasing with increased slip length, while Fig. 5.14(d) shows that the mobility of the deformation mode compared to the translation mode decreases with increasing contact angle.

Up to this point, all results were obtained in the thin film limit. The same approach can be taken with the BEM code for high contact angle droplets. In the range where the system changed between the two depinning scenarios, the observed mobilities change significantly. Fig. 5.15(a) shows the mobilities of the translation and the deformation mode for a slip length $l_s = 0.1$. As for the low contact angle case, the mobility of the deformation mode is higher than the mobility of the displacement mode.

When increasing the slip length to $l_s = 3$, both mobilities increase, but now the translation mobility is higher than the deformation mobility. This is shown in figure 5.15(b). So not only the overall mobility changes with the slip in the system, but also the ratio of the two mobilities changes significantly.

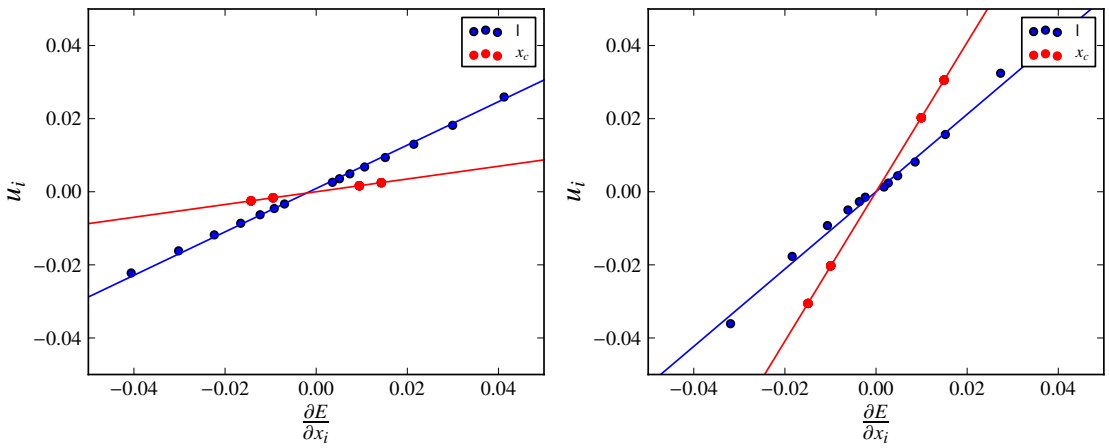

Fig. 5.15: (a) energy gradient over velocities for translation and deformation mode for 90° droplets, $l_s = 0.1$
(b) energy gradient over velocities for translation and deformation mode for 90° droplets, $l_s = 3$

A helpful mental model to understand the effect of bulk fluid dynamics in the high slip case is a droplet on a full-slip substrate in vacuum. While an infinitesimal volume force in a system without friction will lead to the droplet accelerating to arbitrary high velocities, the mobility of the deformation mode will still be limited by the relaxation time scale of a free interface.

Fig. 5.16 shows the mobilities obtained through a linear fit of data sets as presented in Fig. 5.15(a), 5.15(b) for different slip lengths. Both the center-of-base mobility and the baselength mobility are increasing, but the baselength mobility seems to slowly converge to a mobility dominated by the bulk deformation. This leads to a crossover where the mobility in center-of-base direction is higher than the mobility of the deformation mode.

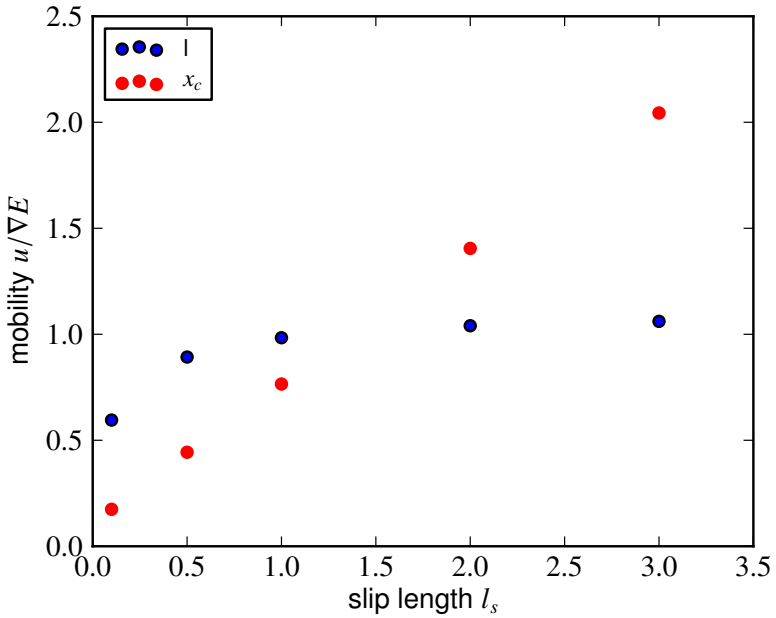

Fig. 5.16: Observed mobilities for 90° droplets over the slip length showing the crossover between the mobilities

The magnitude of the mobilities is less significant, as one mobility can be eliminated by rescaling the time. The ratio of the two mobility has to remain in a reduced model for the droplet motion, though, as it can not be scaled out. While it will not influence the static droplet solutions, it will have an influence on the dynamics observed for moving droplets.

5.3.2 Model equations

To derive the equations of motion, assume the total droplet configuration energy to be the slightly simplified expression introduced previously

$$\tilde{E} = \tilde{w} \int_{\tilde{x}_c-\tilde{l}}^{\tilde{x}_c+\tilde{l}} \cos(2\pi k y/l_0) dy - \tilde{\mu} x_c + \tilde{a}(\tilde{l}-\tilde{l}_0)^2$$

with the first part giving the contribution of the substrate wetting energy, the second part giving the gravitational contribution and the third part the configuration energy of the free energy, modeled as elastic spring. Integrating it gives

$$\tilde{E} = \frac{\tilde{w}\tilde{l}_0}{\pi k}\cos(2\pi k/l_0\tilde{x}_c)\sin(2\pi k/l_0\tilde{l}) - \tilde{\mu}x_c + \tilde{a}(\tilde{l}-\tilde{l}_0)^2$$

With the substitution $x_c = 2\pi k/l_0\tilde{x}_c$ and $l = 2\pi k/l_0\tilde{l}$ to eliminate the periodicity from the system and after dividing the whole equation by $(2\tilde{a}\tilde{l}_0^2)/(2\pi k)^2$ to eliminate one of the free parameters, the equation takes the following form:

$$E(x_c,l) = w\cos(x_c)\sin(l) + \mu x_c + 0.5(l-l_0)^2$$

Here, w represents the non-dimensionalized strength of the heterogeneity and μ the strength of the driving force. The length l_0 gives the equilibrium baselength on a homogeneous substrate modulo the periodicity of the heterogeneity.

The length scale is non-dimensionalized with the periodicity of the substrate, the driving force and strength of the heterogeneity are non-dimensionalized with the spring constant of the free interface. The equations of motion can be introduced now as gradient dynamics, with the velocity proportional to the gradient of the energy landscape. After rescaling the time with the mobility in center-of-base direction, the following equations of motion describe the simplified dynamics:

$$\frac{\mathrm{d}x_c}{\mathrm{d}t} = -\frac{\partial E}{\partial x_c} = \mu - w\sin(x_c)\sin(l)$$

$$\frac{\mathrm{d}l}{\mathrm{d}t} = -\frac{1}{\beta}\frac{\partial E}{\partial l} = (-(l-l_0) - w\cos(x_c)\cos(l))/\beta.$$

with $\beta = \frac{m_{x_c}}{m_l}$ as the ratio of mobilities. For this set of ODEs, static and periodically moving solutions can be computed with Auto07p, giving us bifurcation diagrams analogous to the full dynamics simulations.

To understand how the dynamics depends on the initial conditions, it is also possible to numerically integrate them directly to obtain the trajectories of the system for different initial conditions and see the relaxation to the static or periodically moving solutions.

One question that should be addressed is why the cross-terms are assumed to be zero: The change in baselength with a gradient in center-of-base direction has to be zero in first order, as it has to be symmetric under inversion of the driving force. That means the baselength should not increase when the driving force points in one direction and decrease when it changes sign. The same holds for a change of the center-of-base with a gradient in baselength direction, at least in the limit of no driving force, where the system is symmetric.

5.3.3 Bifurcation diagrams, scalings

The first case to study is a system with fixed strength and periodicity of the heterogeneity, but varying ratio of the mobilities. The question is if the ODE system shows the same behavior as the droplets studied in the direct numerical simulations. The parameters to consider are again the velocity and the baselength as the system goes through the periodic motion.

Fig. 5.17(a) shows the obtained average velocity (i.e. the inverse of the periodicity) over driving force for the periodically moving solutions depending on the ratio of mobilities β. The chosen equilibrium baselength is $l_0 = 0.1$, i.e. the case where the droplet is not quite commensurable with the substrate, thus breaking the symmetry in baselength direction.

The system shows the same bistability where both moving and pinned solutions coexist. As observed in the full simulations, the minimal driving force where a periodically moving droplet solution exists changes with the ratio of mobilities. A higher mobility in the translation direction leads to a lower minimum driving force. The velocity also drops increasingly sharp at the critical point with increasing β.

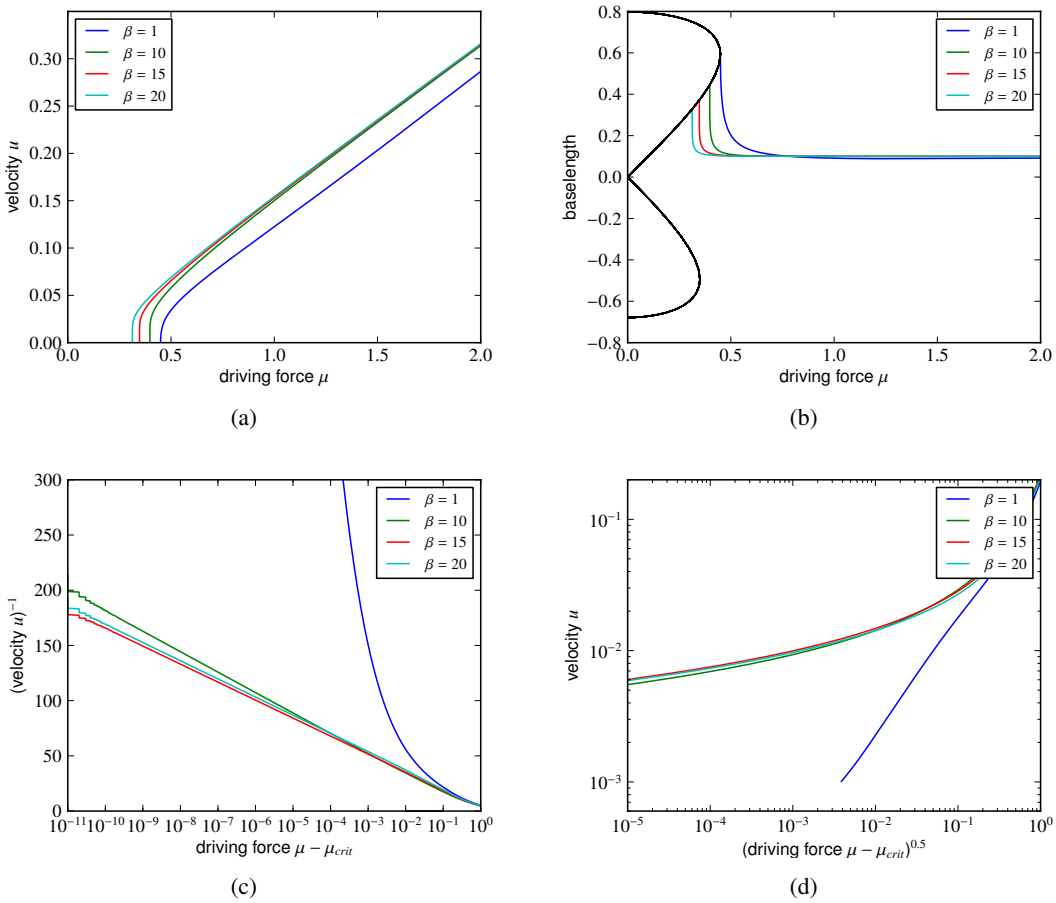

Fig. 5.17: (a) time averaged velocity over driving force for different mobility ratios showing a changing range of bistability with changing mobility ratio β
(b) baselength over driving force for different mobility ratios plus the static solution branches (black) showing the transition from a homoclinic bifurcation to a SNIPER bifurcation
(c) velocity over driving force rescaled to show logarithmic divergence, as predicted for a homoclinic bifurcation
(d) velocity over driving force rescaled to show square root behavior, as predicted for a SNIPER bifurcation

To confirm the similarity, Fig. 5.17(b) shows the average baselength of the solution branches over the driving force. The point where the periodically moving solution approaches the static branch shifts with increasing beta, with the slope of the approach becoming increasingly sharp.

To confirm the change in the bifurcation scenario, it is possible to check if the scaling of the velocity changes as expected. Fig. 5.17(c) shows the periodicity over the logarithm of the distance from the critical point, indicating that the results for $\beta = 10, 15, 20$ display a homoclinic bifurcation. Fig. 5.17(d) shows the linear scaling when plotting over $(\mu - \mu_{crit})^{0.5}$ which corresponds to a SNIPER bifurcation for $\beta = 1$, while the other three cases deviate.

It turned out that a two-dimensional configuration space is sufficient to obtain the transition between sniper and homoclinic bifurcation. Introducing an additional degree of freedom to represent the configuration of the free interface was not necessary.

Around the saddle point (x_e, l_e) that is approached by the periodically moving solution, the system can be linearized using $x_c = x_e + \delta x$ and $l = l_e + \delta l$ in the form

$$\begin{pmatrix} \delta x' \\ \delta l' \end{pmatrix} = A \begin{pmatrix} \delta x \\ \delta l \end{pmatrix}$$

with A of the form

$$A = - \begin{pmatrix} \frac{\partial^2 E}{\partial x_c^2} & \frac{\partial^2 E}{\partial x_c \partial l} \\ \frac{1}{\beta} \frac{\partial^2 E}{\partial x_c \partial l} & \frac{1}{\beta} \frac{\partial^2 E}{\partial l^2} \end{pmatrix} \Bigg|_{x_c = x_e, l = l_e}$$

Alternatively it can be written as

$$x_1' = \lambda_1 x_1$$

$$x_2' = \lambda_2 x_1$$

with λ_1, λ_2 as the eigenvalues of A plus x_1 and x_2 as the two coordinates in the base of the corresponding eigenvectors. For a saddle point, $\lambda_{1,2}$ have opposite signs, as the system is stable in one direction and unstable in the other.

For a homoclinic bifurcation the periodically moving solution will approach the saddle point from the stable direction and eject along the unstable direction of the linearized system. If the periodically moving solution is stable, the time scale of this process is dominated by the time required to leave the proximity of the saddle point, determined by the unstable eigenvalue. The scaling of the period close to the critical point and the eigenvalues at the critical point of a homoclinic bifurcation can be related by the following equation, as explained in detail by Gaspard[79, 28]:

$$\mu - \mu_c = C e^{-\lambda_u T}$$

Here, $\mu - \mu_c$ is distance from the critical driving force, λ_u the unstable eigenvalue of the linearized system at the saddle point, T the periodicity of the obtained solution and C determined by the dynamics away from the region close to the saddle point. The dynamics away from the saddle point is assumed to change only slowly with μ, even if the system is close to the critical point.

Figure 5.18(a) plots the eigenvalues of the unstable branch that is approached by the periodically moving solutions. It shows the unstable eigenvalue approaching zero as the branch approaches the turning point. The negative eigenvalue of the solution branch changes too, but relatively little, compared to the absolute value. As shown in Fig. 5.17(a), the point where the homoclinic bifurcation occurs moves to higher driving forces, as the mobility ratio β decreases. Therefore, even as λ_u increases with decreasing β for a fixed driving force, λ_u at μ_c decreases and approaches zero.

The previously presented velocity data can now be rescaled with the eigenvalues at the branching points of the homoclinic bifurcation, as presented in Fig. 5.18(b). It shows a very good agreement with the predicted scaling, with the point where the scaling breaks down moving closer to the critical driving force with β approaching the transition point.

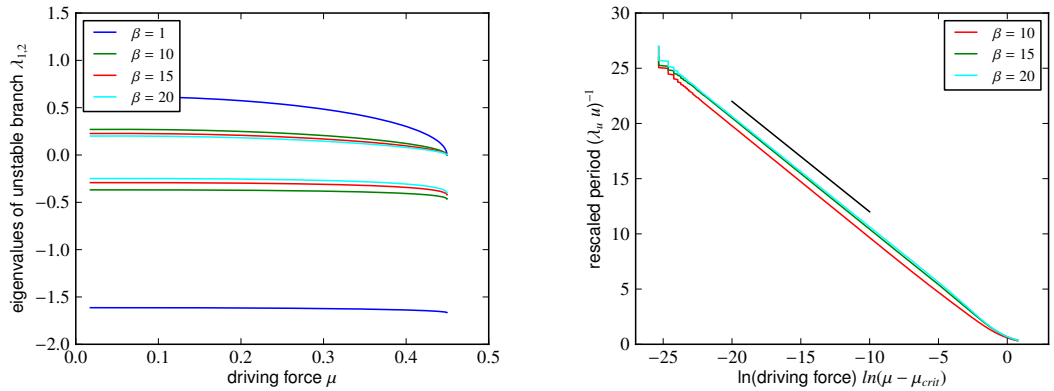

(a) (b)

Fig. 5.18: (a) Eigenvalues of the unstable branch that is approached by the periodically moving solutions for different mobility ratios β, showing the unstable eigenvalue approach 0 at the driving force where the last stable solution annihilates.
(b) Velocity rescaled with the unstable eigenvalue showing the scaling predicted for homoclinic bifurcations, the black line represents a slope of -1

The critical driving force where the bifurcation occurs can be determined for different mobility ratios and periodicity mismatches l_0, as shown in Fig. 5.19(a). As the periodicity mismatch changes, the critical driving force where no more pinned solutions exist changes, as discussed previously. At a value of β just above 5 that varies slightly with l_0, the critical driving force starts decreasing for all cases presented here. That means the critical point where no more moving solution exists is not at the turning point of the static branch anymore and the bifurcation scenario changed.

The transition region for the different curves has been replotted in 5.19(b). While the curves are qualitatively similar, no sensible scaling law to describe the transition could be derived from them. For the case $l_0 = 0.6$ the range of bistability is decreasing most slowly, as the system is close to the state where the baselength of the pinned droplet equals the equilibrium baselength. This is also indicated by the fact that this state has the highest critical driving force.

5.3.4 Sample trajectories

To obtain the domains of attraction of the system, the differential equations were integrated for different initial conditions and plotted in Fig. 5.20(a) for a set of parameters where the bistability was observed. They were colored according to their classification as approaching the periodically moving or the static state.

It shows both trajectories approaching a periodically moving solution, colored red, and

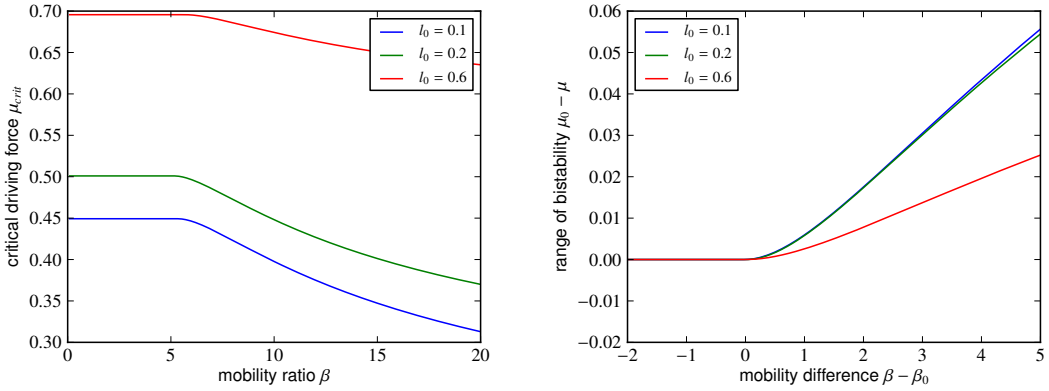

(a) (b)

Fig. 5.19: (a) Critical driving force where repinning occurs over ratio of mobilities β showing the transition between the bifurcations for different equilibrium baselengths l_0.
(b) Zoom of the transition region between the homoclinic and the SNIPER transition for different l_0

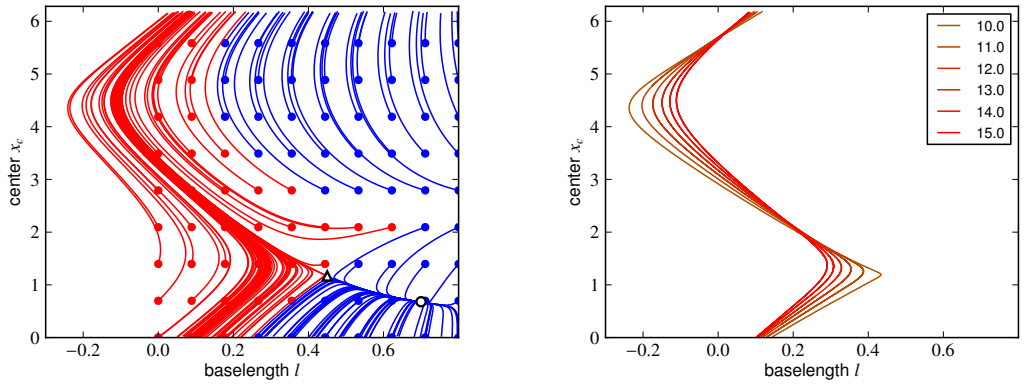

(a) (b)

Fig. 5.20: (a) Trajectories obtained from different initial conditions (indicated by full circles), color-coded for moving(red) and finally pinned (blue) solutions plus local minimum (black circle) and saddle point (black triangle), $\beta = 15$, $\mu = 0.4$, $l_0 = 0.1$.
(b) Periodic solutions obtained for different values of β showing the reduced variation for the same driving force and underlying wetting energy, $\mu = 0.4$, $l_0 = 0.1$.

trajectories approaching a local minimum, colored blue, coexisting. All solutions with a baselength lower than the presented ones approach the periodically moving solution, all solutions with a higher initial baselength approach the pinned state. This graph illustrates how the system does not need a third degree of freedom to store energy to cross the saddle point, but rather bypasses it.

Fig. 5.20(b) shows the obtained periodic solutions for different mobility ratios, with the system coming increasingly close to the saddle point with decreasing β. The trajectories approaching the periodically moving solution show the behavior expected from a homoclinic bifurcation. With decreasing β, i.e. moving closer to the bifurcation point, the turning point moves closer to the saddle point of the system.

5.4 Reducing model complexity

A recurring point in the previous discussions was up to which point the simplified models for the droplet dynamics hold. It is important to understand that, while full dynamical simulations in the Stokes limit or MD simulations might be able to capture most of the relevant physics, the dynamics of the fluid are just one component when going towards dynamics of complex fluid flows. When trying to incorporate for example surfactants or suspensions, simplified models, as the lubrication approximation, are unavoidable. Otherwise the numerical effort becomes unmanageable without foraying into high performance computing.

5.4.1 Full Stokes to contact line driven dynamics

It is possible to use the contact line driven dynamics model to describe the motion of droplets on heterogeneous substrates. This approach is related closely to the ODE model approach, as the change in the configurational energy with displacement of one of the contact lines directly determines the contact angle.

When first looking at the results obtained from the contact line driven dynamics model, there seems to be an increasingly good agreement between the motion of a droplet on a heterogeneous substrate obtained from the full simulations and from the contact line driven dynamics model. This is shown in Fig. 5.21(a), plotting the contact line velocity over one period for different slip lengths and in the quasi-static limit.

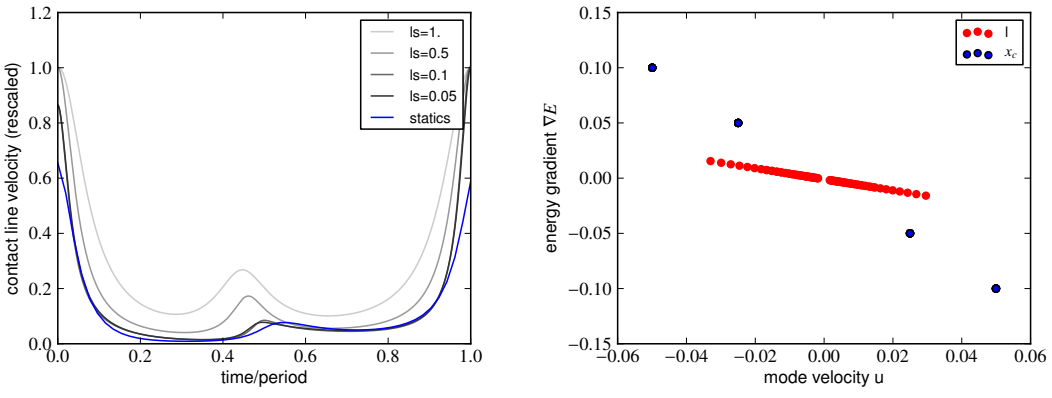

(a) (b)

Fig. 5.21: (a) Full BEM simulations and surface evolver results for the contact line velocity on a heterogeneous substrate, $w = 0.2$, $k = 5$, $f = 0.35$
(b) Mobilities derived from the contact line driven dynamics model for a 90° droplet, with the center of base mobility being exactly 4 times the mobility in baselength direction

But it turns out that it is difficult to obtain an quantitative agreement between the droplet shapes from the full dynamics and a contact line driven dynamics model for driven droplets. In first order, the time scale can be tuned so the change in the droplet baselength with the velocity matches the results from the dynamic simulations. At higher velocities, the thin film droplets display hydrodynamic tail formation already for moderate slip lengths, a feature that does not occur in a model that assumes the droplet shape to be close to the equilibrium configuration for a given baselength. This causes a strong deviation between the two models.

Another issue arises from dealing with the two contact lines independently. As shown previously, already for moderate slip lengths and very small driving forces the mobilities of the deformation and translation mode vary. By treating both contact lines independently, a varying ratio of the translation and deformation mobility can not be achieved in this model. Fig. 5.21(b) shows the dataset from which the mobilities were determined, showing that the center-of-base mobility is exactly 4 times the baselength mobility, as expected from this choice of variables. This ratio does not change with the friction coefficient, as the ratio $\Delta\Theta_i/x_i'$ only determines the timescale. Agreement with the results presented in the previous sections for droplets simulated in moderate slip length regimes, where the ratio of the two was changing with the slip length, can not be achieved. These findings indicate that even in the limit of low velocities and high contact angles the bulk fluid dynamics can not generally be neglected when studying the droplet motion.

One point where the contact line driven dynamics is very helpful is to study systems close to the depinning transition, as it does capture the approach of the critical point and the initial depinning mode when it is reached. This is especially relevant when going to 3-dimensional systems, where the time to run full dynamical simulations become prohibitively high.

5.4.2 Full Stokes to coupled ODE model

In the previous section, mobilities for the deformation and translation modes of the droplet were obtained from the full simulations. The one missing component for a quantitative comparison of the ode model to the full dynamical simulations is the opening of the parabola used to approximate the free energy of the interface. This is shown for a 90° droplet in Fig. 5.22(a), where a coefficient $a = 0.49$ was obtained as estimator in the equation

$$E(l) = E_0 + a(l - l_0)^2$$

with $l_0 = 1.59$ as shown previously and E_0 irrelevant, as only the gradient of the energy landscape is of any concern in the simplified model. The obtained values are a good approximation up to driving forces of approximately $\mu \approx 0.5$, as both l_0 and a change less than 5% in this range and in a range for the baselength l of ± 0.3. This sets an upper bound on the maximum defect spacing and strength, as the variation in droplet baselength should stay below it.

Instead of using the expression for the energy that was introduced previously, the energy functional without the non-dimensionalization using the same parameterization as the full simulations was employed to simplify comparison of the results. It has the form:

$$E = a(l - l_0)^2 - \mu x + w \int_{x-l/2}^{x+l/2} \cos(2\pi k y / l_0) dy$$

So the final system of ODEs to be integrated takes the form

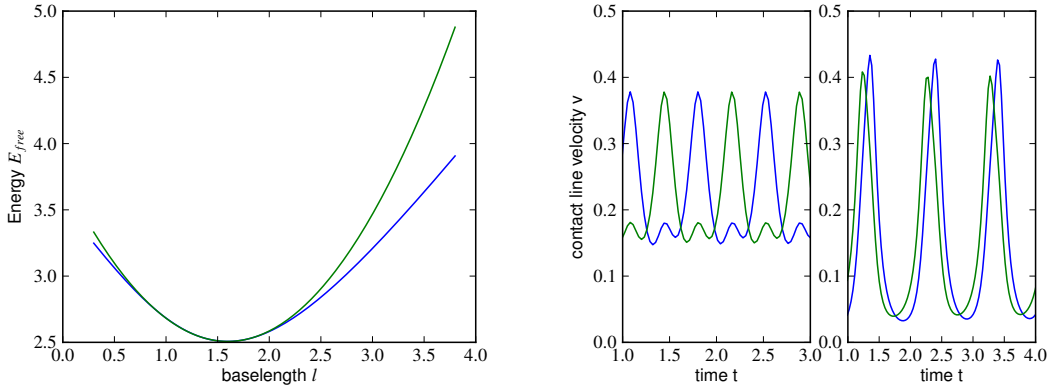

(a) (b)

Fig. 5.22: (a) Free energy of the static interface over baselength for 90° droplet (blue), fitted (green) to obtain a spring coefficient $a = 0.49$ for the ODE model.
(b) Contact line velocities for $w = 0.2$, $k = 10, 10.25$, $\mu = 0.4$ showing the changing phase shift. Mobilities equivalent to $l_s = 1$.

$$x' = m_x \frac{\partial E}{\partial x} = m_x(-\mu - 2w\sin(2\pi kl/2/l_0)\sin(2\pi kx/l_0))$$

$$l' = m_l \frac{\partial E}{\partial l} = m_l(2a(l-l_0) + w\cos(2\pi kl/2/l_0)\cos(2\pi kx/l_0))$$

with a and l_0 taken from the static configuration energy for $\mu = 0$ and the mobilities m_l and m_x taken from the fit of the full dynamics simulations on the homogeneous substrate introduced at the beginning of the section.

Comparing the results for homogeneous substrates from this model would be moot, as the mobilities were obtained by fitting the results of full dynamic simulations on homogeneous substrates. Therefore the dynamics on a homogeneous substrate has to match. The question is if the model reproduces the features of the dynamics on a heterogeneous substrate properly, i.e. the phase shift in the contact line motion, the depinning point and the change in the bifurcation scenario.

Fig. 5.23(a) shows the obtained average droplet velocities using the mobilities for different slip lengths. It shows average velocities that are quite comparable to the full dynamical simulation results for these system parameters presented previously and a strongly increasing range of bistability for the slip length above unity. The driving force where no more pinned solution exists agrees with the stability analysis of the energy landscape. The observed range of bistability is even larger than observed in the full dynamical simulations, indicating that the higher modes of droplet deformation still play a role.

This leads to the conclusion that this change in the bifurcation scenario can be explained based on the two basic modes of droplet deformation and translation without incorporating higher modes of droplet deformation for fixed contact line position. This is surprising, as it defies the original assumption that an additional degree of freedom capable of storing and gradually releasing energy would be necessary to cross the energy barriers. The non-symmetric mobilities allow for the system to bypass the saddle point at an even lower slip

length, between $l_s = 0.1$ and $l_s = 1$ in this simplified model than in the full model.

A quantitative agreement can not be achieved with this model, though, for macroscopic defect strengths and driving forces. This is also shown by the minimum and maximum observed baselength presented in Fig. 5.23(b). First, the fluctuation of the baselength is significantly lower for the ODE model with equivalent mobilities, leading to a more pronounced bistability. That means additional deformation modes of the free interface for a given contact line position can not be neglected completely.

Second, for the full dynamical simulations the average baselength seems to be higher due to hydrodynamic deformation. This effect can not be accounted for in a linear model, as the effect is symmetric under inversion of the direction of the driving force.

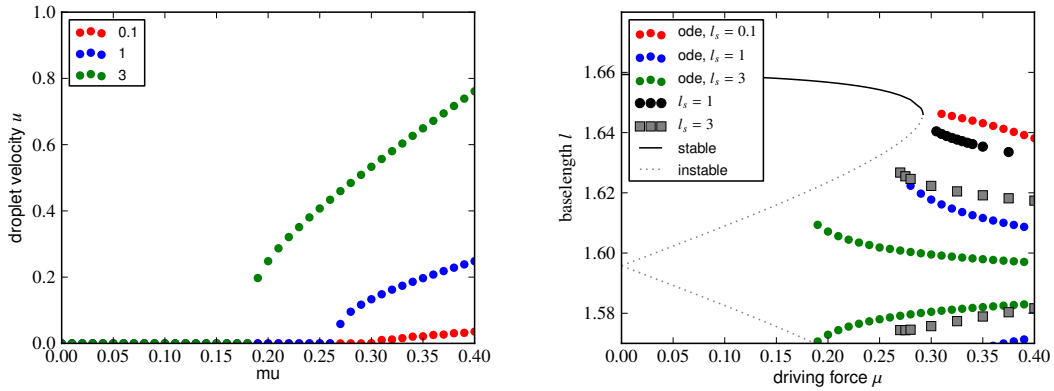

(a) (b)

Fig. 5.23: (a) Droplet velocities obtained from the ode model with mobilities taken from full dynamic simulations on homogeneous substrates, $k = 10$, $w = 0.2$
(b) Minimal and maximal baselength of solutions from full dynamic simulations and ODE model, $k = 10$, $w = 0.2$

Another aspect is also reproduced qualitatively: The system also shows the changing phase shift between the front and the back contact line depending on the relative defect spacing $1/k$, as illustrated in Fig. 5.22(b). For the same strength of the heterogeneity but slightly changed periodicity, the system gets closer to a complete halt with $k = 10.25$ where the contact lines are moving nearly synchronized. For the periodicity $k = 10$, the system approaches the pinned state for the same driving forces.

This model will fail at higher driving forces, as the assumption of the baselength dependent interfacial energy, i.e. a being independent of μ, is increasingly invalid for higher driving forces. This could be fixed by introducing a driving force dependent spring constant a, but goes beyond the scope of this strongly simplified model.

Another point that is not captured is the change of the baselength at higher velocities due to hydrodynamic deformation of the fluid interface. It can not be captured easily in a linear model, as change is independent of the direction of driving. This could be solved with a velocity-dependent term of the equilibrium baselength, though.

To conclude, for very low velocities, where the response of the system is purely linear, the ode model for the contact line motion gives a good agreement. As the higher modes of droplet deformation without displacement of the contact line and nonlinear responses of the system,

as the change in baselength due to driving, become relevant, it does not reproduce the results quantitatively.

5.5 Summary

The preceding chapter presented results on the statics and dynamics of droplets on a chemically heterogeneous substrate. For a substrate with a sinusoidally varying wetting energy, the range of stable droplet states depending on the periodicity of the pattern was presented. For periodicities that are small compared to the droplet baselength, stable solutions with the range of contact angles determined by the minimum and maximum wetting energy of the droplet were observed. As the length scale of the heterogeneity approaches the droplet size, a reduced number of stable droplet configurations was observed with a hysteresis that varies with the periodicity.

When introducing a volume force parallel to the substrate that acts on the droplet, the critical driving force where no more pinned droplet solutions exist has been determined depending on the substrate properties. For a defect length scale much smaller than the droplet size, the depinning force is directly determined by the wetting energy contrast. In contrast, as the periodicity approaches the length scale determined by the droplet, the pinning strength can be reduced significantly if the defect length scale is commensurable with the defect length scale.

Going beyond the statics of droplet pinning, the dynamics of driven droplets on a chemically heterogeneous substrate was modeled. Depending on the periodicity of the heterogeneity, a transition between the synchronized and desynchronized motion of the contact line was observed. For high slip lengths and a substrate commensurable with the equilibrium baselength of the droplet, a bistability was observed where both a static, pinned droplet and a periodically moving droplet are a solution. At a decreased slip length, moving droplets were only observed at driving forces where no more pinned droplet states exist.

To understand this transition, a simplified droplet model with a transition and a deformation mode was introduced. It represents the droplet motion as gradient dynamics on the energy landscape given by the static configuration energy depending on the droplet baselength and center. After estimating the mobility terms from the full droplet dynamics, the resulting set of ODEs was integrated to obtain static and periodically moving solutions. It was shown that this reduced two-dimensional model can reproduce the change in the bifurcation scenario only by varying the mobility ratio of the two modes.

6 Conclusions and Outlook

The present work offered an alternative perspective on the microscopic dynamics occurring when a contact line is driven over a chemically heterogeneous substrate. The change in the macroscopic contact angle when a heterogeneity is introduced is documented and explained with a velocity-dependent microscopic contact angle due to the sampling of the chemically patterned substrate. This challenges the common assumption that the static advancing contact angle together with the dynamics observed on a homogeneous substrate describes the dynamics on a heterogeneous substrate.

To get a better understanding of the underlying processes, the response of a free interface to a time-periodic driving has been studied. As a result, the scaling of the fluctuation amplitude with the distance from the contact line and the phase shift depending on the driving were obtained. These scaling differ from the results obtained using a traditional approach to model contact line dynamics on a heterogeneous substrate using a friction law, as proposed by Joanny[38]. This point should be approached experimentally to answer which model resembles observations more closely.

Based on these results, a simplified model for the motion over the heterogeneous substrate is proposed. The model is based on a mode expansion in terms of the displacement of the contact line in response to time periodic perturbations of the contact angle. This makes it possible to model the contact line motion by obtaining a self-consistent solution to a set of non-linear equations instead of running the full dynamical simulations, which significantly simplifies the problem. The idea is that the contact line displacement due to the heterogeneities encountered over the course of a period should be the same as the displacement due to a time dependent variation of the contact angle of the same structure.

The model was validated by determining trajectories on substrates with a sinusoidal modulation of the substrate wetting energy and on substrates with a randomized periodic modulation of the wetting energy. The randomized wetting patterns were created as superposition of sinusoidal variations of the wetting energy with random phase shift. On these substrates, the velocity dependent variation of the contact line displacement and time averaged wetting energies were determined. The results on the random heterogeneity present the strength of the mode expansion approach, as the numerical difficulty of the problem is determined by the smallest length scale of the underlying structure, which determines the number of modes that have to be considered. The complexity of the structure itself does not influence it.

The approach could be extended to three dimensions, i.e. to a system where the wetting energy varies along the contact line to allow for an easier comparison to experimental results. This would require solving the thin film equation in two spatial dimensions and goes beyond the scope of this work. Discussions are underway to approach this in collaboration with another research group that implemented such a code. This would give experimentalists[26] a tool to fit their obtained contact angle-velocity diagrams with a more suitable model than those obtained for a homogeneous substrate.

Even though this could not be achieved yet, this work clarifies that there are processes occurring between the molecular length scale and the length scale on which the system is

observed due to the non-constant wetting energy. These effects should not be neglected, but are not accounted for in current models. They go beyond the effects taken into consideration in the two most prominent theories for contact line motion, the molecular kinetic theory (MKT)[11] and the Cox-Voinov scaling [90], as MKT assumes hopping on molecular length scales and Cox-Voinov assumes a fixed microscopic contact angle in the continuum limit. Neglecting them, as done when assuming the system goes directly from one of these limits to the other one, is not appropriate for most system observed in reality.

One limitation of the numerical results in the present work is the small separation between the length scales of the slip, the characteristic length scale of the contact line fluctuations and the system size. This problem is twofold: On one side, an increased separation requires an increased refinement of the free interface with more colocation points. On the other side, the smallest length scale also limits the maximal time step when modeling the evolution of the system, which directly effects the running time. Improvements in computational power and the code base will make it possible to obtain stronger predictions concerning the problems discussed in the present work.

In the second part, a droplet driven with constant force instead of constant velocity was considered. Looking at the statics underlying the wetting of heterogeneous substrates, similar to the works of Kalliadasis [65], it became clear how not only in three dimensions, but also in two dimensions, the minimum and maximum wetting energy do not have to represent the minimum and maximum contact angle of stable solutions. This is a result of the finite length scale of the wetting heterogeneities. It also showed how with increasing driving force the range of observable advancing and receding contact angles decreases, until one stable solution remains.

Beyond the statics of wetting of heterogeneous substrate, the dynamics of droplets moving over heterogeneous substrates with defect length scales below the droplet size was studied. For high contact angle droplets in the high slip limit, range of bistability was observed where both pinned and depinned droplet solutions coexist for the same system parameters. It was surprising, as this is often associated with inertial effects, which do not play a role in the Stokes limit. The effect could be shown to correspond to a change in the bifurcation scenario from a SNIPER bifurcation to a homoclinic bifurcation with the corresponding change in the scaling of the velocity. The initial assumption was that this change is due to the finite relaxation time of the free interface leading to an alternative energy storage mechanism. This turned out not to be the case, as the change in the length of the free interfacial energy was observed to be very low.

The same change could be observed in a simplified ODE model for the droplet dynamics derived as gradient dynamics on the free energy presented for the statics. In this model the slip dependent dynamics of the droplet is represented by different mobilities of the translation and the deformation mode, without requiring an additional parameter to represent additional energy stored in the interface. This model is also relevant to the dynamical systems community, as it motivates and enables further studies of the transition between bifurcation scenarios. While bifurcations are a recurring topic in a range of fields, the transitions between bifurcation scenarios in dynamical systems have not been characterized systematically. Even though this model reproduced the transition, it did not succeed to reproduce the fluctuation of the droplet baselength after depinning accurately. This indicates that a model incorporating additional deformation modes of the free interface would be in order. It was discussed that this could be possible by deriving additional equations of motion for these building on the principle of minimum energy dissipation, as already proposed for moving contact line

hydrodynamics[57].

In this context, the question of comparability of the different droplet models, ranging from the quasi-static approximation over the ODE models, proposed in the present work and by Savva[66], to the thin film limit and the full Stokes model arises. This question was approached in the present thesis, but limited by the bounds on the slip length of the BEM code. As this question was not resolved satisfactorily, further work on this topic is necessary to determine the limits of validity of the different approximations. Understanding up to which point the models for the fluid dynamic aspect of the problem hold is important when moving to complex fluid flows. For example when coupling free interface flows with surfactant flows or colloids, the complexity of the model has to be reduced to obtain an addressable problem.

Another very relevant point is the comparability of these results to experiments. For the droplet depinning on striped substrates, a linear scaling of the velocity with the excess driving force was reported[89]. A linear scaling agrees with the predicted scaling far away from the critical point, but not close to the depinning. This indicates that more precise experiments on well-controlled substrates close to the depinning transition are indispensable. Preparing substrates with a controlled heterogeneity is very difficult, just as observing the dynamics close to the contact line in an evolving system. But recent progress with confocal microscopy[1] and micro-fabrication techniques should allow for this problem to be revisited experimentally.

In addition, a code to study free interface flow problems in the Stokes limit using boundary element methods was implemented. Beyond studying droplets on homogeneous and heterogeneous substrates, it is suitable to study a range of problems with mixed solid and free boundary conditions. For systems where it is not necessary to resolve a contact line region over 3 or more orders of magnitude, for example when particles are suspended in the fluid, the performance should be quite satisfactory. Possible applications range from modeling foam formation from individual gas bubbles over suspension dynamics to active swimmers. Another field where this code could be applied is the problem of electrowetting applied to heterogeneous substrates. Having a tunable additional energy source in the system that enables the droplet to cross local energy barriers makes it possible to probe the substrate energy landscape in detail.

List of symbols

Symbol	Description
$G(x,x_0)$	Green function of a free Stokes flow
$T(x,x_0)$	stress Green function of a free Stokes flow
$u(x)$	velocity of the fluid flow
$\sigma(x)$	stress tensor of the fluid flow
$f(x)$	projection of the stress tensor on the interface normal vector
$W(h)$	interface potential
η	viscosity of the fluid, non-dimensionalized to unity
γ	surface tension, non-dimensionalized to unity
θ	contact angle
k	spatial periodicity of the substrate heterogeneity
w_0	average wetting energy of the substrate
Δw	amplitude of the wetting heterogeneity
ω	frequency of the contact angle variation
μ, g	strength of the driving force
l_0	equilibrium baselength of the droplet for wetting energy W_0
x_f	position of the front contact line
x_b	position of the back contact line
$l(t)$	baselength of the droplet over time
$x_c(t)$	coordinate of the center of the droplet base over time
$\ell(t)$	length of the free interface of the droplet over time
u	velocity of the droplet
a	spring coefficient used to model the energy of the free interface
m_x	mobility of translation mode in center-of-base direction
m_l	mobility of deformation mode in baselength direction
β	ratio of center-of-base mobility and deformation mobility

List of Figures

Acknowledgements

First of all, I'd like to thank Dr. Martin Brinkmann for enabling me to take on this project, for both challenging and supporting me and for always pushing me to resolve yet another order of magnitude. This PhD has been a true learning experience.

All this would probably have not been possible in a research group other than DCF - thanks to Prof. Stephan Herminghaus who created and maintained this space of academic freedom. I'd also like to express my gratitude for very valuable discussions. I'd like to thank Prof. Marcus Müller for his input over the course of this project. Special thanks go to Prof. Uwe Thiele for very helpful and inspiring discussions and support over the years. Of course I'd also like to gratefully acknowledge the financial support from BP Upstream Operations Ltd. and many enjoyable discussions at the project meetings.

I'm forever indebted to my parents who did everything they could to make sure I have everything I need to make my way through this world. The same holds for all the rest of my family, both close and extended, no matter how far away. Special thanks go to Stefan, Laura and Sabine, you are great. Many thanks for the great times we shared go to Ghazaleh. Also from you, I learned a lot.

The list of all the former and current people in DCF who made this a very special place for me would lead to a page overflow, so it's truncated kind of arbitrarily: Johannes, for your support; Ciro, for always being good; Thomas, for always being distractable; Julie, for her contributions to the acknowledgements; Anupam, for a call from Deja; Zrinka, for preventing Diplomacy; Max, for all the coffees; Tiger, for debug support. I'd also like to thank especially Monika and Guido for providing invaluable support for all the non-scientific aspects of a PhD and Thomas for taming the daemons.

There are also some very special people outside of work to whom I owe a lot for staying in my life over the years: Impic, you know why; Marie, for being awesome; Moritz, for the plans; Max and Julia, the other Max, Sophie, Konrad and Robert, for the stories; Ariane, for being there; Heiko, for teaching me about antennas; Jan and Alex, for many entertaining evenings.

Bibliography

[1] D. G. a. L. Aarts, M. Schmidt, and H. N. W. Lekkerkerker. "Direct visual observation of thermal capillary waves." In: *Science* 304.5672 (2004), p. 847.

[2] R. Adler. "A study of locking phenomena in oscillators". In: *Proc. I.R.E. Waves Electrons* 34 (1946), p. 351.

[3] D. M. Anderson, G. B. McFadden, and A. A. Wheeler. "Diffuse-interface methods in fluid mechanics". In: *Ann. Rev. Fluid Mech.* 30 (1998), p. 139.

[4] B. Andreotti and J. Snoeijer. "Moving Contact Lines: Scales, Regimes, and Dynamical Transitions". In: *Annual Review of Fluid Mechanics* 45 (2013).

[5] G. K. Batchelor. *An Introduction to Fluid Dynamics*. Cambridge University Press, 1967.

[6] G. K. Batchelor, H. K. Moffatt, and M. G. Worster. *Perspectives in Fluid Dynamics: A Collective Introduction to Current Research*. Cambridge University Press, 2002, p. 631.

[7] P Beltrame et al. "Rayleigh and depinning instabilities of forced liquid ridges on heterogeneous substrates". In: *Phys. Rev. E* 83 (2011), p. 16305.

[8] P. Beltrame, P. Hänggi, and U. Thiele. "Depinning of three-dimensional drops from wettability defects". In: *EPL (Europhysics Letters)* 86.2 (2009), p. 24006.

[9] E. Bertrand, T. D. Blake, and J. De Coninck. "Dynamics of dewetting at the nanoscale". In: *The European Physical Journal Special Topics* 166.1 (2009), p. 173.

[10] T. Blake. "The physics of moving wetting lines". In: *Journal of Colloid and Interface Science* 299 (2006), p. 1.

[11] T. Blake and J. Haynes. "Kinetics of liquid/liquid displacement". In: *Journal of Colloid and Interface Science* 30.3 (1969), p. 421.

[12] E. Bonaccurso, M. Kappl, and H.-J. Butt. "Hydrodynamic Force Measurements: Boundary Slip of Water on Hydrophilic Surfaces and Electrokinetic Effects". In: *Physical Review Letters* 88.7 (2002), p. 076103.

[13] D. Bonn et al. "Wetting and spreading". In: *Reviews of Modern Physics* 81.2 (2009), p. 739.

[14] R. Borcia, I. Borcia, and M. Bestehorn. "Drops on an arbitrarily wetting substrate: A phase field description". In: *Physical Review E* 78.6 (2008), p. 1.

[15] K. A. Brakke. "The Surface Evolver". In: *Experimental Mathematics* 1.2 (1992), p. 141.

[16] M. Brinkmann, J. Kierfeld, and R. Lipowsky. "A general stability criterion for droplets on structured substrates". In: *Journal of Physics A: Mathematical and General* 37.48 (2004), p. 11547.

[17] A. Cassie and S. Baxter. “Wettability of porous surfaces”. In: *Transactions of the Faraday Society* 40.5 (1944), p. 546.

[18] R. G. Cox. “The dynamics of the spreading of liquids on a solid surface”. In: *Journal of Fluid Mechanics* 168 (1986), p. 169.

[19] K. Davitt, M. S. Pettersen, and E. Rolley. “Thermally Activated Wetting Dynamics in the Presence of Surface Roughness”. In: *Langmuir : the ACS journal of surfaces and colloids* 29.23 (2013), p. 6884.

[20] J. De Coninck and T. Blake. “Wetting and Molecular Dynamics Simulations of Simple Liquids”. In: *Annual Review of Materials Research* 38.1 (2008), p. 1.

[21] B.-J. deGans, P. Duineveld, and U. Schubert. “Inkjet Printing of Polymers: State of the Art and Future Developments”. In: *Advanced Materials* 16.3 (2004), p. 203.

[22] H. Ding, M. N. H. Gilani, and P. D. M. Spelt. “Sliding, pinch-off and detachment of a droplet on a wall in shear flow”. In: *Journal of Fluid Mechanics* 644.2010 (2010), p. 217.

[23] E. Doedel and B. Oldeman. *Auto 07p: Continuation and bifurcation software for ordinary differential equations*. Concordia University, Montreal, Canada, 2008.

[24] J. Eggers. “Existence of receding and advancing contact lines”. In: *Physics of Fluids* 17.8 (2005), p. 082106.

[25] J. Eggers and H. Stone. “Characteristic lengths at moving contact lines for a perfectly wetting fluid: the influence of speed on the dynamic contact angle”. In: *Journal of Fluid Mechanics* 505 (2004), p. 309.

[26] R. Fetzer and J. Ralston. “Influence of Nanoroughness on Contact Line Motion”. In: *The Journal of Physical Chemistry C* 114.29 (2010), p. 12675.

[27] M. Galassi. *GNU Scientific Library Reference Manual*. 3rd Ed.

[28] P. Gaspard. “Measurement of the instability rate of a far-from-equilibrium steady state at an infinite period bifurcation”. In: *Journal of Physical Chemistry* 94.1 (1990), p. 1.

[29] P. G. de Gennes. “Deposition of Langmuir-Blodgett layers”. In: *Colloid and Polymer Science* 264 (1986), p. 463.

[30] P. de Gennes. “Wetting: statics and dynamics”. In: *Reviews of Modern Physics* 57.3 (1985), p. 827.

[31] N. Goga et al. “Efficient Algorithms for Langevin and DPD Dynamics”. In: *Journal of Chemical Theory and Computation* 8.10 (2012), p. 3637.

[32] P. Hänggi, P. Talkner, and M. Borkovec. “Reaction-rate theory: fifty years after Kramers”. In: *Reviews of Modern Physics* 62.2 (1990), p. 251.

[33] D. Herde et al. “Driven large contact angle droplets on chemically heterogeneous substrates”. In: *EPL (Europhysics Letters)* 100.1 (2012), p. 16002.

[34] S Herminghaus. “Wetting, spreading, and adsorption on randomly rough surfaces.” In: *The European physical journal. E, Soft matter* 35.6 (2012), p. 43.

[35] L. M. Hocking. “Waves produced by a vertically oscillating plate”. In: *Journal of Fluid Mechanics* 179 (1987), p. 267.

[36] S. R. Hodges, O. E. Jensen, and J. M. Rallison. “Sliding, slipping and rolling: the sedimentation of a viscous drop down a gently inclined plane”. In: *Journal of Fluid Mechanics* 512 (2004), p. 95.

[37] H. P. Jansen et al. “Simulating anisotropic droplet shapes on chemically striped patterned surfaces.” In: *Langmuir : the ACS journal of surfaces and colloids* 28.1 (2012), p. 499.

[38] J. F. Joanny and M. O. Robbins. “Motion of a contact line on a heterogeneous surface”. In: *The Journal of Chemical Physics* 92.5 (1990), p. 3206.

[39] H. Kramers. “Brownian motion in a field of force and the diffusion model of chemical reactions”. In: *Physica* 7.4 (1940), p. 284.

[40] H. Kusumaatmaja and J. M. Yeomans. “Modeling contact angle hysteresis on chemically patterned and superhydrophobic surfaces.” In: *Langmuir : the ACS journal of surfaces and colloids* 23.11 (2007), p. 6019.

[41] L. D. Landau and E. M. Lifshitz. *Course on Theoretical Physics: Volume 6, Fluid Mechanics*. 2nd Ed. Elsevier, 1987.

[42] E. Lauga, M. P. Brenner, and H. A. Stone. “Microfluidics :” in: *Springer Handbook of Experimental Fluid Mechanics*. Springer, 2007, p. 1219.

[43] N. Le Grand, A. Daerr, and L. Limat. “Shape and motion of drops sliding down an inclined plane”. In: *Journal of Fluid Mechanics* 541 (2005), p. 293.

[44] J. Marsh, S. Garoff, and E. Dussan V. “Dynamic contact angles and hydrodynamics near a moving contact line”. In: *Physical review letters* 70.18 (1993), p. 2778.

[45] R. Melanie et al. “The Influence of Topography on Dynamic Wetting”. In: *Advances in Colloid and Interface Science* (2013).

[46] K. Migler, H Hervet, and L Leger. “Slip transition of a polymer melt under shear stress.” In: *Physical review letters* 70.3 (1993), p. 287.

[47] F. Mugele and J.-C. Baret. “Electrowetting: from basics to applications”. In: *Journal of Physics: Condensed Matter* 17.28 (2005), R705.

[48] A. Münch, B. Wagner, and T. P. Witelski. “Lubrication Models with Small to Large Slip Lengths”. In: *Journal of Engineering Mathematics* 53 (2006), p. 359.

[49] S. Narasimha et al. “High Performance 45-nm SOI Technology with Enhanced Strain, Porous Low-k BEOL, and Immersion Lithography”. In: *2006 International Electron Devices Meeting* (2006).

[50] A. Otten and S. Herminghaus. “How plants keep dry: a physicist’s point of view.” In: *Langmuir : the ACS journal of surfaces and colloids* 20.6 (2004), p. 2405.

[51] P. G. Petrov and J. G. Petrov. “A Combined Molecular-Hydrodynamic Approach to Wetting Kinetics”. In: *Langmuir* 11 (1992), p. 1762.

[52] L. Petzold. “Automatic selection of methods for solving stiff and nonstiff systems of ordinary differential equations”. In: *SIAM J.Sci.Stat.Comput.* 4 (1983), p. 136.

[53] C. M. Pooley, H. Kusumaatmaja, and J. M. Yeomans. “Contact line dynamics in binary lattice Boltzmann simulations.” In: *Physical review. E, Statistical, nonlinear, and soft matter physics* 78.5 Pt 2 (2008), p. 056709.

[54] C. Pozrikidis. *A practical guide to boundary element methods with the software library BEMLIB*. CRC Press, 2002.

[55] C. Pozrikidis. *Boundary integral and singularity methods for linearized viscous flow*. Cambridge Univ Pr, 1992.

[56] C. Pozrikidis. "Interfacial Dynamics for Stokes Flow". In: *Journal of Computational Physics* 169.2 (2001), p. 250.

[57] T. Qian, X. Wang, and P. Sheng. "A variational approach to moving contact line hydrodynamics". In: *Journal of Fluid Mechanics* 564 (2006), p. 333.

[58] J. M. Rallison. "The deformation of small viscous drops and bubbles in shear flows". In: *Annual Review of Fluid Mechanics* 16.1 (1984), p. 45.

[59] E. Raphael and P. G. de Gennes. "Dynamics of wetting with nonideal surfaces. The single defect problem". In: *The Journal of Chemical Physics* 90.12 (1989), p. 7577.

[60] M. Rauscher and S. Dietrich. "Wetting Phenomena in Nanofluidics". In: *Annu. Rev. Materials Research* 38 (2008), p. 1.

[61] M. Ripoll et al. "Low-Reynolds-number hydrodynamics of complex fluids by multi-particle-collision dynamics". In: *Europhysics Letters (EPL)* 68.1 (2004), p. 106.

[62] P. J. Rossky. "Exploring nanoscale hydrophobic hydration". In: *Faraday Discussions* 146 (2010), p. 13.

[63] M. J. Santos, S Velasco, and J. a. White. "Simulation analysis of contact angles and retention forces of liquid drops on inclined surfaces." In: *Langmuir : the ACS journal of surfaces and colloids* 28.32 (2012), p. 11819.

[64] N. Savva and S. Kalliadasis. "Two-dimensional droplet spreading over topographical substrates". In: *Physics of Fluids* 21.9 (2009), p. 092102.

[65] N. Savva, S. Kalliadasis, and G. Pavliotis. "Two-Dimensional Droplet Spreading over Random Topographical Substrates". In: *Physical Review Letters* 104 (2010), p. 84501.

[66] N. Savva, G. Pavliotis, and S. Kalliadasis. "Contact lines over random topographical substrates. Part 2. Dynamics". In: *Journal of Fluid Mechanics* 672 (2011), p. 384.

[67] A. D. Schleizer and R. T. Bonnecaze. "Displacement of a two-dimensional immiscible droplet adhering to a wall in shear and pressure-driven flows". In: *Journal of Fluid Mechanics* 383 (1999), p. 29.

[68] A. E. Seaver and J. C. Berg. "Spreading of a Droplet on a Solid Surface". In: *Journal of Applied Polymer Science* 52.3 (1993), p. 431.

[69] C. Semprebon, S. Herminghaus, and M. Brinkmann. "Advancing modes on regularly patterned substrates". In: *Soft Matter* 8.23 (2012), p. 6301.

[70] J. Servantie and M. Müller. "Temperature Dependence of the Slip Length in Polymer Melts at Attractive Surfaces". In: *Physical Review Letters* 101.2 (2008), p. 026101.

[71] D. N. Sibley et al. "On the moving contact line singularity: asymptotics of a diffuse-interface model." In: *The European physical journal. E, Soft matter* 36.3 (2013), p. 26.

[72] J. Snoeijer et al. "Thick Films of Viscous Fluid Coating a Plate Withdrawn from a Liquid Reservoir". In: *Physical Review Letters* 100.24 (2008), p. 8.

[73] J. H. Snoeijer et al. “Cornered drops and rivulets”. In: *Physics of Fluids* 19.4 (2007), p. 042104.

[74] A. Solga et al. “The dream of staying clean: Lotus and biomimetic surfaces.” In: *Bioinspiration & biomimetics* 2.4 (2007), S126.

[75] J. M. Souza. “Boundary conditions in the finite-difference method”. In: *Mecanica Computational* 1.1 (1985), p. 23.

[76] P. Spelt. “Shear flow past two-dimensional droplets pinned or moving on an adhering channel wall at moderate Reynolds numbers: a numerical study”. In: *Journal of Fluid Mechanics* 561 (2006), p. 439.

[77] G. G. Stokes. “On the theories of the internal friction of fluids in motion”. In: *Transactions of the Cambridge Philosophical Society* 8 (1845), p. 287.

[78] H. Stone and L. Leal. “Relaxation and breakup of an initially extended drop in an otherwise quiescent fluid”. In: *Journal of Fluid Mechanics* 198 (1989), p. 399.

[79] S. Strogatz. *Nonlinear Dynamics and Chaos*. Perseus Books, 1994.

[80] P. S. Swain and R. Lipowsky. “Contact Angles on Heterogeneous Surfaces: A New Look at Cassie’s and Wenzel’s Laws”. In: *Langmuir* 14.23 (1998), p. 6772.

[81] R. Takaki. “Variational principle to derive the Stokes equations”. In: *Fluid Dynamics Research* 39.7 (2007), p. 590.

[82] L. Tanner. “The spreading of silicone oil drops on horizontal surfaces”. In: *Journal of Physics D: Applied Physics* 12 (1979), p. 1473.

[83] A. Tarnowski et al. “Biodeterioration and Performance of Anti-graffiti Coatings on Sandstone and Marble”. In: *Journal of the Canadian Association of Conservation* 32 (2007), p. 3.

[84] U. Thiele and E. Knobloch. “Driven Drops on Heterogeneous Substrates: Onset of Sliding Motion”. In: *Physical Review Letters* 97.20 (2006), p. 204501.

[85] U. Thiele and E. Knobloch. “On the depinning of a driven drop on a heterogeneous substrate”. In: *New Journal of Physics* 8.12 (2006), p. 313.

[86] N. Tretyakov and M. Müller. “Correlation between surface topography and slippage: a Molecular Dynamics study”. In: *Soft Matter* 9.13 (2013), p. 3613.

[87] N. Tretyakov et al. “Parameter passing between molecular dynamics and continuum models for droplets on solid substrates: the static case.” In: *The Journal of chemical physics* 138.6 (2013), p. 064905.

[88] P. H. Valvatne and M. J. Blunt. “Predictive pore-scale modeling of two-phase flow in mixed wet media”. In: *Water Resources* 40 (2004), p. 07406.

[89] S. Varagnolo et al. “Stick-Slip Sliding of Water Drops on Chemically Heterogeneous Surfaces”. In: *Physical Review Letters* 111.6 (2013), p. 066101.

[90] O. V. Voinov. “Hydrodynamics of wetting”. In: *Fluid Dynamics* (1976), p. 714.

[91] O. V. Voinov. “Inclination Angles of the Boundary in moving Liquid Layers”. In: *Journal of the Electrochemical Society* 2 (1982), p. 216.

[92] R. Wenzel. “Resistance of solid surfaces to wetting by water”. In: *Industrial & Engineering Chemistry* 28.8 (1936), p. 988.

[93] W. Wirth and S Storp. “Mechanisms controlling leaf retention of agricultural spray solutions”. In: *Pesticide science* 33 (1991), p. 411.

[94] A. L. Yarin. “Drop Impact Dynamics : Splashing, Spreading, Receding, Bouncing...” In: *Annual Review of Fluid Mechanics* 36 (2006), p. 159.

[95] T. Young. “An Essay on the Cohesion of Fluids”. In: *Philosophical Transactions of the Royal Society in London* 95 (1805), p. 65.

[96] L. Zhai et al. “Patterned superhydrophobic surfaces: toward a synthetic mimic of the Namib Desert beetle.” In: *Nano Letters* 6.6 (2006), p. 1213.